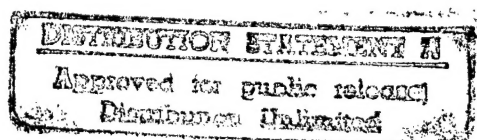National   Défense
Defence   nationale

ICEBERG DETECTION AND TRACKING
USING HIGH FREQUENCY SURFACE WAVE RADAR

by

Hing C. Chan

19970528 044
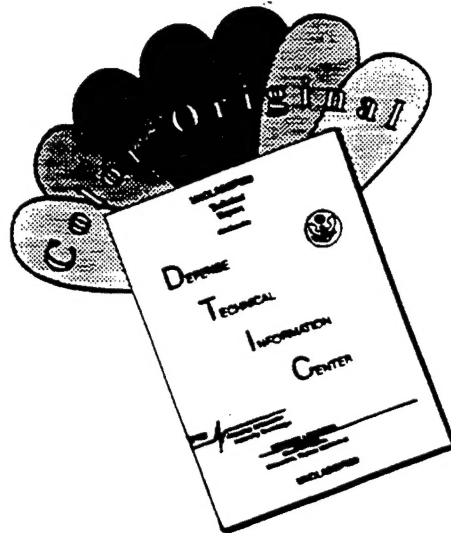
DEFENCE RESEARCH ESTABLISHMENT OTTAWA
REPORT NO. 1310

Canada

DTIC QUALITY INSPECTED 3

January 1997
Ottawa

DISCLAIMER NOTICE

ICEBERG DETECTION AND TRACKING
USING HIGH FREQUENCY SURFACE WAVE RADAR

by

Hing C. Chan
Surface Radar Section

DEFENCE RESEARCH ESTABLISHMENT OTTAWA
REPORT NO. 1310

ABSTRACT

An iceberg surveillance experiment involving multiple sensors was carried out in a one-week period between April and May, 1995. Several Canadian and U.S. agencies and members of industry participated. The Canadian Department of National Defence, in collaboration with industry, provided high-frequency surface-wave radar (HFSWR) sensors, while the Canadian and U.S. Coast Guards collected surface aerial ground-truth data. The experiment coincided with the over-flight of the surveillance area by the ERS-1 satellite. The ERS-1 data permit the evaluation of techniques for detecting icebergs from satellite imagery. The trial results demonstrated the potential of the HFSWR technology in the detection and tracking of icebergs and surface vessels. Surface targets can be detected out to beyond 100 nautical miles. The estimated positions of the targets correlate very well with the available ground-truth data.

Résumé

Une expérience portant sur la surveillance des icebergs et au cours de laquelle ont été testés de multiple détecteurs s'est déroulée pendant une semaine en avril et mai 1995. Plusieurs agences canadiennes et américaines ainsi que des membres de'industrie y ont aussi participé. Le ministère canadien de la Défense nationale, en collaboration avec l'entreprise privée, a fourni les détecteurs de radar décamétrique à ondes de surface (RDOS); les Gardes côtières canadienne et américaine ont, quant à elles, recueilli les données de terrain, par voie aérienne. L'expérience a coïncidé avec le survol de la zone de surveillance par le satellite ERS-1. Les données de ce dernier ont permis d'évaluer des techniques de détection d'icebergs grâce à l'imagerie par satellite. Les résultats de l'essai ont démontré le potentiel de la technologie du RDOS dans le champs de la détection et de la poursuite des icebergs et des navires de surface. La détection des objets de surface peut se faire à plus de 100 milles nautiques. La position estimée des objets correspond très bien avec les données de terrain disponibles.

EXECUTIVE SUMMARY

An iceberg surveillance experiment involving multiple sensors was organized by the Ice Service Branch of the Canadian Atmospheric Environment Service (AES) during a one-week period in April and May, 1995. Several agencies in both the Canadian and the U.S. Governments as well as members of industry participated. The objective was to evaluate the capabilities of spaceborne synthetic aperture and ground-based over-the-horizon radar sensors to detect and track icebergs. The Canadian Department of National Defence (DND) provided high-frequency surface wave radar (HFSWR) sensors.

DND is collaborating with industry in a technology demonstration project to demonstrate the potential of HFSWR technology to provide wide-area coastal surveillance. This trial presented an excellent opportunity to evaluate the radar's detection performance against surface targets, because of the availability of ground-truth data from other sensors. These included the Canadian Coast Guard and the Department of Fisheries and Oceans (DFO) who provided surface ground truth via observation from surface vessels. The U.S. Coast Guard's International Ice Patrol (IIP) and Atlantic Airways of St. John's, Newfoundland provided aerial ground-truth data.

The experiment was scheduled to coincide with the over-flight of the surveillance area by the ERS-1 radar satellite. The ERS-1 data permit the evaluation of techniques for detecting icebergs from satellite imagery. The ERS-1 data are to be analyzed by Science Application International Corporation (SAIC) using its filtering techniques to identify the number of targets within the vicinity of the observation platform (surface ship). The Centre for Cold Ocean Resources Engineering (C-CORE) analyzed the aerial photographs taken during the experiment to verify the accuracy of an iceberg population model.

For DND, the activities consisted of the acquisition and analysis of HFSWR data of icebergs and surface ships. Preliminary results from all the participants have been presented in a post trial evaluation meeting. In this report, we present the detailed analysis of the HFSWR data.

The results demonstrated the excellent potential of HFSWR technology for the detection and tracking of icebergs and surface vessels. Even though the nominal resolutions of the HFSWR in bearing and range were rather coarse, using advanced digital signal processing techniques, quite respectable accuracies can be obtained in both range and azimuth. Surface targets were detected out to beyond 100 nautical miles. The estimated positions of the targets correlated very well with the ground-truth data.

There are some definite advantages in employing HFSWR over other sensors in iceberg detection and tracking. First, it has the capability to provide a real-time continuous surveillance picture of a wide area of the coastal regions at relatively low cost. Second, it detects the relatively large icebergs among much smaller ones or packed sea ice. This cannot easily be done

by examining satellite images. Finally, based on relative radar-cross-section and velocity estimates, it provides some target identification capability. These capabilities are not available from coastal microwave radars.

It should be emphasized that these trial results used experimental HFSWRs, and they by no means represent the full potential of an operational HFSWR. DND, in collaboration with the Canadian Industry, is in the process of developing two full-scale HFSWRs. These radars are scheduled to become operational in June 1997. At that time a comprehensive evaluation of the capabilities of the HFSWR against various targets of military and civil interest will be carried out.

TABLE OF CONTENTS

TABLE OF CONTENTS (Continue)

LIST OF FIGURES

LIST OF FIGURES (Continue)

LIST OF TABLES

1. INTRODUCTION.

An iceberg surveillance experiment involving multiple sensors was organized by the Ice Service Branch of the Canadian Atmospheric Environment Service (AES) during a one-week period between April and May, April, 1995. Several agencies in both the Canadian and the U.S. Governments as well as members of Industry participated. This experiment was code-named BERG SEARCH '95. The objective was to evaluate the capabilities of spaceborne synthetic aperture and ground-based over-the-horizon radar sensors to detect and track icebergs. The Canadian Department of National Defence (DND) participated in BERG SEARCH '95 because it has an ongoing research and development program in high-frequency surface-wave radar (HFSWR). This R&D program is carried out in collaboration with Canadian industry (principally Raytheon Canada of Waterloo, Ontario and Northern Radar Systems Limited of St. John's, Newfoundland). The objective of this program is to demonstrate the potential of employing HFSWR technology as an economical means for providing wide-area coastal surveillance of surface and low-altitude air targets.

Unlike microwave radars, which are not capable of detecting targets that are below the horizon because of the line-of-sight limitation in the propagation of microwave signals, HF radars can detect targets below the horizon via two mechanisms. The first is by bouncing the radar signal off the ionosphere to the target and back (sky-wave over-the-horizon or OTH radars); the other is by launching the radar signal along the surface of the earth (surface-wave OTH radars) and receiving the echo via the same path. These two mechanisms do not work for microwave radars because (i) the ionosphere is practically transparent to signals at frequencies above the HF band, and (ii) surface waves attenuate rapidly with increasing frequency.

Both types of OTH radar are subject to a variety of conditions that limit their performance. In particular, the performance is influenced to a large extent by the variability of the conditions in the ionosphere. In addition, surface waves require a conducting surface to propagate. Hence HFSWR loses its OTH capability over land because of the poor conductivity of the soil. In the case of a coastal HF surface-wave radar, the ocean provides the conducting surface. Surface waves attenuate much more rapidly at horizontal polarization than at vertical polarization. The attenuation also increases with range and surface roughness. Consequently, all HFSWRs employ vertically polarized antennas; although horizontally polarized antennas may be used as auxiliary antennas for sky-wave interference suppression. Because of the large attenuation of the surface wave at the upper HF frequencies, for long-range applications HFSWR operates at relatively low frequencies (2-6 MHz).

From DND's perspective, because of the availability of ground-truth data from other sources, this trial presented an excellent opportunity to evaluate the radar's detection performance against surface targets. These included the Canadian Coast Guard and the Department of Fisheries and Oceans (DFO), who provided surface ground truth via observation from surface vessels. The U.S. Coast Guard's International Ice Patrol (IIP) and Atlantic Airways of St. John's, Newfoundland provided aerial ground-truth data. The IIP reconnaissance flights were conducted with a U.S. Coast Guard Hercules (HC-130) equipped with a Motorola X-band AN/APS-135 side-looking airborne radar (SLAR) and a Texas Instruments X-band AN/APS-137 forward-looking airborne radar (FLAR).

The experiment was scheduled to coincide with the over-flight of the surveillance area by the ERS-1 satellite, which carries a synthetic aperture radar. The ERS-1 data permit the evaluation of techniques for detecting icebergs from satellite imagery. The ERS-1 data were to be analyzed by Science Application International Corporation (SAIC) using its filtering techniques to identify the number of targets within the vicinity of the observation platform (surface ship). The Centre for Cold Ocean Resources Engineering (C-CORE) analyzed the aerial photographs taken during the experiment to verify the accuracy of an iceberg population model.

For DND, the activities consisted of the acquisition and analysis of HFSWR data of icebergs and surface ships. Preliminary results from all the participants have been presented in [1]. In this report, the detailed analysis of the HFSWR data is presented.

2.   EXPERIMENTAL HFSWR FACILITIES.

Two experimental HFSWR facilities are used by DND to conduct research. Raytheon Canada Limited (RCL) operates the facility at Cape Bonavista, and Northern Radar Systems Limted (NR) owns and operates the facility at Cape Race. The geographical locations of the two sites are shown in Figure 1. The coverage of both radars is a fan-shape area. There is a small overlap in the coverage. This could provide an opportunity to evaluate the potential performance enhancement by fusing tracks obtained from the two radars. However, this depends on whether targets of opportunity are in the overlapped area during the trial. A brief description of the two facilities and the radar parameters employed in the iceberg detection trials is presented in the following sub-sections.

2.1   The Cape Bonavista HFSWR facility.

The HFSWR facility at Cape Bonavista is shown in Figures 2. The transmit and receive facilities are, for all practical purposes, co-located, being separated by less than one km. The radar operates in a monostatic mode. The radar parameters employed by the Cape Bonavista radar in BERG SEARCH '95 are summarized in Table 1.

Table 1: Cape Bonavista HFSWR parameters for iceberg trials.

Transmit:	
Frequency	4.2 MHz.
Antenna	Log-periodic monopole array (Gain ≈ 10 dBi).
Waveform	50 μsec raised cosine pulse
Peak power:	8 kW
PRF	12.5 Hz.
Receive:	
Antenna	8 doublet monopole array.
Receiver	4 coherent receivers; multiplexed between two sets of 4 Doublets; Bandwidth = 20 kHz.
Data acquisition:	Digital demodulation (25 kHz i.f., I-Q channel sampling at 125 kHz with 16-bit A/D converter; translation to complex baseband and low-pass filtering); Data recording

The radar transmits a coherent pulse train and receives the echoes of each pulse while maintaining phase coherence over the duration of the pulse train. A simple pulsed waveform is used. The pulse length is 50 μsec with a raised cosine shaping. This yields a nominal range resolution (the extent of a range cell) of 7.5 km. The transmit antenna is a five-element log-
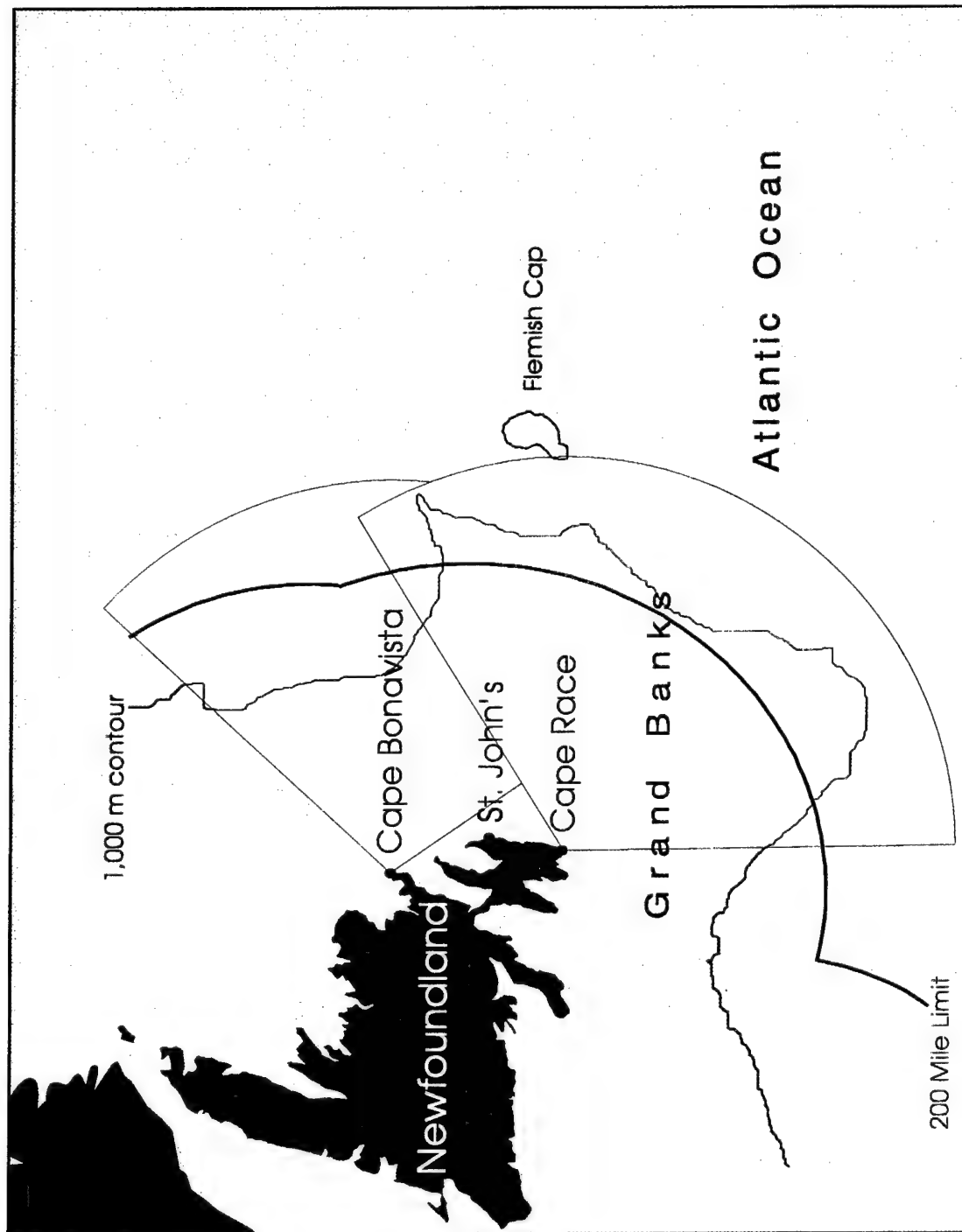
Figure 1. Geographical locations of the two HFSWR testbeds.
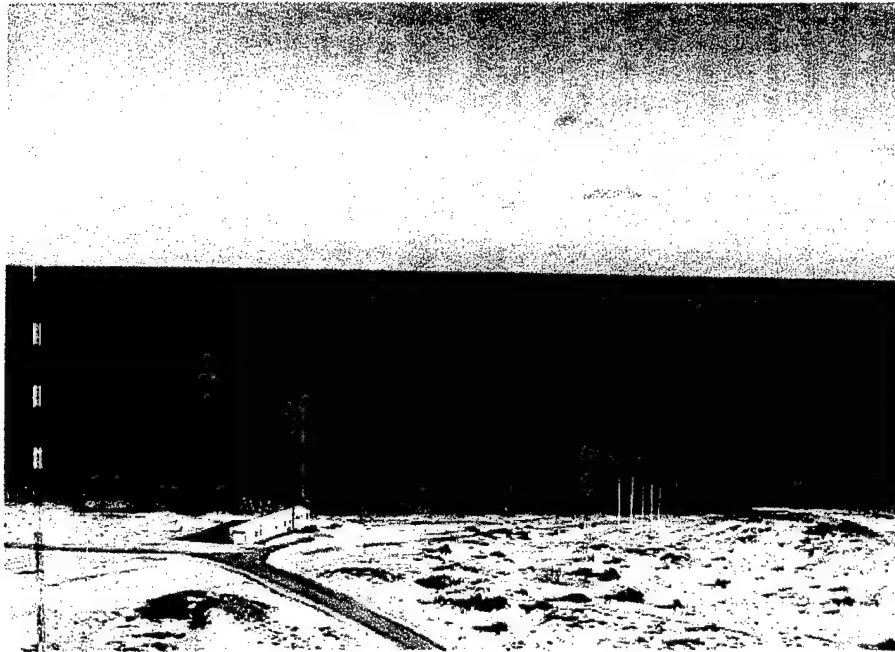
(a) Transmit facility.
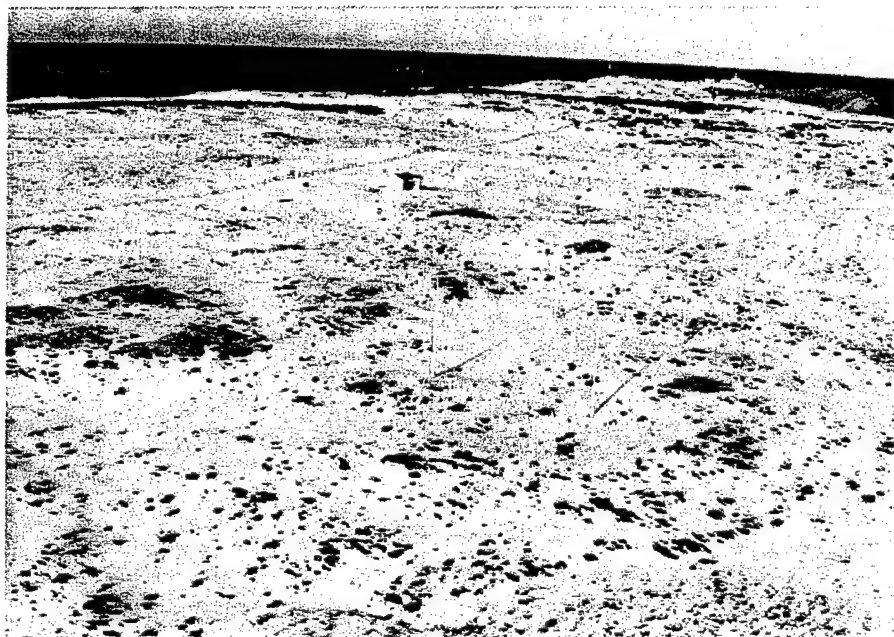
(b) Receive facility.

Figure 2. The Cape Bonavista HFSWR facility.

periodic monopole, and the nominal peak transmit power was rated at 8 kW. The transmit antenna generates a reasonably broad beam (120°) pointing towards the Atlantic Ocean.

The receive facility consists of an array of eight-doublet monopole antennas. The two antennas in each doublet are spaced 19.23 m apart and are phased so that signals coming from the rear are cancelled. The eight doublets are fed into a multiplexing unit which in turn is connected to four identical receivers.

A point target will return an echo that is a time-delayed, and possibly Doppler-shifted, replica of the transmit waveform. In the absence of any coding within the pulse, the nominal range resolution, or extent of a range cell, of the radar is given by:

$$\Delta R = \frac{c\tau}{2} \tag{1}$$

where τ is the pulse length, and c is the speed of light. For waveforms with coding such as those of frequency or phase modulation types, τ is the compressed pulse length.

In microwave radars the received waveform is normally passed through a matched filter and sampled at a rate that represents one sample (for both I- and Q-channels) per range cell. Matched filtering may be performed either at the intermediate frequency (i.f.) stage or at baseband, using analog or digital filters. In most HFSWRs, the signal from each receiver is first mixed down to an i.f. and sampled at a substantially higher rate than the signal bandwidth. The samples are then demodulated digitally and filtered using a digital low-pass filter (LPF) to remove the double-carrier component and out-of-band noise. Strictly the LPF is not a matched filter. However, because the precise shape of the waveform is not known after it leaves the antenna, we shall assume that the LPF is a good approximation of the matched filter. Since the received signal is over sampled, there is a lot of redundant information among the adjacent samples that span a range cell. For the purpose of target detection, it suffices to retain one (complex) sample per range cell after low-pass filtering. This localizes a potential target to the extent of a range cell. However, we can utilize the extra samples to determine the range of the target more precisely by locating the sample that is the local maximum.

To avoid any confusion that might arise in subsequent discussions, we shall define the term "range point" as the distance from the radar represented by a particular sampling instant of the return waveform. Time series are formed by collecting samples at the same instants in time with respect to the transmitted pulses. Thus each time series represents the returns from a range point, and a range cell may contain a number of range points as shown in Figure 3. Here, the range points, are separated by 1.2 km (8 μsec) and the extent of the range cell is 7.5 km (50 μsec). It can be seen that, even though the echo of a point target could occupy the full extent of a range cell, its true range may be deduced more precisely from the peak location. The improvement in localization of targets in range depends on the signal-to-noise ratio and whether multiple targets are present within the range cell. For this estimate to be accurate, there must not be more than one target with a particular Doppler frequency in that range cell. Assuming that the

probability of having multiple targets that have precisely the same velocity (i.e., Doppler frequency) is low, the single target scenario should apply in most cases.

ECHO WAVEFORM
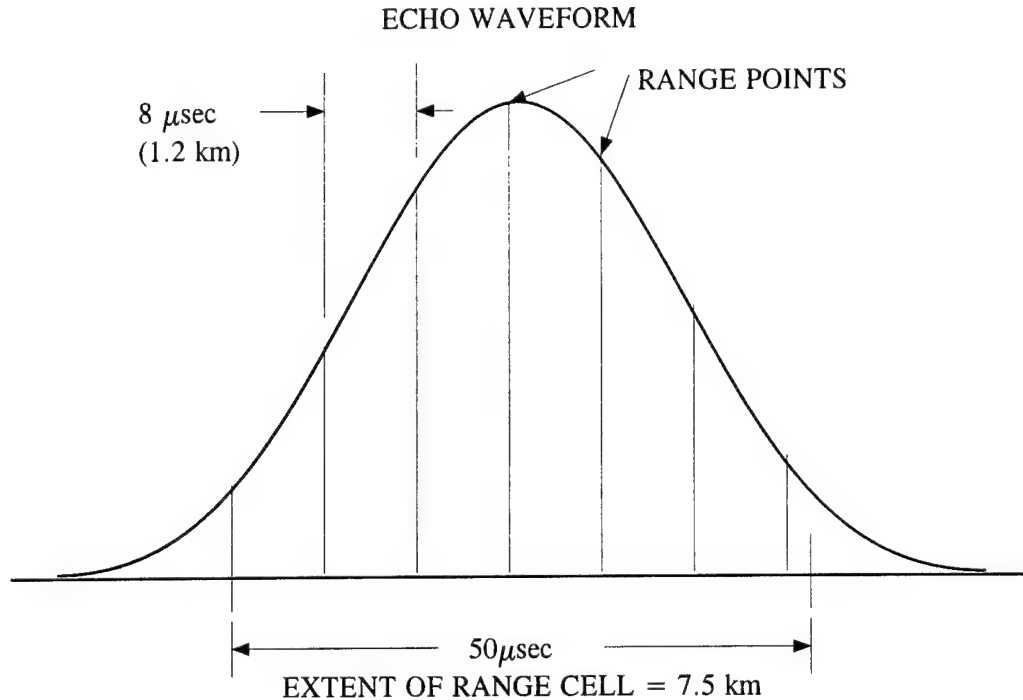
Figure 3. Illustration of range points and range cell.

2.2   The Cape Race HFSWR facility.

The HFSWR facility at Cape Race is shown in Figures 4. The transmit and receive facilities are also co-located, and the radar operates in a monostatic mode. Table 2 summarizes the radar parameters employed by the Cape Race radar for BERG SEARCH '95.

A frequency-modulated, interrupted-continuous-wave (FMICW) waveform is used in the Cape Race radar. The FMICW is a wide-band pulse compression waveform. The transmitter emits a sequence of coherent pulses whose carrier frequency varies linearly with time. The instantaneous bandwidth is not very large, in the order of several kHz. However, the carrier frequency is swept over a wide bandwidth (over 100 kHz). Pulse compression takes place over a number of pulses. The duration of the sequence of transmitted pulses is called the sweep period, and the frequency range in which the carrier varies over one sweep period is called the FM sweep bandwidth. Between pulses, the transmitter is turned off, and the echoes are received by the receivers.
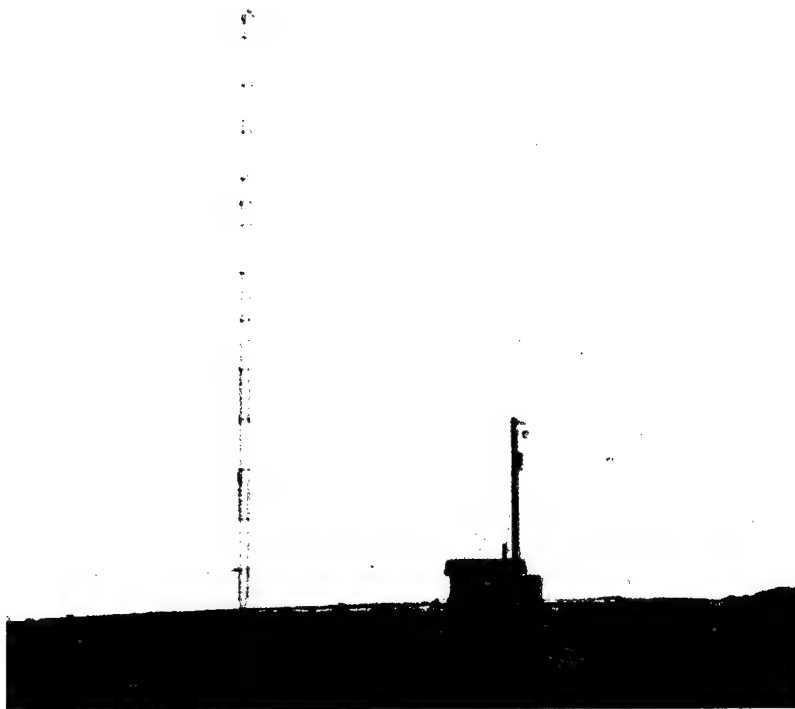
(a) Transmitting Antenna.

(b) Receive Antenna Array.

Figure 4. Cape Race HFSWR facility.

Table 2: Cape Race HFSWR parameters for iceberg trials.

Transmit	
Frequency:	5.811 MHz.
Antenna:	Log-periodic dipole array (Gain ≈ 10 dBi).
Waveform:	Frequency modulated, interrupted continuous wave (FMICW), BW = 125 kHz; transmit pulse length = 240 μsec.
Peak power:	8 kW
WRF:	9.01 Hz
Receive	
Antenna:	40-element array.
Receiver	effective bandwidth = 125 kHz.
Signal Processing:	Demodulation; Digital pulse compression; and Data recording

The receive facility of the Cape Race HFSWR consists of an array of forty folded monopole antennas. There are, however, only ten receivers. The outputs of four adjacent antennas are first combined and fed into one of the ten receivers. This arrangement resulted in some complication in the analysis of the trial data, as will be discussed in Section 2.3d.

The received signal is mixed with the transmitted signal and translated down to an i.f. of 25 kHz and then low-pass filtered and sampled. Since the echo signals are basically delayed version of the mixer signal (in this case, linear FM), the mixer output is a superposition of many sinusoidal waveforms whose frequency is a function of the range of the sactterer that produces the echo. After the entire sequence of pulses is transmitted and the echoes received, digital pulse compression is performed on the received signal, which yields one sample of the time series for each range point. For the Cape Race radar, the separation of the range points is equal to the compressed pulse length. The above sequence of operations is repeated in subsequent FM sweep periods, and time series for all compressed range cells are collected.

To avoid any confusion that might arise from discussions of the PRF with respect to the FMICW waveform, the time interval between two successive FM sweeps is called the waveform repetition interval (WRI), and the reciprocal of WRI is called the waveform repetition frequency (WRF). The detailed operation and processing of the FMICW may be found in [2]. The FMICW employed in the trial has an effective bandwidth of 125 kHz which yields a nominal range

resolution of 1.2 km. Hence, for the Cape Race radar, two distinct targets can be resolved if they are separated in range by more than 1.2 km.

2.3   Limitations of the experimental facilities.

Because the two HFSWR facilities were experimental, there were limitations that degraded the trial results. In evaluating the present set of trial results, these limitations must be kept in mind.

(a)   Low average power

The average power of a radar is equal to the product between the peak power and the duty cycle. The duty cycle is the fraction of a time interval when the radar transmitter is turned on.

For the Cape Bonavista radar, the peak power was 8 kW, the pulse length was 50 µsec and the PRF was 12.5 Hz. Hence the average power was

$$P_{AV} = 8000 \times 50 \times 10^{-6} \times 12.5 = 5 \text{ Watts}$$

For the Cape Race radar, Northern Radar Systems estimated that the peak power was about 8 kW and the duty cycle was about 7%. Hence the average power was:

$$P_{AV} = 8000 \times 0.07 = 560 \text{ W}.$$

(b)   Relatively coarse azimuthal and range resolutions.

The azimuthal resolution of an antenna array is proportional to the aperture size. For a linear array whose elements are spaced half a wavelength apart, the 3 dB beamwidth may be approximated by the following formula [3]

$$\Theta_B = \frac{101.6}{N} \tag{2}$$

where Θ_B is the beamwidth in degrees and N is the number of antenna elements in the array.

For the Cape Bonavista radar, the beamwidth was approximately 101.6/8 = 12.7°, and for the Cape Race Radar, 101.6/40 = 2.54°. For the case of a single target, improved accuracy in the bearing estimate can be obtained by interpolating the signals from various directions. This will be described in more detail in Section 3.2.3b.

The range resolution of a radar is a function of the signal bandwidth, which nominally was equal to the reciprocal of the pulse length. For the Cape Bonavista radar, the signal

bandwidth is 20 kHz (i.e., the reciprocal of 50 µsec). This translates into a range resolution of about 7.5 km. Because the velocity of icebergs is confined to a very narrow range, Doppler is less effective as a discriminant for detecting icebergs than for ships and aircraft. It is difficult to resolve two iceberg targets with the same bearing, if they are separated in range by less than the radar's nominal range resolution.

Nevertheless, considerable improvement in the accuracy of the target position can be obtained by considering the information in bearing, range and Doppler collectively, rather than individually. That is, two targets that are unresolvable in two out of the three dimensions may be resolvable if they are separable in the third dimension.

(c)   Ambiguous range response in the Cape Race data.

In analyzing the Cape Race data, it was found that there exists a certain anomalous response that is periodic in range. This anomalous behaviour was observed in a few Doppler bins around zero only. Figure 5 shows the range profile of the response for the zero Doppler component. It can be seen that large spikes appear periodically in range, with a period of 32 range cells (or about 38.4 km). The exact origin of this anomalous response has yet not been determined. However, in consultation with the NR engineers, it is conjectured that it is related to the ambiguous range response associated with the particular implementation of the pulse compression processing of the FMICW waveform.
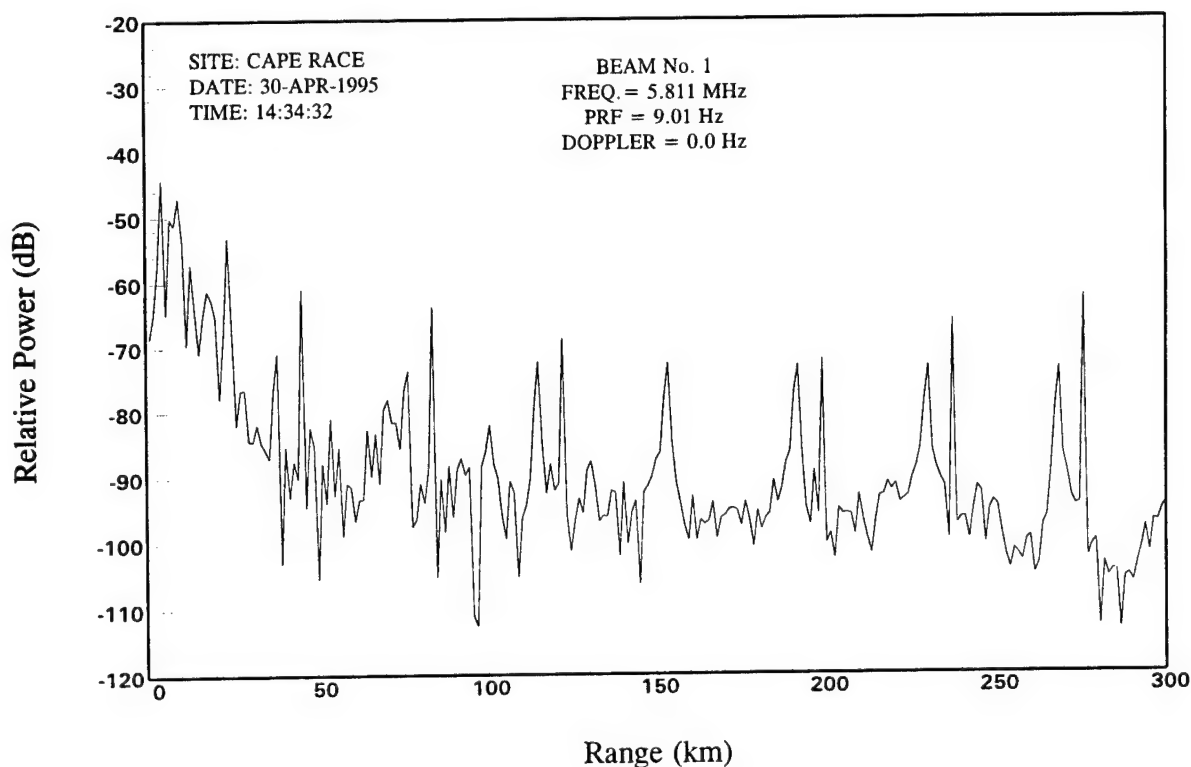
Figure 5. Ambiguous range response observed in the Cape Race HFSWR.

The elimination of the ambiguous range response is essentially an engineering problem that can be overcome. Nevertheless, the presence of this ambiguous range response near the zero Doppler bin presents some complications in the detection of icebergs, because the Doppler shift of most icebergs is also around zero. The conventional automatic detection and constant false alarm algorithms could not be applied in a straight-forward manner.

One could gate out those range cells at which the ambiguous response is known to exist. However, this means that targets that are near these periodic ranges will be lost because the ambiguous range response spans several range cells, albeit at lower magnitudes.

All the detections had to be checked manually and examined in the Doppler, azimuthal and range dimensions to ensure that they were legitimate targets. This was a rather laborious process; however, it was necessary to ensure that the detections were valid before they were compared with the ground-truth data.

(d)   Ambiguous azimuthal response in the Cape Race HFSWR.

The Cape Race radar had a further complication in regard to the bearing estimate. This was a result of the sub-array configuration used in that radar. The Cape Race radar had only ten receiver channels. With forty antenna elements, groups of four adjacent antennas were first combined, in a sub-array configuration, to form a composite element. These composite elements could be electronically phased to point in a specific direction. The resulting ten composite elements were then fed to the ten receiver channels. The effective separation of the composite elements was about 2λ. This produced an antenna pattern that was periodic in angle (grating lobes).

With ten receiver channels, array patterns can be synthesized from the signals such that the main lobe points to any direction in a sector centred about the pointing direction of the composite element. The grating lobes of the synthesized array pattern, except those of the one with the same pointing direction as that of the composite elements, will not coincide with the nulls of the elemental pattern. Figure 6a shows the array pattern together with the elemental pattern of a 10-element linear array for the case where both the array and all the composite elements are pointing at $0°$. Two grating lobes are formed on both sides of the main lobe. The total pattern of this array is the product (or the sum in dB scale) of the array pattern and the elemental pattern, assuming all the elements are identical. In this case the grating lobes do not present serious problems because the elemental pattern has nulls that coincide with the array's grating lobes.

Figure 6b shows the array pattern for a look direction of $16°$ off boresight together with the elemental pattern that is pointing at boresight. It can be seen that the nulls of the elemental pattern no longer coincide with the grating lobes of the array pattern. In fact, both the main lobe and one of the grating lobe intersect the elemental main lobe at about the same gain. The resulting high gain in the grating lobes produces an ambiguity in the bearing estimate because the radar cannot distinguish a target in the direction of the main lobe from those in the direction of the grating lobes. This ambiguity will be eliminated in a fully developed HFSWR; however, its presence in the experimental trial data complicated the analysis of the Cape Race data.

12
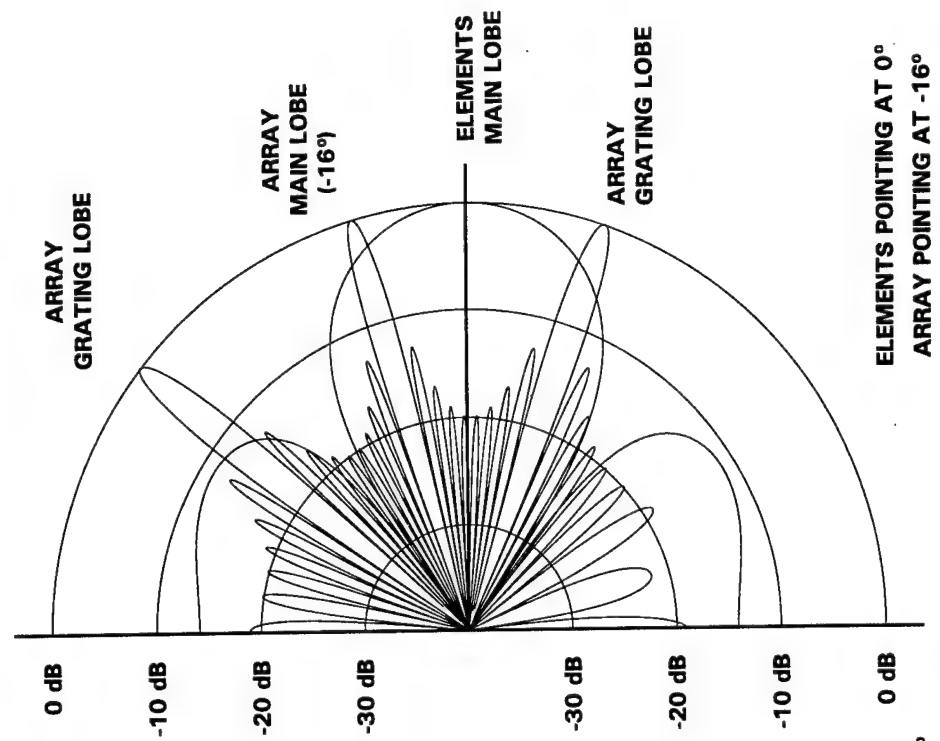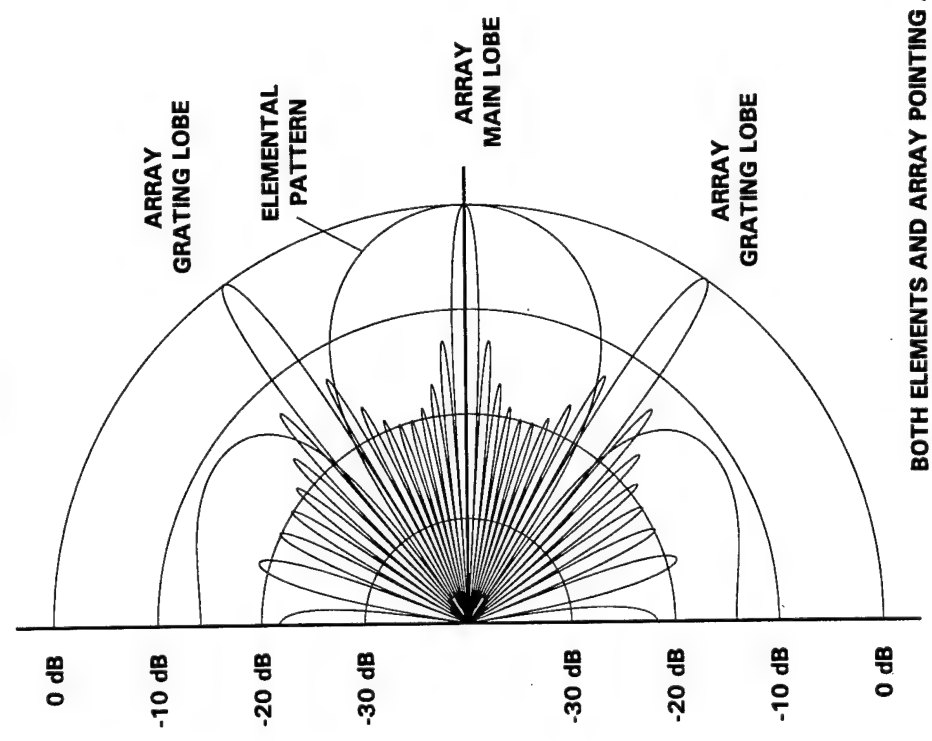
Figure 6. Azimuthal ambiguity in the Cape Race HFSWR.

13

3. THE HFSWR SIGNAL ENVIRONMENT, SIGNAL PROCESSING AND TARGET DETECTION.

For optimum target detection performance, the radar signal must be processed to enhance the signal-to-noise ratio (SNR). This is done by first sorting the radar returns in azimuth, range and Doppler and then comparing the result with a threshold setting that satisfies certain probability of detection (P_d) and probability of false alarm (P_{fa}) criteria. Before going into signal processing, detection and tracking, it would be informative to examine the signal environment of a typical HFSWR.

3.1 The HFSWR signal environment.

Regardless of which waveform is used, the recorded data represent the returns from all the range points up to the maximum unambiguous range. The maximum unambiguous range is determined by the radar's waveform repetition interval (PRI)

$$R_{max} = \frac{cT_f}{2} \tag{3}$$

where T_f is the PRI of the radar.

The resolution of an HF radar is generally rather coarse in both the azimuthal and range dimensions because of the limited aperture size of the antenna array and limited signal bandwidth. However, the resolution is relatively fine in the Doppler (or velocity) dimension. This, ironically, is a consequence of the low resolutions in azimuth and range. Because the range cell is large (7.5 km for the Cape Bonavista radar), it takes even a high speed target a considerable amount of time to migrate from one range cell to the next. For example it takes a Mach 1 target 22.7 seconds to traverse a distance of 7.5 km. This means that one can perform coherent integration over 22 seconds without any significant loss of signal. For this reason, Doppler is used as the principal target discriminant.

Doppler processing is a form of coherent integration, and it sorts the signal components according to their Doppler frequency. The time series for each channel is first Doppler processed using the fast Fourier transform (FFT), with a Blackman window [4] to suppress the Doppler sidelobes. The squared magnitudes of the FFT represent the Doppler spectrum of the return echoes.

The individual spectral components of all the channels are used to form beams that enhance the signal from a desired direction (simultaneous digital beamforming). Targets are discriminated against background noise and interference based on a higher magnitude of a Doppler component, for a given range and azimuth, than a threshold that is designed to maintain a given false alarm rate.

The undesirable background signal components against which a target must compete for detection include galactic, atmospheric and man-made noises, co-channel radio interference, direct over-head reflection of the radar pulse and sea clutter. An active research program is being conducted at DREO in collaboration with RCL and NR. As this research is on-going, the two HFSWR facilities that were used in this study should be considered rudimentary and experimental.

Sea clutter is self-generated interference that results from the reflection of the radar signal off ocean waves. Ocean waves result from the interaction of the wind and gravitational force on the water surface, and are present to varying degrees in all wavelengths. When the ocean wavelength is exactly half that of the radar wavelength, the echoes from the wave facets on two adjacent crests reinforce and produce the Bragg resonance [5] components, or the Bragg lines. Bragg resonance is a first order scattering mechanism which means that the signal undergoes only one scattering before returning to the radar.

Second and higher order peaks in the spectrum result from constructive interference of the radar signal after scattering more than once off the wave facets. Higher order scattering of the radar signal by ocean waves of different wave lengths produces the sea-clutter continuum.

Figure 7 shows a typical Doppler spectrum of the radar returns as observed by a HFSWR. The central portion of the spectrum comprises the background signal components against which surface targets are detected. A target travelling at a constant velocity will produce a spectral line in the spectrum with a Doppler frequency given by [6]
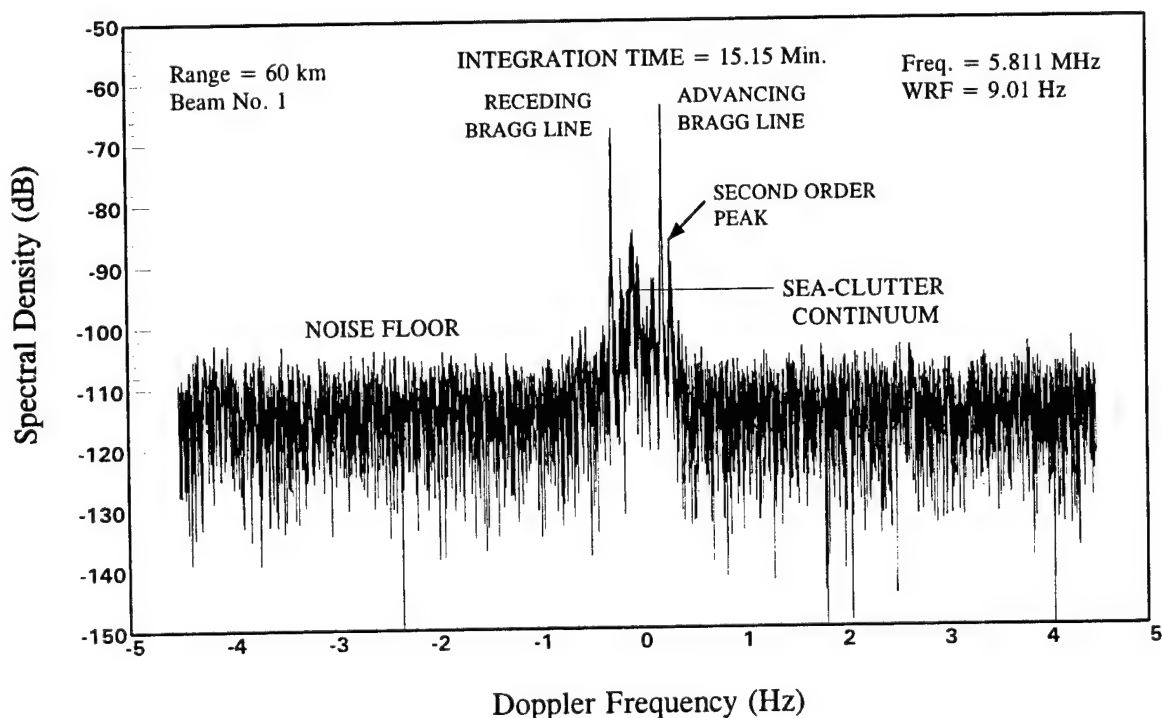
Figure 7. A typical HFSWR Spectrum.

$$f_D = -\frac{2v}{\lambda} \qquad (4)$$

where v is the velocity of the target in m/sec and λ is the radar wavelength in metres; v is positive (i.e., $f_D < 0$) when the target is travelling away from the radar.

The two large spectral peaks in Figure 7 are the Bragg lines. The frequencies of the Bragg lines are given by:

$$f_B = \pm [\frac{g}{\pi \lambda}]^{\frac{1}{2}} \qquad (5)$$

where g = 9.81 m/sec^2 is the gravitational acceleration.

The spectral peak on the left hand side of Figure 7 is called the receding Bragg line, whose frequency is obtained by taking the negative sign in (5). The one on the right hand side is called the advancing Bragg line, and its frequency is obtained by taking the positive sign in (5). The Bragg lines appear as two very large targets.

Substituting (5) into (4) and solving for v, the apparent velocities of the two Bragg lines are given by

$$v_B = \pm [\frac{g\lambda}{4\pi}]^{\frac{1}{2}}. \qquad (6)$$

The spectral components around zero-Doppler are the sea-clutter continuum. The nominal velocity of icebergs is in the range of 0 to 1 knot. Hence an iceberg will appear in the velocity spectrum close to zero. Surface ships, in general, would have a much higher velocity than icebergs, in the order of 10 to 20 knots. Consequently a ship target would normally appear in the velocity spectrum away from the zero value, except, of course, when the vessel is stationary or travelling in a direction tangential to the radar beam. In any case, they will appear to the radar in the sea-clutter dominated region.

The relatively flat portion of the spectrum represents that of the external noise which is the normal level of the radar response to the background noise. This portion of the Doppler spectrum is where high speed aircraft targets normally appear.

Figure 8 provides a graphical representation of the HFSWR signal environment. This figure is obtained by displaying the Doppler spectra of the radar returns from all range points, in a fixed azimuth, in 3-D format. The data for this figure were obtained in an earlier trial with the Cape Race radar using a coherent integration period of 27.89 seconds. The x-axis represents the Doppler or velocity dimension, and the y-axis represents the range dimension. There are 250 spectra that span a range of about 300 km (1.2 km per spectrum). The Doppler domain is ± 4.6 Hz which, at the radar frequency of 5.811 MHz, corresponds to a velocity domain of ± 230 knots. The z-axis is the magnitude of the Doppler component in dB (relative to unity). For display purpose, the magnitudes are hard limited to -110 dB which is slightly above the average noise floor observed in the data.

The sea-clutter components are concentrated around zero Doppler. The Bragg lines have been suppressed in the figure by replacing the values of a few Doppler bins around f_B (see (5)) by the average values of a small number (two on each side of the Bragg lines) of neighbouring bins. This was done so as not to obscure other spectral details of interest. Targets and interference can also be seen. One of the targets was an Air Force Challenger 601-3A flying at an altitude of 200 ft and a velocity of -220 knots (moving away from the radar). It is observed to be at about 115 km. One form of interference is seen here (Dopplers corresponding to velocities around 200 knots) that is independent of range. Detection of targets with Doppler frequencies that coincide with those of the interference would be degraded.

The HFSWR spectrum also contains a wealth of information regarding the ocean environment such as the wave height, wind speed and direction, velocity of the ocean current, and so forth. All of these can be important in search and rescue.

3.2   Signal processing.

The signal processing performed on the data was conventional in that Doppler processing and digital beamforming are carried out using the fast Fourier transform (FFT) technique. Super-resolution techniques such as the auto-regressive [7] and MUSIC [8] spectral analysis algorithms were not used.

The data were supplied as large files recorded on 8 m.m. EXABYTE tape cassettes. The signal processing procedure employed in the analysis of both the Cape Bonavista and Cape Race data was similar. They included

(i)   Data decimation via coherent summation,
(ii)   Doppler processing, and
(iii)   Digital beam forming.

3.2.1   Data decimation.

Each data file from the Cape Bonavista experiment contains the returns of approximately 30,000 pulses. At a PRF of 25 Hz, these represent an observation time of about 20 minutes. But because the receivers were multiplexed, with the input selected from one of two antennas, the effective PRF was 12.5 Hz. Hence the time series for each channel contains about 15,000 complex

FILE = AIR_SEVEN

DATE: 28-OCT-1994
TIME: 18:23:28

FREQ. = 5.81 MHz
WAVEFORM = FMICW
BW = 125.0 kHz
WRF = 9.18
INTEGRATION TIME = 27.89 sec.
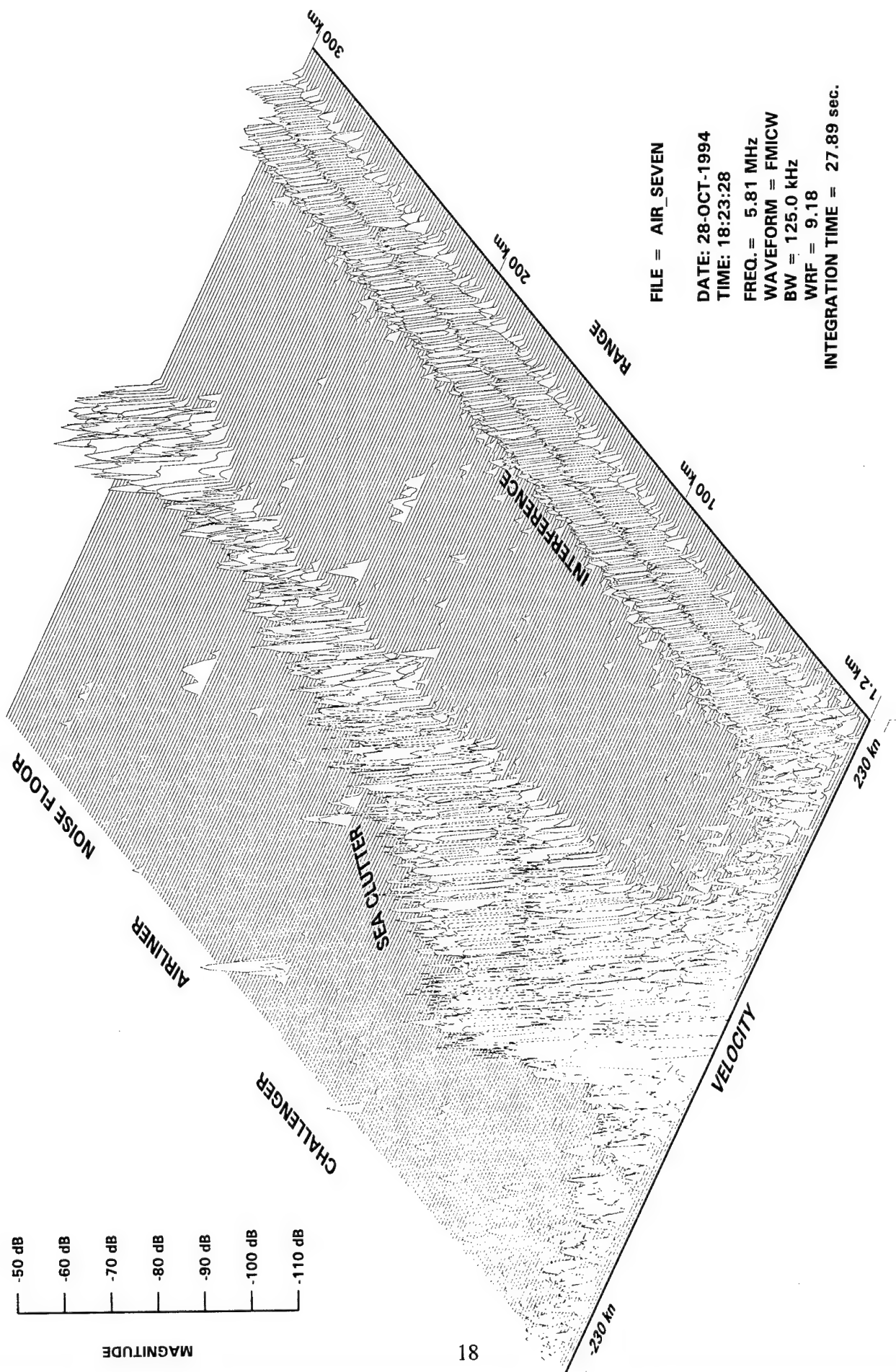
Figure 8.   3-D view of the HFSWR signal environment.

18

samples.

To reduce the time and data-storage requirements, it was decided not to attempt the detection of aircraft targets. This was justified because of the low average power of the Bonavista HFSWR. In previous aircraft detection trials, the radar was re-configured (employing higher PRF and a fixed receive beam) to yield a substantially higher average power.

For the iceberg tracking trial, all receiver channels had to be sampled, and the limited data storage capacity dictated the use of a low PRF to achieve a long observation time. As a result, the average power was very low, about 5 W. At this level of average power, it is unlikely that small aircraft beyond the horizon could be detected.

For a PRF of 12.5 Hz, the unambiguous Doppler domain is ± 6.25 Hz which, at the radar frequency of 4.1 MHz, correspond to an unambiguous velocity domain of ± 228.7 m/sec, or ±444.6 knots. Since the primary targets of interest were icebergs and surface vessels, a maximum unambiguous velocity domain of ± 30 knots would suffice. This translates to an unambiguous Doppler domain of ± 0.42 Hz. Decimation can be used to reduce the amount of data before Doppler processing. This can be done with coherent summation. Coherent summation is effectively a LPF that has a pass band of $1/T_i$, where T_i is the integration time. The time series were coherently summed over fourteen contiguous samples. This effectively reduced the Doppler bandwidth from ± 12.5 Hz to about ± 0.9 Hz, which is adequate for iceberg and ship detection. The length of the original time series was reduced from 15,000 samples to slightly over 1024.

Similar decimation was performed on the Cape Race data. The Cape Race data files contain the returns of approximately 25,000 FM sweeps. The WRF of the Cape Race data was 9.01 Hz which, at the radar frequency of 5.811 MHz, corresponds to a maximum unambiguous velocity domain of ± 226.08 knots. If aircraft detection was not performed, then an unambiguous velocity domain of ± 30 knots would suffice. For the Cape Race data, the data were coherently summed over eight consecutive samples. This reduced the effective Doppler domain to ± 0.56 Hz, and the length of the time series was reduced to 3125 samples.

3.2.2 Doppler processing

After coherent summation, the decimated time series were processed by an FFT, using a Blackman window to suppress the Doppler sidelobe. Windowing is necessary for ship and iceberg detection because of the very large magnitudes of the Bragg components whose Doppler sidelobes can easily overwhelm legitimate targets. The Blackman window is defined as

$$W_n = 0.42 + 0.5\cos(\frac{2\pi n}{N}) + 0.08\cos(\frac{4\pi n}{N}) \tag{7}$$

for n = 0,1,2,...,N-1.

For the Cape Bonavista data, the decimated time series have 1071 samples. We retained 1024 of these samples and divided them into two segments of 512 samples each and processed them with a 512-point FFT. The effective coherent integration time for both the data decimation and FFT was equivalent to 9.56 minutes. The resulting spectrum has a nominal velocity resolution of 0.124 knots. However, since the Blackman window was used, the Doppler main lobe actually occupied more than one Doppler bin.

For the Cape Race data, the decimated time series have 3125 samples. We used a 1024-point FFT. The effective integration time for both data decimation and FFT was 15.15 minutes. Each data file yielded three detection intervals. The resulting spectra had a nominal velocity resolution of 0.055 knots.

After Doppler processing, the complex FFT results for each range point were stored on disk files. These files were used in subsequently coarse and fine beam-forming operations.

3.2.3 Digital beam forming.

To enhance the signal-to-noise ratio (SNR) of potential targets before detection, digital beam forming was performed. Figure 9 shows a linear array with N antenna elements. A plane wave is impinging on the array at an angle of θ° with respect to boresight. Since the plane wave is coming at an angle other than boresight, it takes time for the wavefront to arrive at the various elements of the array, and there is a phase difference between the signal at element n compared with that at the reference element (element zero). This phase difference is given by

$$\phi_n = \frac{2\pi nd}{\lambda}\sin\theta \tag{8}$$

n = 0,1,2,.., N-1,

where c is the speed of light; λ is the radar wavelength and d is the element spacing.

To steer the beam toward the direction of θ, one needs to compensate for the phase differences at each element so that signal components in that direction at each element add up in phase. This is accomplished by multiplying the signal at element n by the phasor

$$\exp[-j(\frac{2\pi nd}{\lambda}\sin\theta)]. \tag{9}$$

Hence the signal coming from bearing θ is obtained by

20
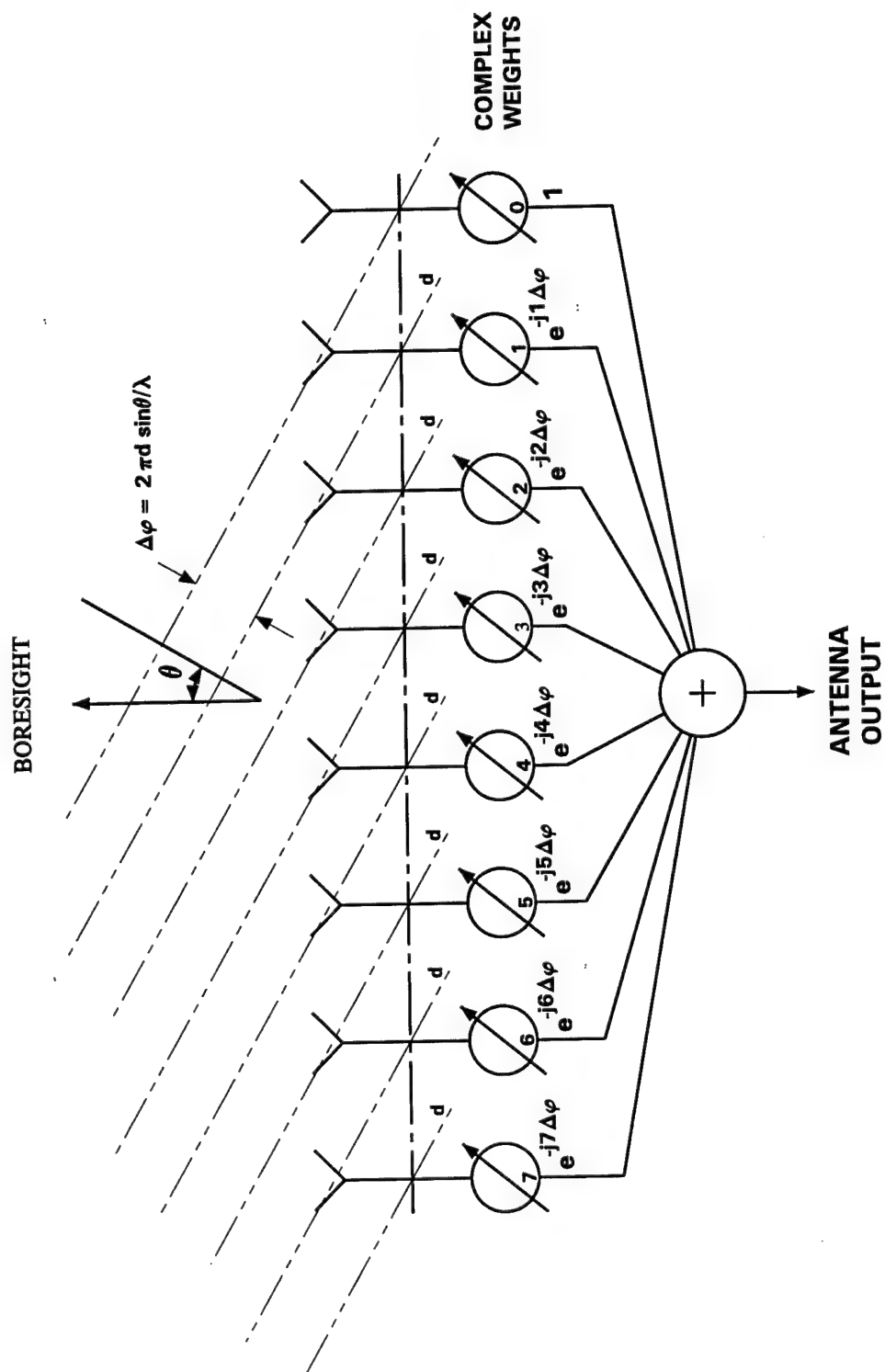
Figure 9. Digital beamforming in a linear array.

21

$$S(\theta) = \sum_{0}^{N-1} x_n \exp[-j(\frac{2\pi nd}{\lambda}\sin\theta)]. \tag{10}$$

The expression in (9) is identical to the DFT

$$F_k = \sum_{0}^{N-1} x_n \exp[-j(\frac{2\pi nk}{N})] \tag{11}$$

if one lets k = Nd sinθ/λ.

(a) Coarse beamforming

Signals from N discrete directions may be obtained from the DFT of the samples of the antenna array. For an array with N elements, N independent beams may be formed simultaneously, with the pointing direction with respect to boresight determined from the DFT index k by

$$\theta = \sin^{-1}(\frac{k\lambda}{Nd}) \tag{12}$$

for k = 0,1,2,...., N/2-1.

where k is the DFT index.

Equation (12) is for positive azimuthal angles. For negative azimuthal angles, the pointing direction is given by

$$\theta = \sin^{-1}[\frac{(k-N)\lambda}{Nd}] \tag{13}$$

for k = N/2,...., N-1.

Equation (11) represents a uniformly weighted array pattern, which has a half power beam width approximately given by (2). A target located at an azimuth mid-way between two beams would suffer a loss in SNR of about 3 dB. To minimize this loss and to suppress the azimuthal sidelobes, a weighting function such as the Taylor weighting [9] is applied to the array data

$$F_k = \sum_0^{N-1} W_n x_n \exp[-j(\frac{2\pi nk}{N})]$$ (14)

where W_n is the weighting to be applied to the nth element.

Because the beams are formed digitally, antenna aperture weighting is analogous to data windowing used in spectral analysis. In fact many of the data windows such as Hanning, Hamming or Blackman can be used. In subsequent processing of the iceberg trial data, the Blackman weighting is used. Figure 10 compares the array patterns of the eight-element array computed by using a 256-point FFT padded with zeros. The curve without symbols is the uniformly weighted (or unweighted) array, and the curve with circular symbols is the Blackman-weighted array. The 3 dB main beamwidths are 12° and 23°, and the first side lobes are -13.6 dB and -58 dB, for the uniformly and Blackman weighted arrays, respectively.
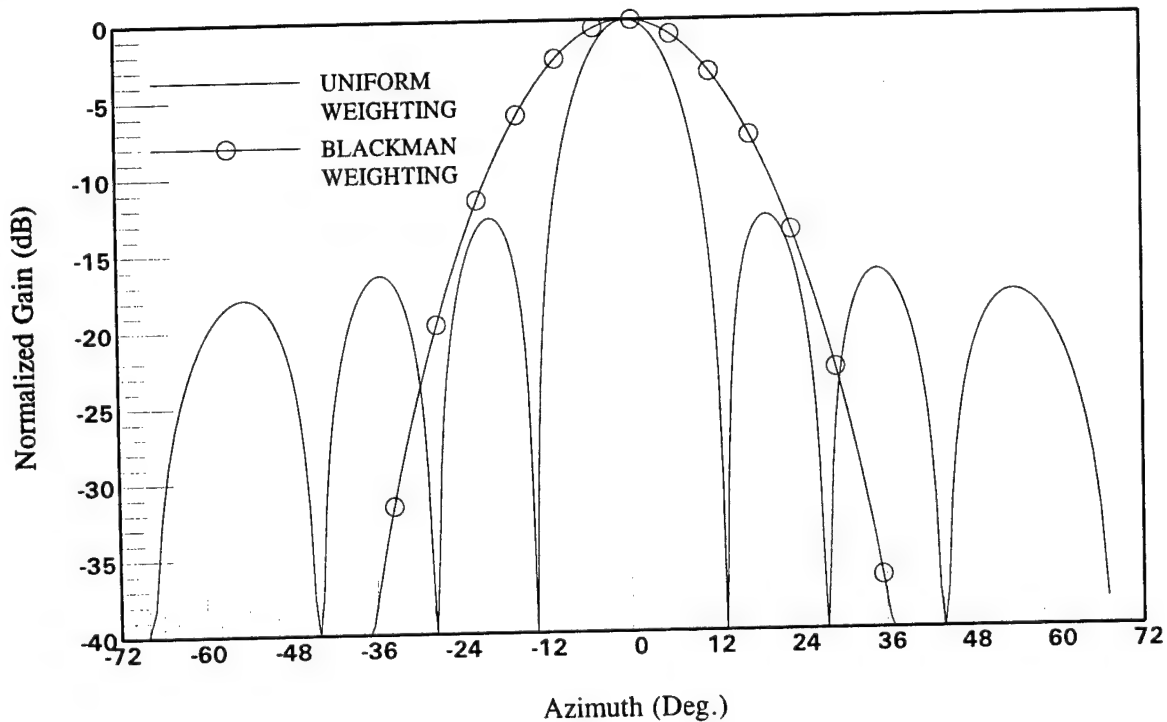
Figure 10. Array patterns of an 8-element array with uniform and Blackman weightings.

Digital beamforming was performed on each Doppler component in the spectrum. Figure 11 shows the resulting spectrum of a Cape Bonavista experiment for a range of 116.4 km (62.8 n.mi) from the radar at a nominal bearing of 0° (Beam No.1). A target is indicated on the basis that a spectral peak is observed at a Doppler of 0 Hz. This indicates a stationary target at that range with a nominal bearing at boresight.

23

(b) Fine beamforming.

The coarse beam forming is intended to maximize the SNR in the general direction of a potential target. It only localizes the target azimuth to one of N discrete bearings. For a more accurate estimate of the target bearing, fine beamforming is required. This was done as follows. Using the example in Figure 11, the 0 Hz spectral components (both real and imaginary parts)
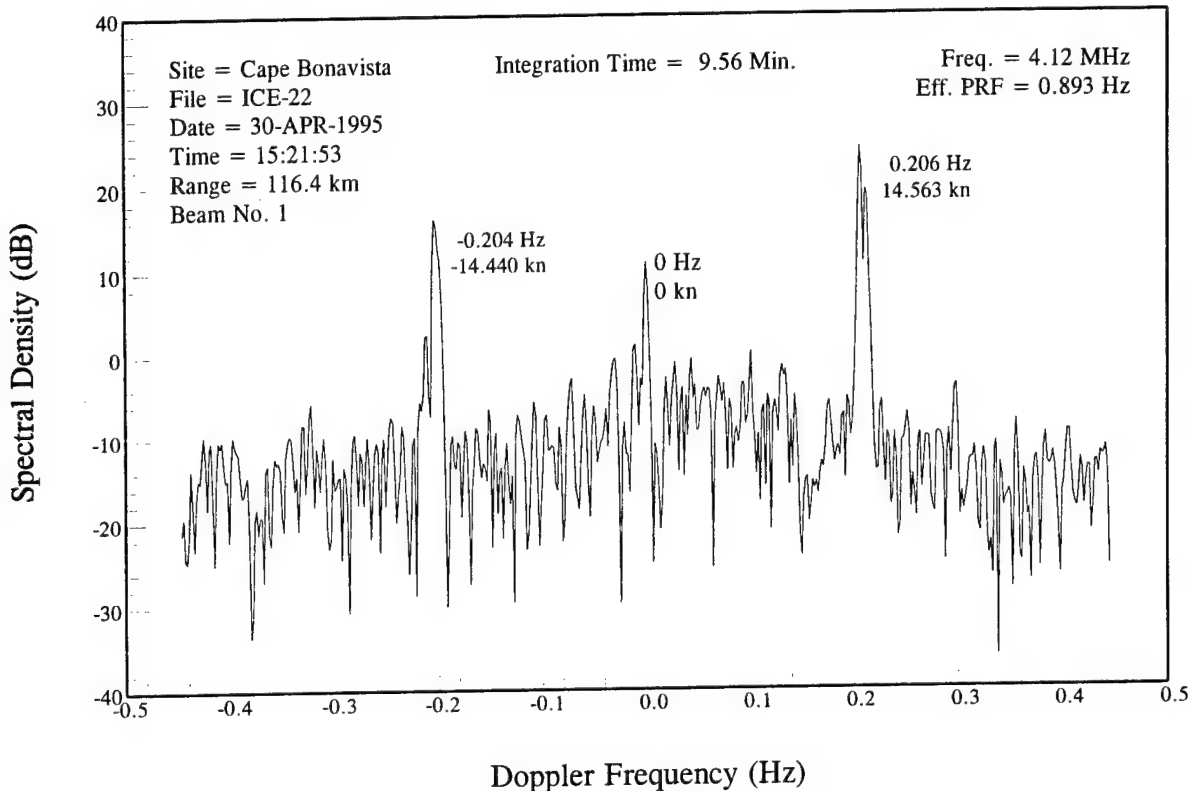
Figure 11. A stationary target observed in a HFSWR spectrum.

from each of the eight channels were placed in a large data array (we used 256 points) and augmented with zeroes. A Blackman window was used to multiply the non-zero samples. In this case, there are only eight non-zero complex samples. An FFT was performed on this augmented data array which yielded the azimuthal response of the selected Doppler component (in this case 0 Hz). The result is shown in Figure 12. By substituting the DFT index k at which the response is maximum into (13), the bearing of this target is estimated to be -2.13° from boresight. Note that in the fine beamforming case, the value of N is the augmented data length (in this case 256) instead of the number of antenna elements as in coarse beamforming.
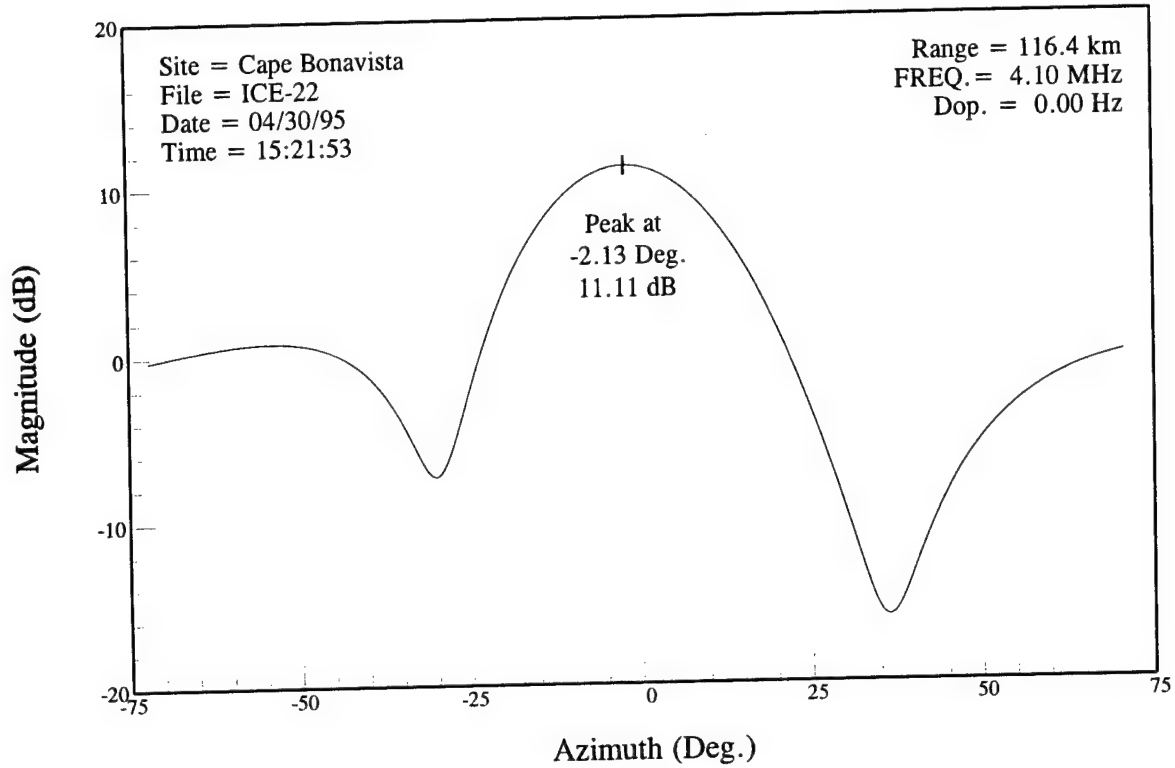
Figure 12.   Example of fine beamforming.

3.3   Detection and tracking.

The problem of detection is simply to determine whether the radar return corresponding to a particular resolution cell is due to a target or due to the normal background interference and noise. This is accomplished by comparing the radar returns from that particular resolution cell to a threshold setting that is designed to yield a specified probability of detection (P_D) and probability of false alarm (P_{fa}). The P_{fa} is the probability that the radar detector output exceeds the threshold when there is no target present. If the probability density function (pdf) of the processed radar signal is known, then the P_{fa} can be determined straightforwardly

$$P_{fa} = \int_{V_T}^{\infty} p(x)dx \qquad (15)$$

where V_T = threshold level, and $p(x)$ is the pdf.

To establish a detection threshold, estimates of the statistical parameters (e.g., mean, variance, etc.) of the processed radar returns without a target are required. This can be done using time averaging or range averaging. In time averaging, one assumes that the random process representing the radar returns from a given resolution cell is ergodic (i.e., time averaging and

25

ensemble averaging are interchangeable). The statistics are determined from a finite number of past samples from that resolution cell. In range-averaging, one assumes that the random processes representing the returns from a finite number of neighbouring range cells are identically and independently distributed.

In early radars, detection and tracking were treated as separate problems with emphasis being placed on false-alarm control. This was necessitated by the limited signal processing capability of the tracker to cope with high false-alarm rates. Much work has been done on constant false alarm rate (CFAR) processors. The objective is to ensure that a predictable and manageable false alarm rate is maintained under operational environments. There are many different configurations of CFAR processors. However, they may be divided into two general categories: (a) parametric CFAR [10,11] and (b) non-parametric CFAR [12,13].

Non-parametric CFARs are used in the case where little or no knowledge about the statistics of the signal at the detector input is available. These type of CFARs utilizes the rank statistics [14] of the test samples. Generally non-parametric CFAR maintains false-alarm rate at the expense of some degradation in detection performance.

Parametric CFARs are used in the case where the form of the probability density function (pdf) of the signal at the detector input is known or has been measured. In this case, the determination of the appropriate threshold setting for a desired P_{fa} becomes a parameter estimation problem. The simplest parametric CFAR is for detecting targets in white Gaussian noise. The pdf of the magnitude of a square-law detector with white Gaussian noise input is the exponential distribution

$$p(y) = \frac{1}{\alpha} \exp[-\frac{y}{\alpha}]$$

(16)

where α is the mean of the exponential process.

Substituting (16) into (15), the threshold is given by

$$V_T = -\alpha \ln(P_{fa}).$$

(17)

In statistical parameter estimation, there are the usual problems of determining the stationarity of the random process and ensuring that a sufficient number of statistically independent samples is used.

26

In modern radars, detection and tracking are treated as an integral problem. Because of the availability of powerful signal processing computers, modern radars can tolerate much higher false-alarm rate. Potential tracks are permitted to propagate a lot longer even though these could be false detections. False detections are eliminated after they fail to be associated with existing tracks for a number of detection intervals.

The problem of detection and tracking by HF radars differs considerably from what is encountered in microwave radars. In microwave radars, the dwell time in each direction is relatively short, in the order of several tens of milliseconds. As a result, the statistical properties of various interference components such as ground and sea clutter may be considered as stationary over a short period of time, say a few seconds to a minute.

HF radars, on the other hand, employ dwell times that range from several tens of seconds to tens of minutes. If time averaging is used to estimate the statistics, a very long time period is required because a sufficient number of statistically independent samples is needed. There is no assurance that the statistical properties of the underlying interference will remain stationary over an extended time interval. Employing range averaging is also impractical because of the large range cell sizes for most HFSWRs. To obtain enough statistically independent samples, the number of range cells required could extend to over a hundred km. An alternative is Doppler averaging. This approach is valid for Doppler regions that are dominated by external noise, which is assumed to have a white spectrum. However, there could be complications in Doppler regions that are dominated by sea clutter, because the spectrum is not flat there.

Icebergs present some unique problems in detection and tracking. First, the velocity of icebergs is in general very low, in the order of one or two knots. This means that Doppler, which normally is an effective discriminant for ship and aircraft targets, may not be as effective for icebergs. Icebergs travels with the direction of the ocean current, which at time could be chaotic. Consequently, icebergs do not always maintain a constant velocity. With long integration time, the Doppler of the iceberg may occupy a number of Doppler cells. There is an ambiguity between the case of two icebergs with slightly different velocities and the case of a single iceberg with a time varying velocity.

Second, at close-in ranges, the icebergs are frequently floating in the midst of sea ice, which is a distributed target in all three dimensions. The collective returns of the echoes from the sea ice could be comparable to that of an iceberg, but the Doppler spread of the sea ice would be substantially wider. Iceberg detection and tracking in sea ice is therefore more difficult, because there are many more possible track associations than must be considered for a single iceberg.

Ship detection presents a slightly different set of problems. The presence of first-order (Bragg lines) and higher-order spectral peaks masks targets whose Doppler happens to coincide with those of the Bragg lines or higher-order peaks. In addition, the sea-clutter peaks also affect the operation of the Doppler-averaging CFAR for targets with Doppler shifts close to these spectral peaks, because they raise the threshold level significantly. In the following a detection algorithm designed for this experiment is described. The exact implementation varies for different data sets because of the different problems encountered.

27

3.3.1 Detection algorithm.

Barrick [15] has examined the statistical properties of HF sea clutter and suggested that they are Gaussian (I and Q) distributed. If this is the case, the magnitude of the sea clutter in each Doppler bin is Rayleigh distributed and an estimate of the mean would suffice to set the detection threshold. In practice, the background returns from an HF radar contains much more than just sea clutter. The returns include atmospheric impulsive noise and co-channel radio interference. The statistical properties of these interference sources are not well understood. Furthermore, these are not stationary random processes. Rather than attempting to handle all different sources of interference, a detection algorithm has been developed based on the sea clutter and noise properties only. This means that only the mean will be estimated.

An empirical detection algorithm has been developed based on the assumption of a well behaved spectrum of the sea-clutter continuum. By well behaved we mean that there are no abrupt changes in the slope with respective to Doppler for the sea-clutter continuum spectrum. The presence of second-order peaks [16] could degrade the performance of this algorithm in terms of false-alarm rate and detection. However, this would affect mainly targets whose Doppler is close to the Bragg lines, and should not affect the detection of icebergs which have a Doppler shift very close to zero.

Figure 13 shows an idealized HFSWR spectrum with the two Bragg lines and a sea-clutter continuum.
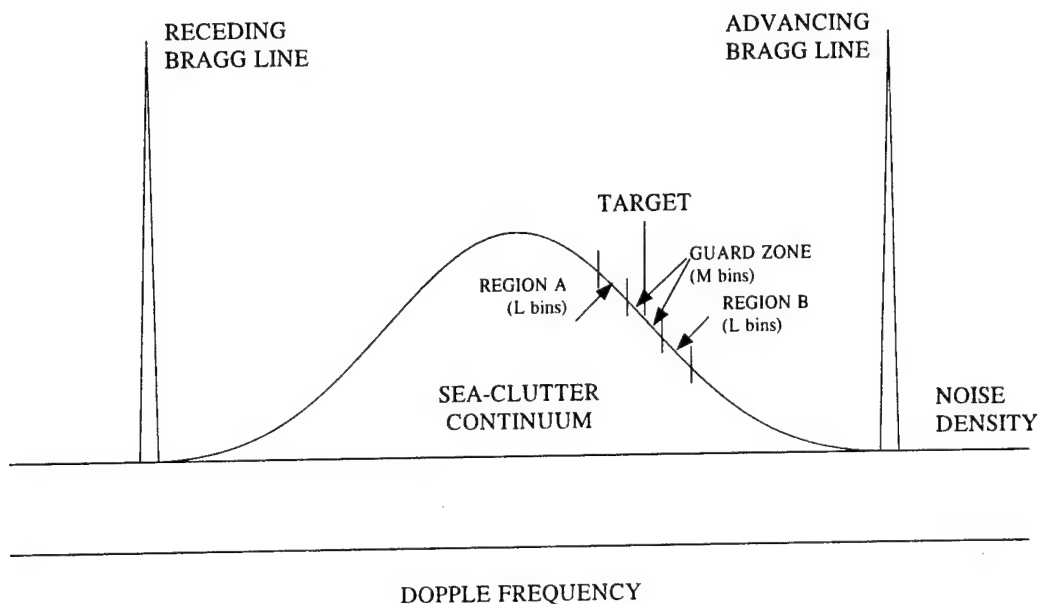
Figure 13. Illustration of Doppler-averaging CFAR.

28

To determine whether a target with a given velocity is present at a range point, we first determine the Doppler bin that corresponds to that velocity and define regions A and B on each side of the Doppler bin. Assuming that the index of the Doppler bin of interest is k, region A is defined as the group of L Doppler bins, starting from the (k-M)th bin and ends at the (k-M-L+1)th bin. Similarly region B is defined as the group of L Doppler bins starting from the (k+M)th bin and ends at the (k+M+L-1)th bin. A sample mean estimate for Doppler bin k when there is no target present is obtained by

$$<y>_{dB} = \frac{1}{2}[10\log_{10}(\frac{1}{L}\sum_{L_1}^{L_2} y_i) + 10\log_{10}(\frac{1}{L}\sum_{L_3}^{L_4} yi)] \tag{18}$$

where $L_1 = k-M$, $L_2 = k-M-L+1$, $L_3 = k+M$ and $L_4 = k+M+L-1$.

This procedure essentially computes the sample mean using two groups of L Doppler bins on each side of Doppler bin k, converts them to dB scale and then averages the two groups. The M Doppler bins separating bin k from regions A or B are called the guard zones. The purpose of the guard zone is to prevent a potential target in bin k from corrupting the sample mean estimate. The rationale for the above procedure is as follows. For a target with a Doppler shift inside the region occupied by the sea-clutter continuum, the Doppler bin in which the target appears will likely be on a spectral slope. That is, the spectral power on one side of the Doppler bin is higher than that on the other. If we simply average the values obtained from regions A and B linearly, then the sample mean estimate will be biased in favour of the side with the higher spectral power. In other words, there will always be an over estimation. Assuming that, within a small spectral region such as those of A and B, the spectral slope is approximately linear (in dB scale), a more reasonable estimate of the sample mean may be obtained by linear interpolation (in dB scale).

Having computed the sample mean estimate, the next step is to determine the detection threshold. The threshold is computed by

$$V_T = \Delta V + <y>_{dB} \tag{19}$$

where $<y>_{dB}$ is the sample mean expressed in dB, and ΔV is a quantity in dB to be added to the sample mean estimate. The value of ΔV is determined nominally by the required P_{fa}:

$$\Delta V \approx 10\log_{10}[-\ln(P_{fa})]. \tag{20}$$

The purpose of ΔV is to control the false alarm. To reduce the additional false alarms that might result from the inaccuracy of the sample mean estimate, the exact value of ΔV is determined empirically for each set of data.

The detection of targets near the Bragg lines is one of the research topics currently being pursued at DREO. Since the primary objective of the present study is iceberg detection and tracking, we shall not worry about the detection of surface targets whose Doppler happens to coincide with those of the Bragg lines. The rationale is that the probability of such a target being present is rather small. For the Cape Bonavista radar, a ship would have to be sailing at a speedy very close to 14.5 knots for it to be in the Bragg line. Nevertheless, we do want to maximize the probability of detection for ships with a Doppler that is close but not exactly equal to the Bragg lines.

Refer to Figure 14 which shows an HFSWR spectrum with a moving target (with a velocity of -10.93 knots) that is very close to one of the Bragg lines. If (18) is used directly to compute the sample mean, the result would likely be corrupted by the Doppler bins around the Bragg line, and the moving target could be missed. For the situation where the Doppler bin of interest is close to one of the Bragg lines, the sample mean is computed using the Doppler bins that are further from the Bragg line.
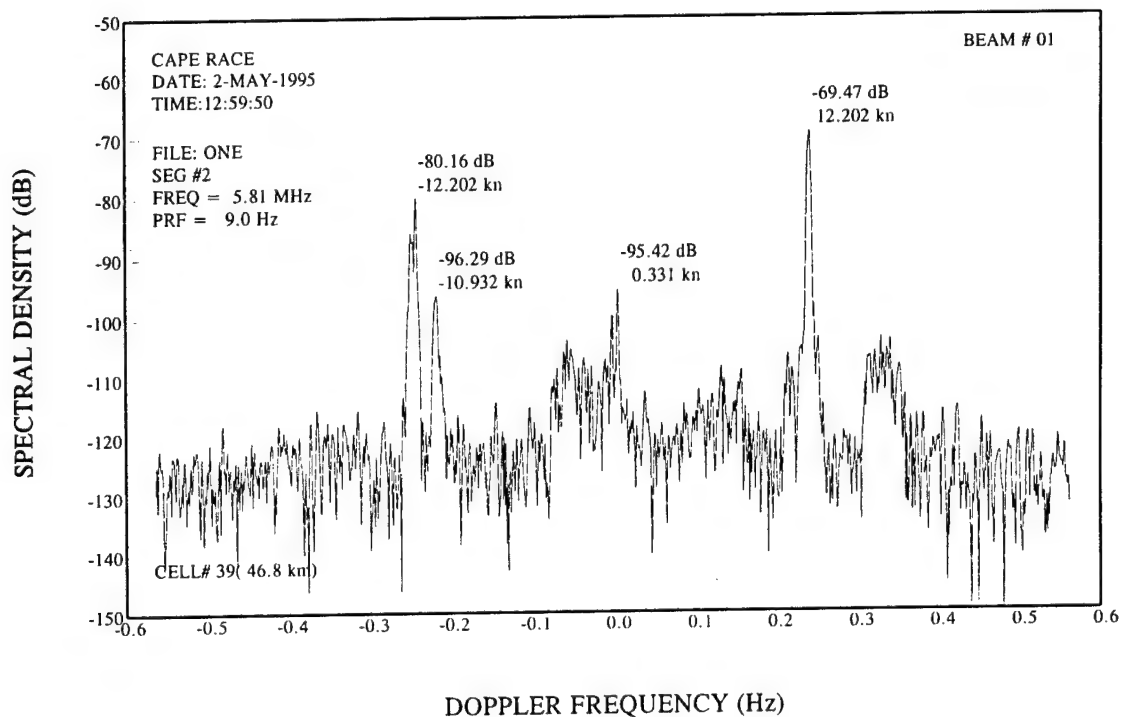
Figure 14. A ship target with velocity that is close to that of the Bragg line.

Figure 15 shows a sequence of 3-D plots for a probable iceberg target. The x-dimension is azimuth, and the y-dimension is range. Each plot represents the magnitude of a particular Doppler component as a function of range and azimuth. The largest magnitude is found in Figure 15b which corresponds to a Doppler of -0.012 Hz. Significant signal power is also found in the Doppler bin of -0.009 Hz. It can be seen that a target occupies a finite region in Doppler, range and azimuth. Since the detection threshold is set in the Doppler dimension only, the same target will be detected at neighbouring range points and azimuths as well. To eliminate multiple detections of the same target in range and azimuth, a detection is discarded unless the response is a local maximum with respect to the azimuthal, range and Doppler dimensions.

3.3.2 Tracking.

A track is a sequence of detections of the same target over a time interval. When a target is detected, there are two courses of action for a tracker to follow: (i) associate the detection with one of the existing tracks if the target satisfies a certain criterion for track association and (ii) initiate a new track if the detection cannot be associated with any existing tracks.

The information associated with a target includes most or all of the following set of parameters: range, range rate, azimuth, azimuthal rate, and acceleration. These parameters are the state variables and, collectively, are referred to as the state vector of the target. For microwave radars, sophisticated dynamic models have been developed and Kalman filtering techniques [17,18] used to enable the tracker to follow fast manoeuvring targets. For HF radars, sophisticated dynamic models of targets are not often used because the required accuracy of state-variable estimates is not achievable. For example, because of the relatively coarse azimuthal resolution and the long coherent integration time, the estimates of the bearing and its rate of change are usually not very accurate.

We use a simple closest-neighbour criterion for track association. The state variables comprise range, Doppler (range rate) and azimuth only. For each detection, estimates of the range, azimuth and Doppler of the target are obtained. The radial velocity of the target is calculated from the Doppler frequency, from which an estimate of the target range in the next detection interval is obtained. Since we have information on range rate only, movement of the target in the azimuthal dimension cannot be measured directly. This information can be obtained indirectly over several detection intervals. However, because of the long coherent integration period employed, the estimation of the target bearing at the next detection interval will not be very accurate, particularly if the tangential velocity of the target is high.

Let a target detected in the jth integration period be represented by the state vector $\{R_j, \theta_j, f_D^j\}$. Assuming that the change in Doppler and bearing of the target is small between two successive detection intervals, an initial estimate of the state vector of this target at the next detection interval may be obtained as

$$\{R_j + v\Delta T, \theta_j, f_D^j\}.$$

where $v = -f_D\lambda/2$ and ΔT is the elapsed time between two detection intervals.

31
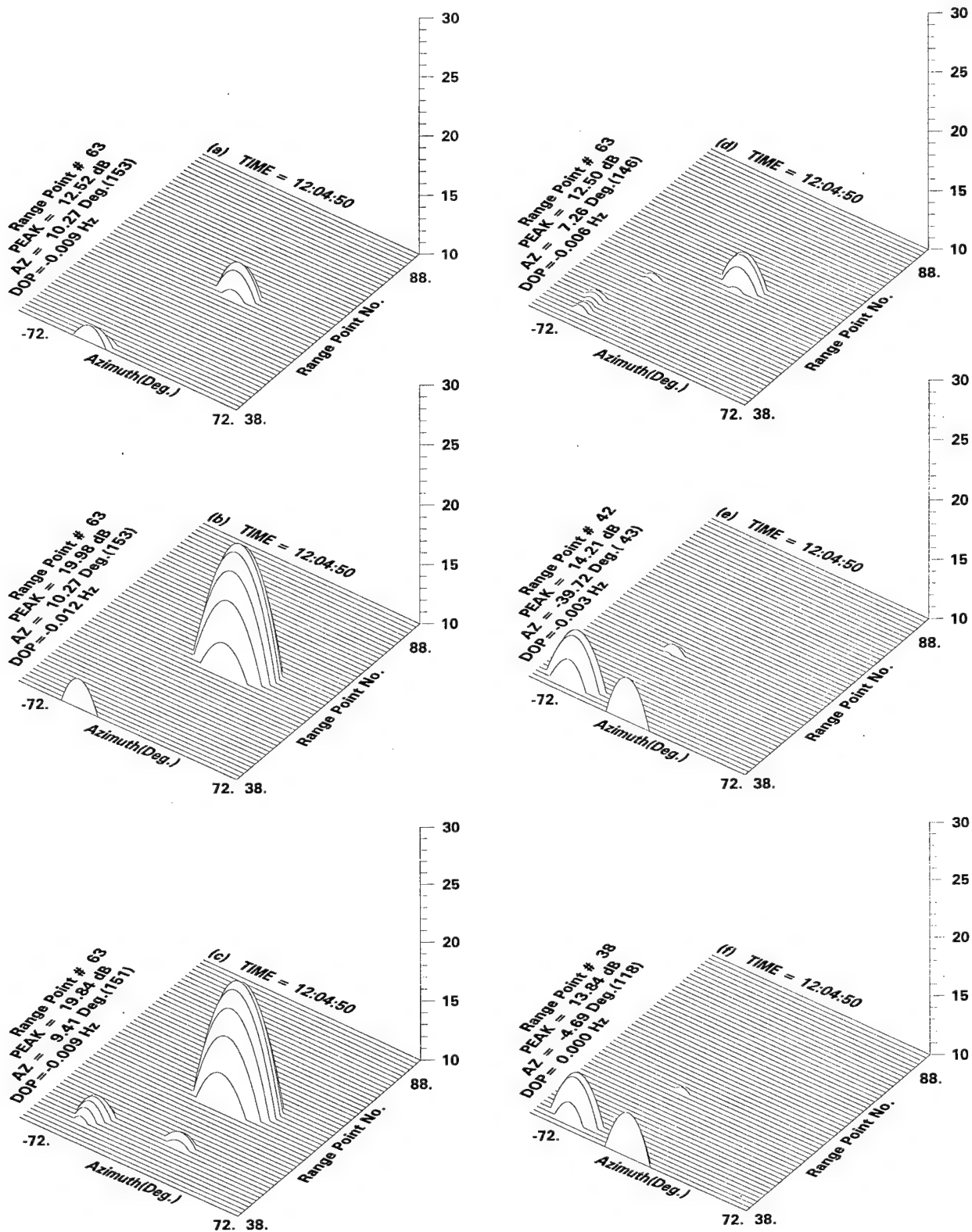
Figure 15. Location of a target in 3-dimensional space.

A target detected in the next detection interval having a state vector $\{R_{j+1}, \theta_{j+1}, f_D^{j+1}\}$ will be associated with this target if the following conditions are satisfied:

$$\left| R_{j+1} - (R_j + v_j \Delta T) \right| \leq \Delta R$$

$$\left| \theta_{j+1} - \theta_j \right| \leq \Delta\theta$$

$$\left| f_D^{j+1} - f_D^j \right| \leq \Delta f_D.$$

The purpose of parameter ΔR is to accommodate random errors that may be present in the range estimate. Parameter $\Delta\theta$ is used to accommodate the unknown azimuthal movement of the target as well as random errors in the azimuth estimate. Parameter Δf_D is used to accommodate random errors in the Doppler estimate as well as small changes in the target velocity. These parameters are determined empirically.

3.4 Estimation of the target radar cross section.

Theoretically, the radar cross section of a target may be estimated from the received echo power through the radar equation. The monostatic HF surface wave radar equation is defined as [19]

$$P_r = \frac{P_t G_t G_r \sigma \lambda^2}{(4\pi)^3 R^4 L_N^2 L_s} \tag{21}$$

where P_t is the peak transmit power; G_t and G_r are the gains of the transmit and receive antennas, respectively. λ is the radar wavelength, R is the range, and L_N and L_s are the one-way Norton surface wave propagation loss and system loss, respectively.

Because the data are in the form of digital samples, precise calibration is required to translate the numerical values into physical quantities from which the radar cross section can be estimated. Extreme care must be exercised when one is dealing with gains and radar cross section in the context of HF surface wave radar because of the non-uniform usage of the definition of these terms [20-22]. This is particularly important when one tries to obtain estimates of parameters using works of different researchers.

For HF surface-wave radars, there is a convenient way in which one can bypass the precise calibration and obtain a first order estimate of the target RCS provided certain conditions are satisfied. The viability of this method is a consequence of the fact that the dominant component of the HF radar echo from the sea are the first order Bragg components, for which the scattering coefficients have been theoretically derived. Barrick [23] has modelled the Bragg sea-clutter components as two delta functions in the Doppler domain

33

$$\sigma^1(\omega)=2^6\pi k_o^4[S(-2k_o)\delta(\omega+\omega_B)+S(2k_o)\delta(\omega-\omega_B)] \qquad (22)$$

where ω is the angular Doppler frequency, $\omega_B = 2\pi f_B$ is the angular Bragg frequency, $k_o = 2\pi/\lambda$ is the radar's wave number, and $S(.)$ is the non directional wave-height spectrum. He also calculates the theoretical scattering coefficient of the Bragg components to be -17 dB m^2/m^2, independent of radar frequency within the HF band.

This value of σ^o for the Bragg lines is calculated by integrating (22) over the Doppler domain, assuming a fully developed sea (see [23] for details):

$$\sigma^o=\frac{1}{2}\int_{-\infty}^{\infty}\sigma^1(\omega)d\omega. \qquad (23)$$

The non-directional wave-height spectrum $S(k)$ is a function of the ocean wave number k which is related to the angular Doppler frequency through the gravity wave dispersion relation [24]:

$$\omega^2=gk \qquad (24)$$

where $g = 9.81$ m/sec^2 is the gravitational acceleration; $k = 2\pi/L$ is the ocean wave number; and L is the ocean wave's wavelength.

There is some confusion as to whether the value of σ^o should be -17 dB or -20 dB. Barrick uses the Phillips wave-height spectral model for $S(k)$

$$S(k)=\frac{B}{2\pi k^4} \qquad (25)$$

for $k > g/u^2$;

$$\equiv 0$$

for $k < g/u^2$.

where u is the required wind speed for a fully developed sea, discussed in the next paragraph. Indeed, in Equation (12:22) of [23], if a numerical value of B= 0.005 is used in the Phillips model (as did Barrick), one would get a value of -20 dB. Howell[1] may have resolved this

---

1. Private communication with Dr. R. Howell of Raytheon Canada.

discrepancy by tracing the ambiguity to one of Barrick's earlier works [25] in which it was noted that a nonstandard definition of power spectral density was used. The value of σ^o for the Bragg components is widely quoted; however, there is sufficient evidence that the correct value of σ^o for the Bragg lines should be -20 dB. In subsequent discussions, we shall use -20 dB as the scattering coefficient of the Bragg components under the condition of a fully developed sea.

A sea is considered fully developed for an HF radar operating at a given frequency if the gravity waves that give rise to the Bragg lines at that radar frequency reach steady state. The minimum speed of the wind that sustains the gravity waves for a given radar frequency $f_c = c/\lambda$ is determined by

$$u = [\frac{g\lambda}{4\pi}]^{\frac{1}{2}}.$$

(26)

The value of σ^o = -20 dB includes the ground plane effect of the transmit and receive antennas. The ground plane effect refers to the doubling of the field intensity (or the quadrupling of the power flux density) when an antenna radiates a signal above a conducting ground plane. The power flux density observed at a point in the far field would be four times (6 dB) that of the same antenna if it were radiating into free space. A target with a certain radar cross section, σ, intercepts the signal and re-radiates it back to the radar. If the target is also above a conducting ground plane the radar receive antenna will see a signal power flux density that is 6 dB greater than if the target were re-radiating into free space. Teague [26] obtained an estimate of σ^o for the Bragg components which differs from Barrick's result by about 12 dB. This difference is accounted for by the ground plane effect. Thus -32 dB is the nominal free-space value of the scattering coefficient of the Bragg lines under the conditions of a fully developed sea.

Returning to the problem of the estimation of the RCS of icebergs, a first order estimate of the RCS of a point target with constant velocity may be obtained from the energy in the Doppler components of the target relative to that of the Bragg lines. The rationale is as follows: Since the area of a HF radar resolution cell is generally very large, an iceberg may be considered as a point target.

Let σ_B^o be the scattering coefficient of the Bragg components. The corresponding equivalent RCS of the Bragg components for the resolution cell is given by

$$\sigma_B = \sigma_B^o R\theta \frac{c\tau}{2}$$

(27)

where R is the range, τ is the pulse length and Θ is the antenna azimuthal beamwidth. After coherent integration the radar equation may be expressed in terms of signal energy

$$E_s = \frac{P_{av}G_tG_r\sigma T_i\lambda^2}{(4\pi)^3R^4L_N{}^2L_s} \qquad (28)$$

where P_{av} = average power and T_i is the coherent integration time.

Equation (28) applies to both Bragg lines as well as a constant-velocity target. For the Bragg lines, we have

$$E_B = \frac{P_{av}G_tG_r\lambda^2 T_i\sigma^\circ R\theta\frac{c\tau}{2}}{(4\pi)^3R^4L_N{}^2L_s}. \qquad (29)$$

For a constant velocity target with a RCS σ_T, we have

$$E_T = \frac{P_{av}G_tG_r\lambda^2 T_i\sigma_T}{(4\pi)^3R^4L_N{}^2L_s}. \qquad (30)$$

Hence the ratio of the signal energy between a constant velocity target and the Bragg lines is equal to

$$\frac{E_T}{E_B} = \frac{\sigma_T}{\sigma^\circ{}_B R\theta\frac{c\tau}{2}}. \qquad (31)$$

Solving for σ_T, the RCS of a constant velocity target may be estimated by

$$\sigma_T = \frac{E_T}{E_B}\sigma^\circ{}_B R\theta\frac{c\tau}{2}. \qquad (32)$$

36

The values of E_B and E_T are obtained from the Doppler spectrum as follows: The nominal Doppler frequency of the Bragg lines is given by (5). However, the exact value may deviate from the nominal value because of (a) the displacement of the Doppler spectrum due to ocean current, and (b) the normal variation in the Bragg resonance frequency.

To obtain E_B, we determine approximately the indices of the Doppler bins that correspond to the advancing and receding Bragg lines given by (5). The Doppler bins that are local maxima around the nominal Bragg frequencies are located. E_B is calculated as the total energy contained in a number of Doppler bins around these two local maxima. The number of Doppler bins used in the calculation of E_B is not very critical. Generally, most of the energy is contained in a small number of bins (3 to 5) around each maxima (it depends on the Doppler resolution).

To obtain E_T, we sum the energy of a number of Doppler bins around the one that contains the target. For a constant velocity target, most of the energy is contained within 3 to 5 Doppler bins around the spectral peak of the target. Three is the minimum number that should be used because of the spreading that arises from the use of data windows in the Doppler processing.

There are several conditions that one should be aware of in regard to (29). The first is that the energy in the Bragg lines fluctuates over time. Consequently, the value of E_B should be averaged over a number of spectra to ensure that temporal fluctuation in the Bragg energy estimate is minimized. Figure 16 shows the Bragg energy vs. range profile computed from one Cape Bonavista data file on April 30, 1995. The coherent integration period was 9.56 minutes. It shows large magnitude swings among some neighbouring ranges. Figure 17 shows the Bragg energy as a function of range after averaging over 24 profiles (over a time interval of about 6 hours). It can be seen that the fluctuation in the Bragg energy among neighbouring range cells has been significantly reduced.

The second condition is that the sea should be fully developed in the area of interest. This condition is usually satisfied if the wind with speed exceeding that given by (26) has been blowing in the area of interest for several hours prior to the time when the data are collected. In the absence of any knowledge of whether the sea is fully developed, σ^0_B should only be regarded as the upper bound of the equivalent scattering coefficient of the Bragg lines.

Finally the signal-to-noise ratio must be sufficiently high so as to minimize the effect of noise on the estimate. However, this condition is automatically satisfied for target magnitudes that exceed the detection threshold.

37
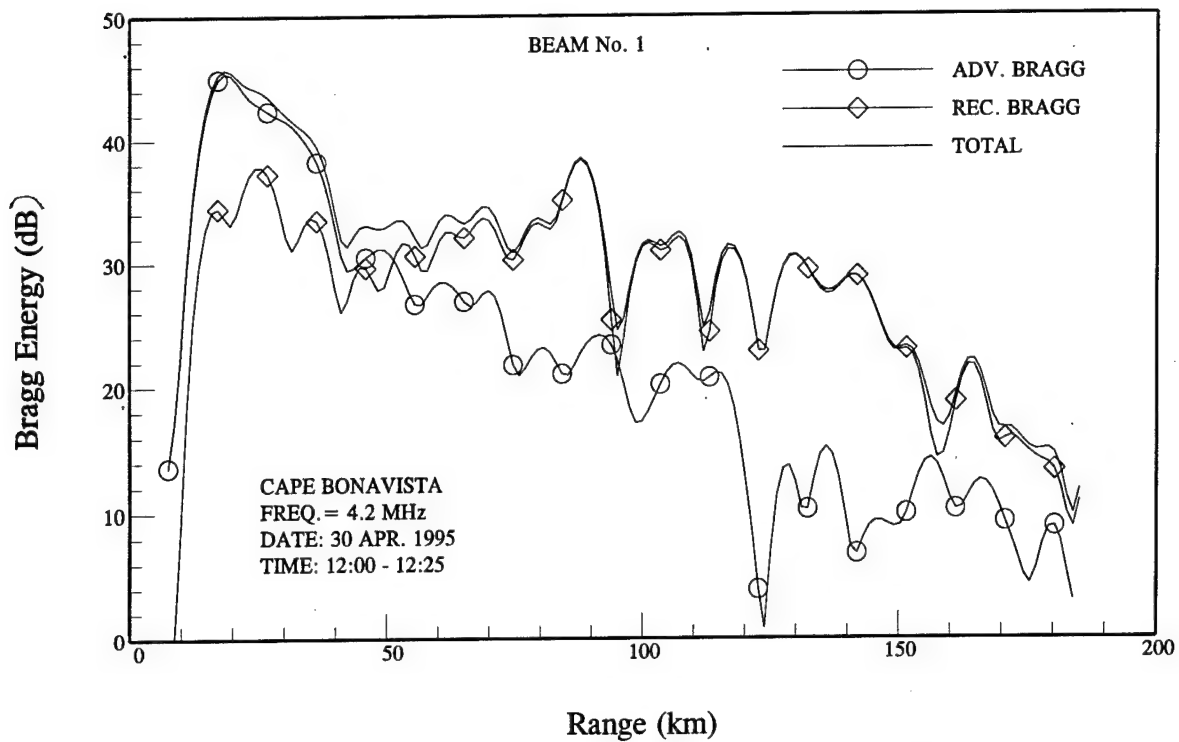
Figure 16. Short-term Bragg energy vs. range profile.
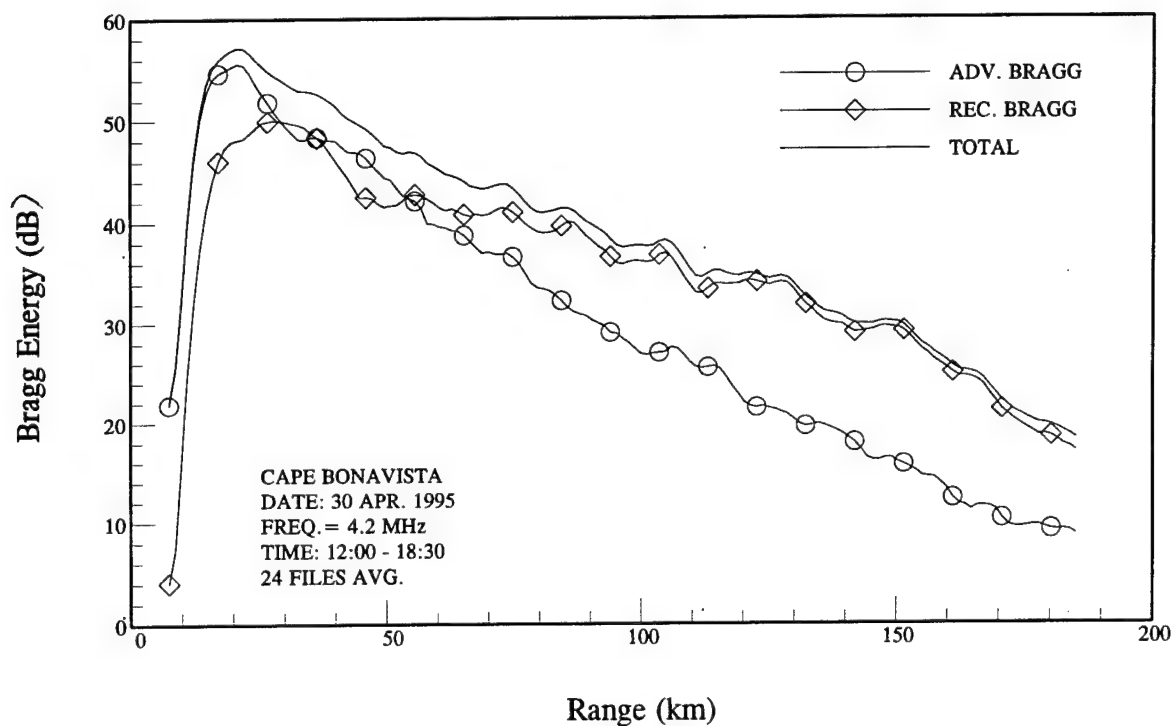
Figure 17. Averaged Bragg energy vs. range profile.

38

4. TRIAL RESULTS.

In this section, we present the results of the analysis of all the HFSWR data collected in BERG SEARCH '95. The results are presented in three separate sub-sections: (i) for 30 April, 1995, (ii) for 2 May, 1995 and (iii) for 25 July 1995. Both RCL and NR collected data on April 30, 1995. Only NR collected data on May 2, 1995, and RCL later went back to Cape Bonavista in July 1995 and collected additional data. Strictly, the July 25 experiment was not part of BERG SEARCH '95, and there are no ground-truth data for that trial.

4.1 Results for 30 April, 1995.

(a) Cape Bonavista data.

Raytheon Canada carried out the experiment on April 29 and 30 only. The data collected on April 29 were for testing purposes. Hence only the results from 30 April are presented in this section. The starting time of the segmented data files are tabulated in Table A.1 of Appendix A. Each of these files represents a time interval of 573.4 seconds. The time is Newfoundland local time.

The data were processed according to the procedure described in Section 3.2. A couple of items are noted. The first is that the sign of the Doppler estimated from the Cape Bonavista data is unconventional. Normally a positive Doppler should indicate an approaching target and vice versa. For the Cape Bonavista data a positive Doppler was associated with a receding target. This was attributed to the frequency of the local oscillator signal employed in down converting the signal to the i.f. stage. This affects the velocity estimate used by the tracking algorithm to predict the position of the target in the next detection interval. This problem was corrected by switching the sign of the Q-channel data before processing.

The second item is that Raytheon personnel reported a significant amount of sea ice in the area, during the experiment on April 30.

The CFAR parameters (see Section 3.3.1) used in processing the Cape Bonavista data were as follows:

No. of Doppler cells in guard zone: $M = 8$;
No. of Doppler cells used in sample mean estimate = 16;
Threshold level = 15 dB above the sample mean.

The detection data were then processed by the tracking algorithm for track initiation and track association.

The boresight of the receive array at Cape Bonavista points nominally at $110°$ clockwise from true north. The separation of the antenna element was 38.45 m. The signals from the eight receiver channels were used to synthesize digitally beams covering a $120°$ sector about the boresight.

39

A partial set of ground-truth data for Cape Bonavista on the day of April 30, 1995 is shown in Figure 18. This plot was provided by Ice Centre Ottawa and was obtained by processing visual and radar data of Atlantic Airways. The triangular symbols represent sighted icebergs, and the circular symbol with a cross inside are unknown radar contacts.

The accumulated HFSWR track plot for Cape Bonavista on April 30, 1995 between the times of 12:04:50 and 18:25:13 is presented in Figure 19. It shows seven clusters of detections. These are listed in Table 3.

Table 3: Estimated position of targets detected by the Cape Bonavista HFSWR on April 30.

Target No.	Range (km)	Range (n.mi.)	Az. (Deg. w.r.t. True North)	Vel. (kn)	Magn. (dB)	LAT.	LONG.
1	16.8	9.1	110.22	0.00	42.4	48:38:06N	52:52:31W
2	27.6	14.9	77.57	0.00	17.8	48:44:25N	52:43:20W
3	27.6	14.9	111.63	0.00	20.6	48:35:43N	52:44:27W
4	27.6	14.9	132.91	0.00	19.2	48:31:05N	52:48:55W
5	74.4	40.3	121.26	-0.11	13.3	48:20:08N	52:13:33W
6	116.4	62.9	104.79	0.01	5.8	48:24:36N	51:33:50W
7	135.6	75.3	97.19	-0.35	1.6	48:30:54N	51:12:36W

There is good agreement between the positions of targets No.1 and No. 5 in Table 3 and the ground truth data in Figure 18. For target No. 1, the bearing is 110.22° and the range is 9.07 n.mi. There is an iceberg in Figure 18 with a bearing of 111° and a range of about 10 n.mi. For target No.5 in Table 3, the bearing is 121.26°, and the average range is 40.31 n.mi. In Figure 18, there is an iceberg with a bearing of 122° and a range of 41 n.mi. The small discrepancy in range and bearing may be attributed to the fact that the Cape Bonavista radar had not been calibrated and that the range and azimuthal resolutions are rather coarse.

There are no icebergs in Figure 18 that correspond to targets No.2, No.3 and No.4. These detections have been examined carefully, and it is conjectured that these are ground-clutter returns coming from the antenna sidelobes. This is plausible because the Doppler shifts of these target are zero, and these detections are at a relatively short ranges. Similar detections were obtained in the 25 July data. It is unlikely, if these were icebergs, that they would remain in the same locations relative to one another for an extended period of time.
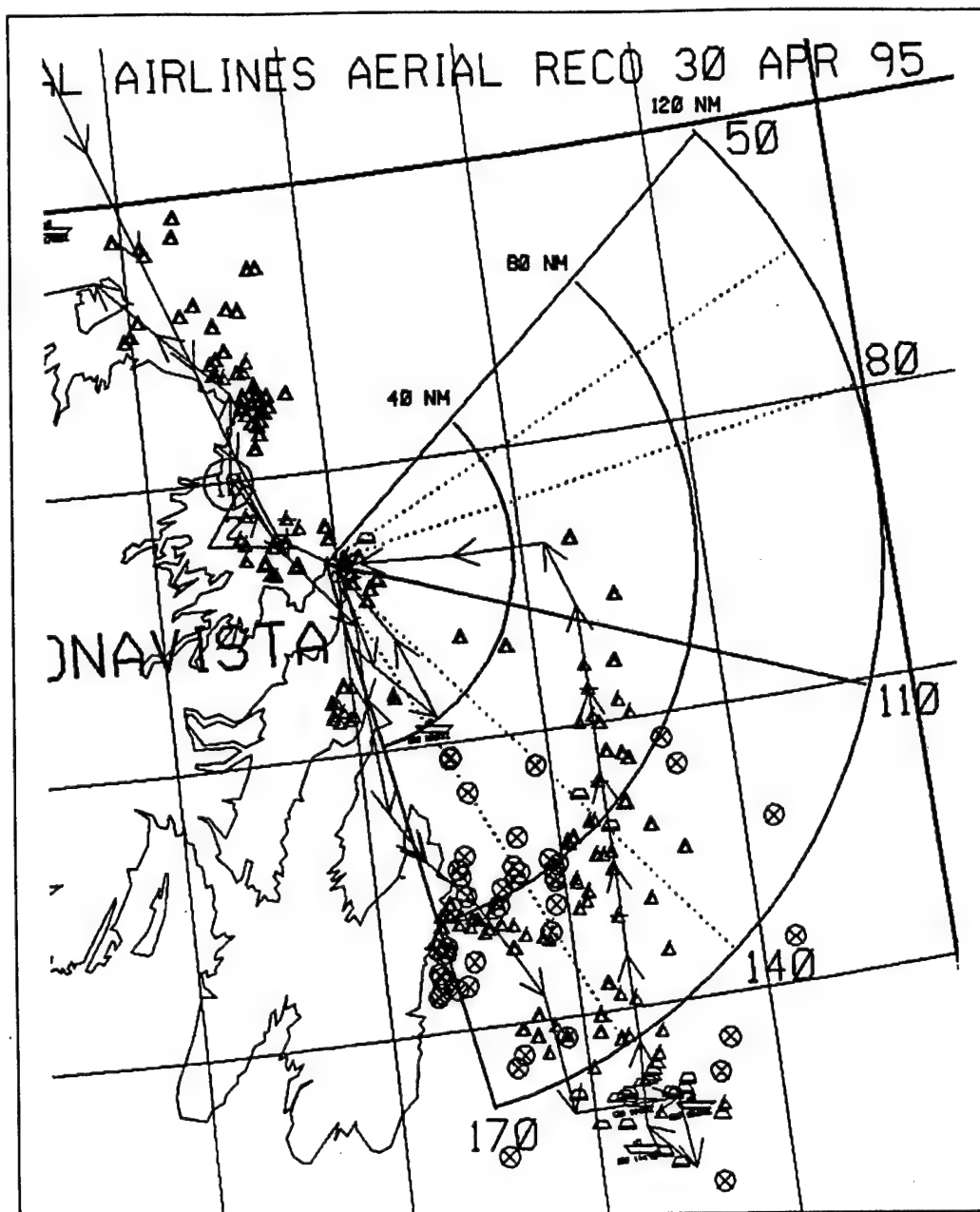
Figure 18. Ground truth data for Cape Bonavista on 30 April, 1995.
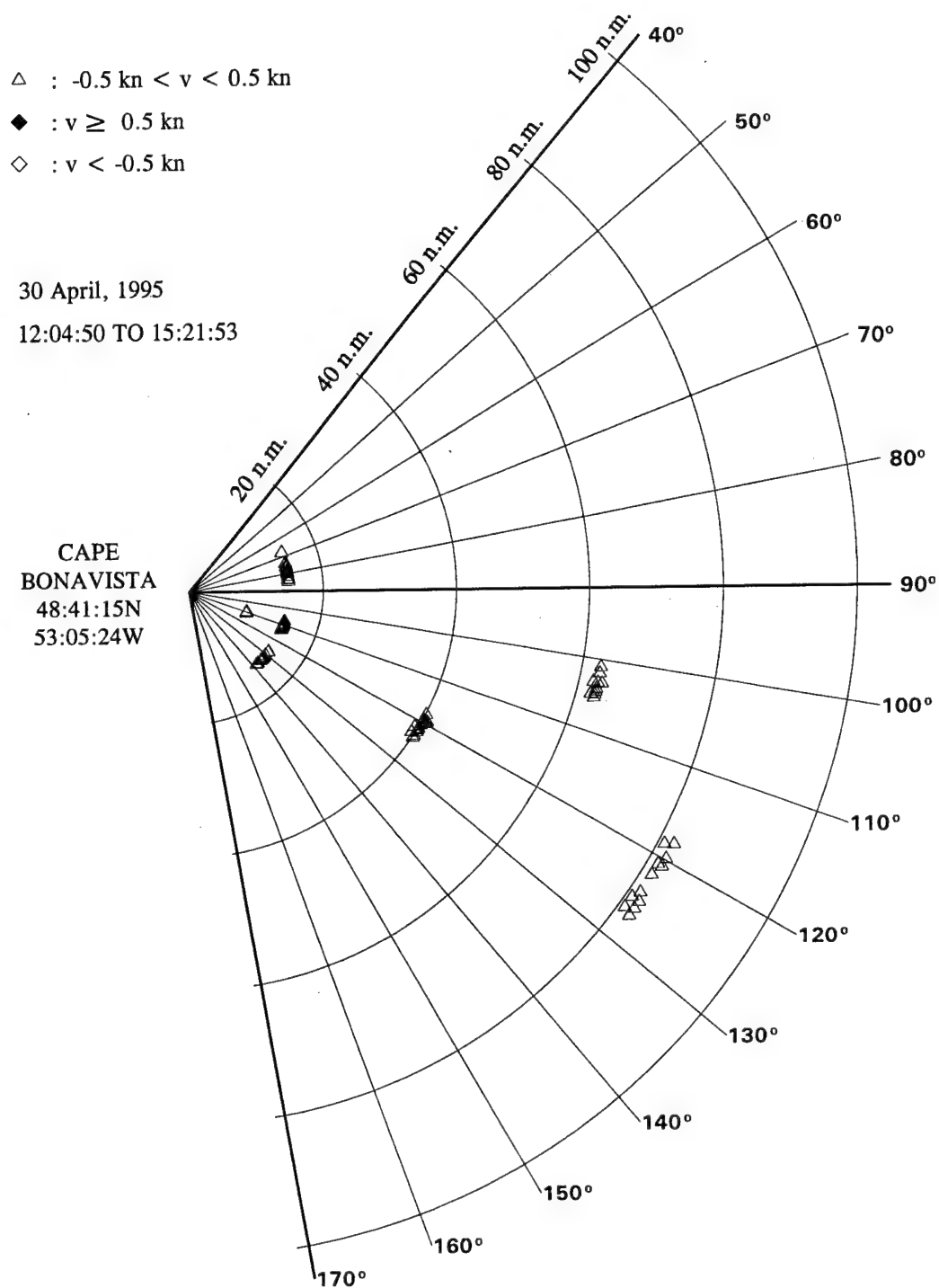
Figure 19. Accumulated track plot for Cape Bonavista on 30 April, 1995.

The detection of targets No.6, No.7 were intermittent in that occasionally the signal dipped below the detection threshold resulting in discontinuous tracks. Nevertheless, these are legitimate detections. There is an iceberg in Figure 18 that corresponds to target No.6 in Table 3. This iceberg is at approximately 105° and a range of 60.54 n.mi.

Figure 20 shows the average energy of the Bragg components (i.e., parameter E_B in (28)) as a function of range for Cape Bonavista on 30 April, 1995. The individual plots in Figure 20 are for the various beam pointing directions. The average Bragg energy for each range cell was obtained by summing the squared magnitudes of the five Doppler bins about the one that corresponds to the nominal Bragg frequencies given by (5). It can be seen that Bragg energy was at a maximum in the direction of Beam No. 6 (-44.14°). In addition, the advancing Bragg component was substantially higher than the receding Bragg, which indicates that the wind was blowing against the direction of Beam No.6.

Since the value of σ_B° = -20 dB was derived assuming the condition of a fully developed sea, it represents an upper limit for the scattering coefficient of the Bragg components. As we have no information with regard to the sea state at each location, we assume that an area of the sea is closer to being fully developed if the Bragg energy in that area is the highest compared with other areas at the same range. A composite Bragg energy versus range profile was constructed by taking the maximum value among the Bragg energies from all eight beams at a given range cell.

Barrick combined three types of losses pertinent to the HF surface wave radar equation into a quantity called the total propagation loss [27]. The three types of losses are (a) the basic propagation loss due to the spherical dispersion of a signal radiating from a source, (b) the Norton surface wave attenuation and (c) loss due to increased surface roughness at higher sea states.

The power density at a distance R from an isotropic source is

$$\Phi = \frac{P_t}{4\pi R^2}.$$

(33)

The equivalent aperture area of an isotropic antenna is

$$A_e = \frac{\lambda^2}{4\pi}.$$

(34)

If an isotropic antenna is placed at a distance R from the source, the received power is equal to
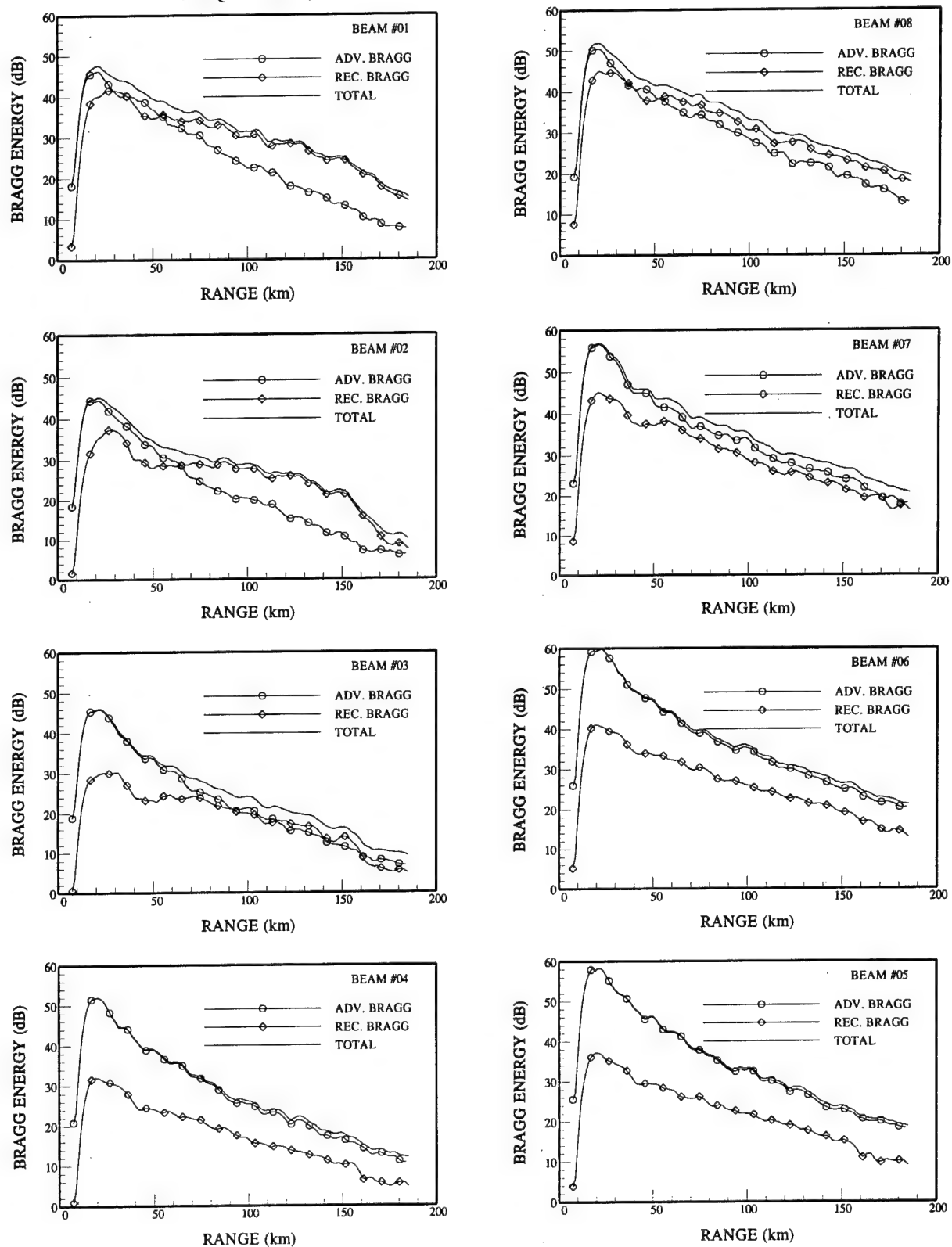
Figure 20.   Average Bragg energy as a function of range for Cape Bonavista on 30 April, 1995.

$$P_r = P_t \left(\frac{\lambda}{4\pi R} \right)^2. \tag{35}$$

The basic loss incurred by the propagation path is equal to the ratio between P_t and P_r

$$L_B = \left(\frac{4\pi R}{\lambda} \right)^2. \tag{36}$$

Hence the total loss is equal to

$$L_T = L_B L_N L_{ss} \tag{37}$$

where L_N is the one-way Norton surface wave attenuation, and L_{ss} is the sea state loss.

The sea state loss L_{ss} has not been taken into account in (21), however, the basic transmission loss L_B and the Norton surface wave attenuation L_N have. Identifying the quantities in (21) associated with L_T, the radar equation becomes

$$P_r = \frac{P_t G_t G_r \sigma 4\pi}{L_T^2 L_s \lambda^2}. \tag{38}$$

Barrick tabulated L_T for various frequencies and sea states. The 6 dB one-way ground plane effect is incorporated in the tabulated data, that is, the basic transmission loss becomes $L_B = (2\pi R/\lambda)^2$. These data are widely used in the HF surface radar community.

Here is where caution must be exercised in applying (38). If tabulated data for L_T from other sources are used, one must determine whether the data were derived by assuming $L_B = (4\pi R/\lambda)^2$ or $L_B = (2\pi R/\lambda)^2$. If the data were calculated by assuming $L_B = (2\pi R/\lambda)^2$, the so-called free space values (i.e., gains without the ground plane) must be used for G_t and G_r. If the data were calculated by assuming $L_B = (4\pi R/\lambda)^2$, then the actual gains[*] of the antennas must be used.

---

[*] We have not considered the ground proximity effect on the antenna gains discussed by Shearman in [20]. The ground proximity effect refers to the reduction in gain from the free-space value due to mutual coupling between the antenna and its image as its distance to the ground plane decreases. A 3 dB reduction will result if the antenna is on the ground plane.

Although we did not have ground-truth data regarding the sea surface, some indication of whether there is a significant degree of variation in the sea-surface condition in different areas of the sea can be obtained by comparing the Bragg energy with the propagation loss as a function of range. Assuming that the sea is fully developed at distances beyond a few tens of km, the equivalent RCS of the Bragg components should increase directly with range because the size of the range cell increases directly with range. This offsets some of the propagation loss. Therefore, one should observe a slightly lower rate of attenuation of the Bragg energy as a function of range compared with the propagation loss.

The Bragg energy versus range profile for Cape Bonavista on 30 April, 1995 is shown in Figure 21 together with the propagation loss curves for 4 MHz at sea states 1 and 6. The Bragg energy derived from the experimental data is not calibrated, and its value is expressed in dB with respect to the numerical value of unity. However, it is plotted within the same dynamic range as those for the propagation loss curves so that the rates of attenuation with respect to range can be visually compared. Indeed it shows a slightly lower rate of attenuation as a function of range for the Bragg energy compared with that of the propagation loss.

The data in Figure 21 were smoothed and used to obtain estimates of the target RCS (see Section 3.4). As an example, target No.5 in Table 3 was located at a range of 74.4 km, and the average received energy was 13.3 dB. From Figure 21, the Bragg energy (E_B) at 74.4 km was determined to be about -40 dB. Hence the average energy (E_T) of target No.5 was 26.7 dB below that of the Bragg energy. The effective RCS of the Bragg component for the Cape Bonavista HFSWR at 74.4 km was determined from (26) to be about 60.85 dBm^2, assuming $\sigma_B^\circ = -20$ dB, an azimuthal beamwidth of 12.5° and a range-cell size of 7.5 km. The estimated value of the RCS of target No.5 is, therefore, 34.15 dBm^2 (i.e., 60.85 - 26.7). Since the value of $\sigma_B^\circ = -20$ dB includes the ground-plane effect, the free space RCS of target No.5 is 34.15 - 12 = 22.15 dB. This represents a large iceberg.

(b)   Cape Race data.

The receive array at Cape Race points nominally at 121° clockwise from true north. To obtain coverage of the area where the icebergs were, the sub-arrays were electronically steered to form an elemental pattern pointing nominally at 91° clockwise from true north. The signals from the 10 receiver channels were then used to synthesize beams that span a sector of approximately 35° about boresight.

The data storage capacity of the Cape Race radar permitted the continuous recording of data for about 45 minutes. The data were processed as described in Section 3.2. There were only three files collected on April 30, 1995 at Cape Race, covering the time interval between 12:45 and 15:04. Each data file provided data for three detections. The starting times of the segmented data files are listed in Table A.2 of Appendix A.

The preliminary track plot for Cape Race on April 30, 1995 between the times of 12:45:04 and 15:04:49 is presented in Figure 22. It shows both surface-ship and probable iceberg targets. Ship targets are indicated by their relatively high speed. For example, a sequence of
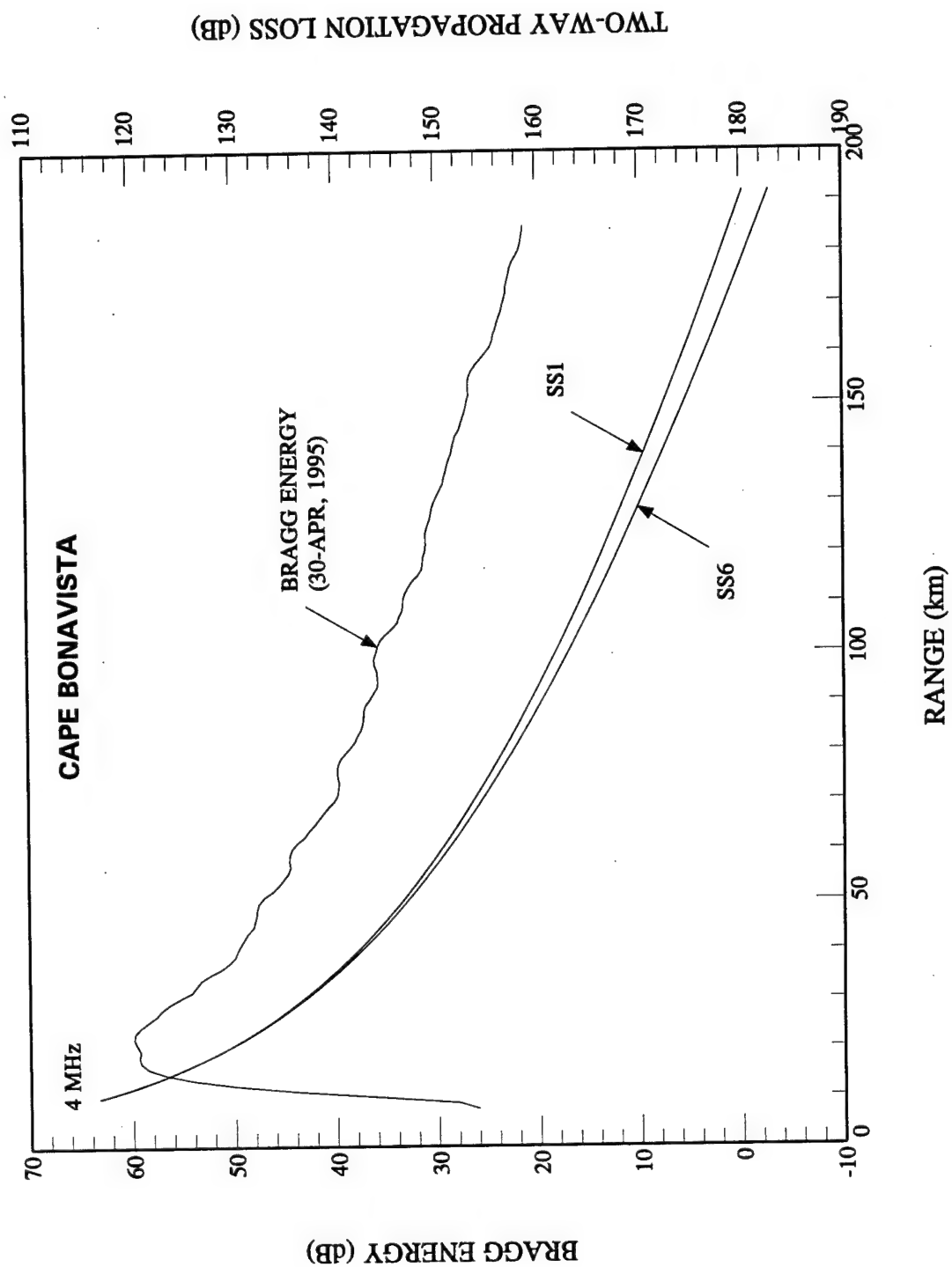
46

Figure 21. Bragg energy at Cape Bonavista on 30 April, 1995 and propagation loss as functions of range at 4 MHz.

47
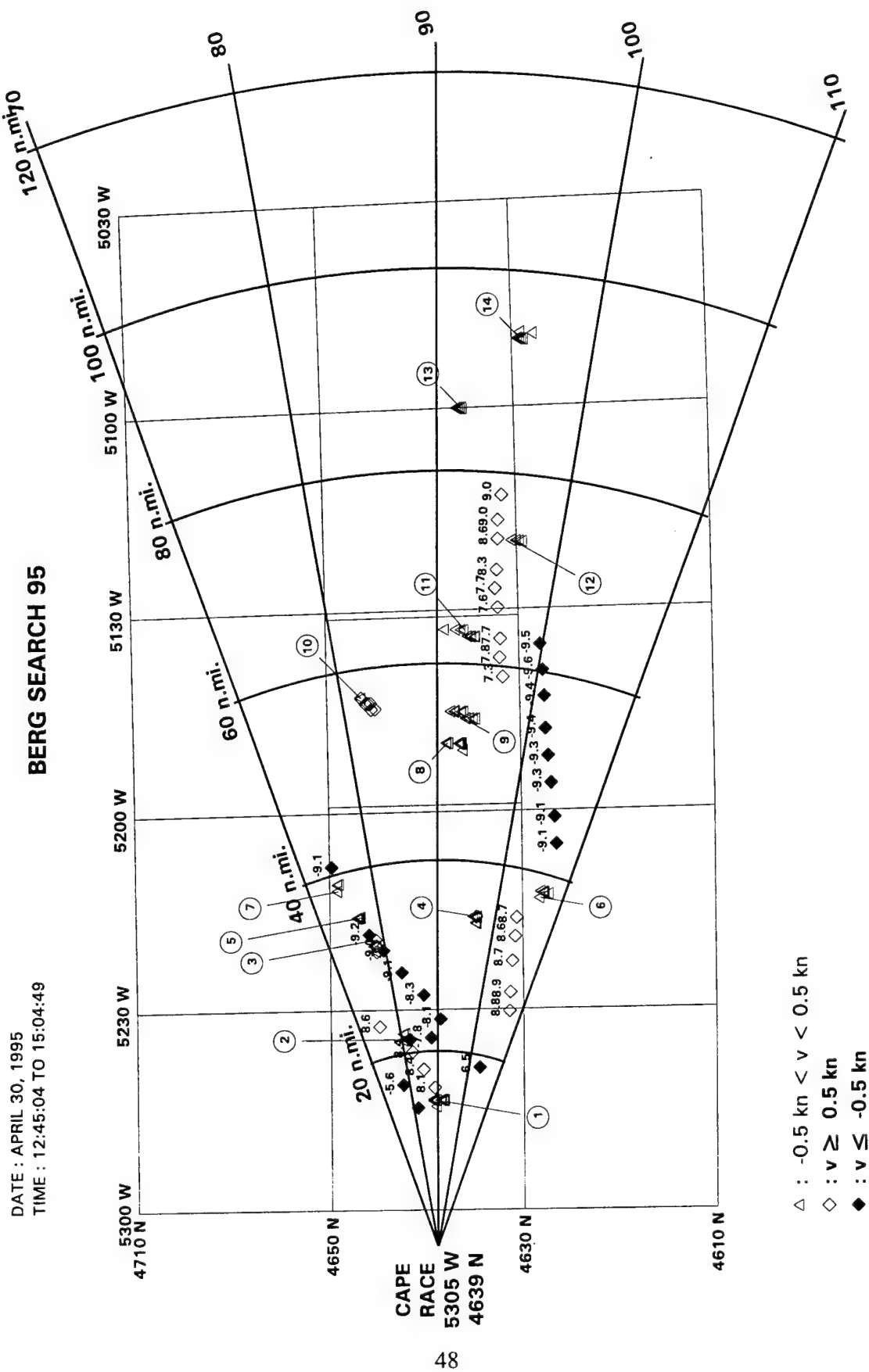
Figure 22. Preliminary track plot for Cape Race on 30 April, 1995.

detections on a target with a nominal velocity of 9 knots is shown around the 46:30N latitude, starting from a range of about 40 n.mi. (at 12:45:04) to about 64 n.mi. (at 15:05:49).

Figure 23, which was provided by Atlantic Airways, shows the ground truth at Cape Race on 30-APR-1995. The square box defined by the latitude-line pair of (46:30N, 46:50N) and longitude-line pair of (51:31W, 51:59W) is an area where surface ground truth was collected. The Canadian Coast Guard Ship CCGS Sir Wilfred Grenfell was stationed there. Its position is indicated in Figure 23 by the black dot designated CCG. The Grenfell was detected and tracked throughout the period of observation. This determination was based on the following estimates. Ground-truthed positions of the Grenfell provided by AES ISS are tabulated in Table 4, together with the values of its range and bearing with respect to Cape Race. The latitude and longitude of Cape Race are 46:39:01N and 53:05:25W, respectively.

Table 4: Ground-truthed positions of CCGS Sir Wilfred Grenfell on April 30, 1995.

Time	Latitude	Longitude	Range (km)	Bearing (w.r.t. Boresight)
12:00	46:43N	51:46W	101.16	-5.65°
13:00	46:42N	51:46W	101.07	-4.60°
14:00	46:41N	51:47W	99.69	-3.57°
15:00	46:40N	51:47W	99.67	-2.51°

Table 5 lists the positions, at various times, of a target closest to the reported position of the Grenfell. Based on the measurements at the approximate times of 13:00, 14:00 and 15:00 respectively, the average range is about 1 km from that of the reported position; and the averaged bearing differs from that of the Grenfell by about 5.68°.

The magnitudes of the echoes from this target were substantially greater than those from other close-by targets; and the positions of other targets do not match as well as this one. Hence there is a high probability that the target described in Table 5 was indeed the Grenfell. This indicates that there was a beam-pointing error of about -5.68° for the Cape Race HFSWR. Instead of the theoretical boresight of 91° from true north, it should have been 85.32°.

This correction was made to the azimuth estimate of all detected targets. In addition the detections were corrected for azimuthal ambiguities. This was done by checking for discontinuities in the tracks. For example, in Figure 22, the track of a ship steaming towards the radar at a velocity of +8.7 knots terminates near the position of (46:30N, 52:30W), while another track with similar attributes was initiated in the next detection interval at about (46:45N, 52:32W). The measurements obtained by the radar on this target are summarized in Table 6.
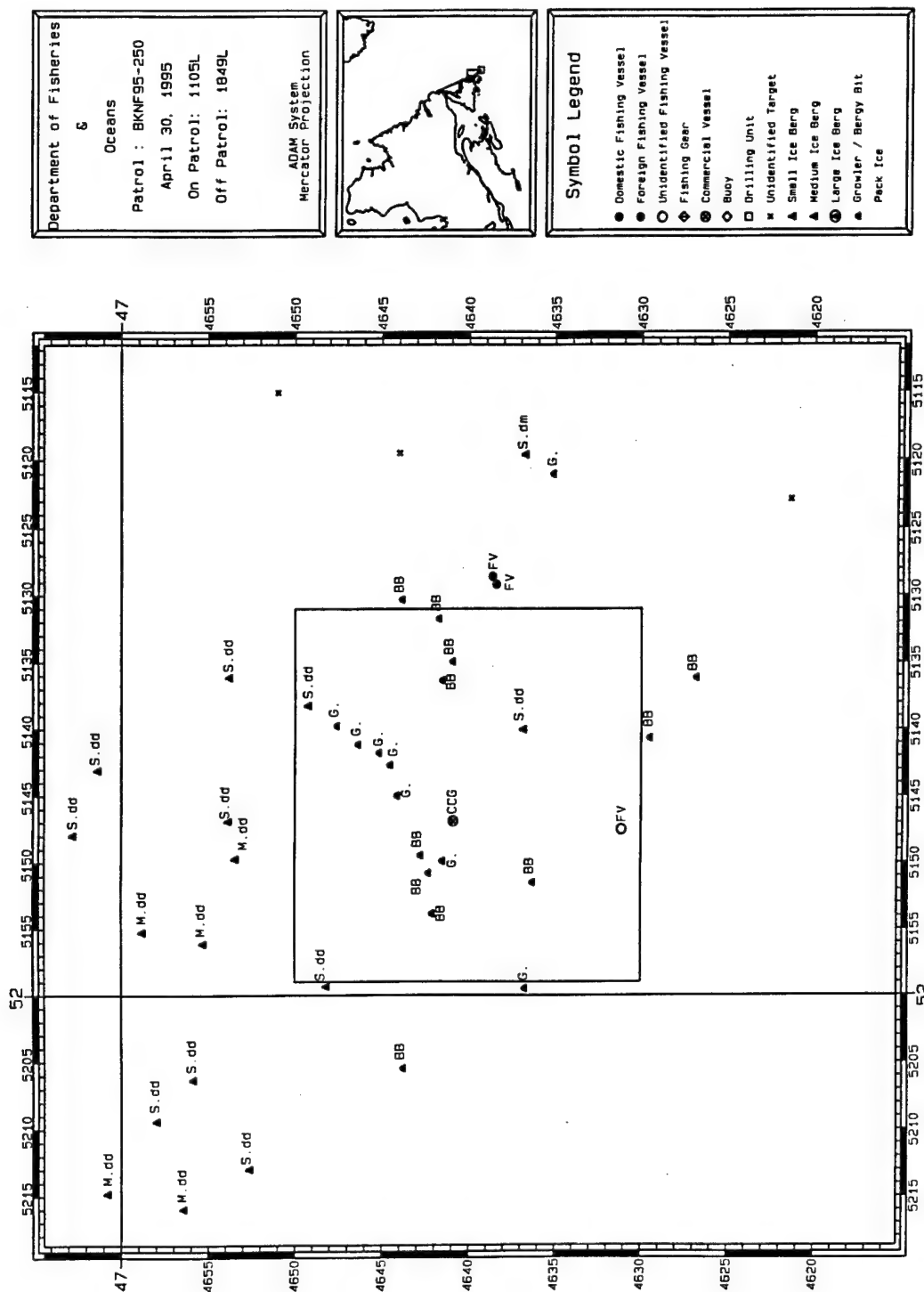
Figure 23. Ground truth at Cape Race on 30 April, 1995.

50

Table 5: HFSWR detections that are closest to the reported positions of CCGS Grenfell.

Time	Range (km)	Range (n.mi.)	Azimuth (Deg. w.r.t. Boresight)	Velocity (kn)	LATITUDE	LONGITUDE
12:45:04	102.0	55.08	0.52	0.330	46:43:37N	51:45:23W
13:00:12	102.0	55.08	0.91	0.280	46:44:00N	51:45:26W
13:15:21	102.0	55.08	1.04	0.170	46:44:07N	51:45:27W
13:39:47	102.0	55.08	1.69	0.170	46:44:45N	51:45:32W
13:54:55	102.0	55.08	1.95	0.220	46:45:00N	51:45:34W
14:10:04	100.8	54.43	2.21	0.220	46:45:10N	51:46:33W
14:34:31	100.8	54.43	2.60	0.110	46:45:33N	51:46:36W
14:49:39	100.8	54.43	2.99	0.220	46:45:55N	51:46:40W
15:04:48	100.8	54.43	3.25	0.060	46:46:09N	51:46:43W

Table 6:   Aliased track of a ship due to antenna grating lobes.

Time	RNG (km)	RNG (n.mi.)	Az.(Deg. w.r.t. Boresight)	DOP. (Hz)	Vel. (kn)	Magn (dB)	LAT.	LONG.
12:45	64.8	34.8	12.58	0.173	8.67	-62.7	46:28:53N	52:16:41W
13:00	61.2	32.9	13.11	0.172	8.61	-62.6	46:29:46N	52:19:15W
13:15	56.4	30.3	13.78	0.174	8.72	-60.6	46:30:52N	52:22:43W
13:39	50.4	27.1	15.13	0.178	8.94	-56.8	46:32:22N	52:27:00W
13:54	46.8	25.2	16.21	0.176	8.83	-64.9	46:33:20N	52:29:34W
14:10	43.2	23.2	-15.93	0.172	8.61	-59.8	46:34:25N	52:32:07W
14:34	37.2	20.0	-8.48	0.168	8.45	-53.8	46:37:39N	52:36:13W
14:49	33.6	18.0	-5.60	0.168	8.45	-53.5	46:38:42N	52:38:59W
15:04	30.0	16.1	-2.08	0.162	8.12	-68.1	46:39:44N	52:41:50W

It can be seen that the azimuthal angles of the two partial tracks differ by an amount that is approximately equal to the difference between the main lobe and a grating lobe. Since the other two attributes, range and velocity, are compatible with a single moving target and no other tracks of moving targets were found in the vicinity, it is concluded that a switching between the true track and an alias track has taken place at the time of 14:10:04. The questions are which part is the true track, and which part is the alias track? Without ground truth, one cannot be 100% sure. An educated guess is that the position estimates for the time interval between 12:45:04 and 13:54:55 represent the aliased track. The rationale is as follows. From Table 5, the last position of the ship is near boresight. Since the aliasing effect is minimal at boresight where the pointing directions of the element and the array coincide, this position estimate is deemed more reliable than the others. Hence it is concluded that the first 6 detections are those of an aliased track.

Another alias track was corrected with the aid of ground truth provided in Figure 23. This track was probably that of an iceberg. Table 7 lists two partial tracks which are indicated in Figure 22 as targets No.6 and 7. The 6 detections from 12:45:04 to 14:10:04 indicate a target at a range of 38 n.mi. and a bearing of about 16°. The three detections from 14:34:31 to 15:04:48 indicate a target at about the same range but at a bearing of about -16°. From Figure 23, we see that there are a number of small-to-medium icebergs in the area around (46:50N, 52:10W) but no icebergs were sighted in the area around (46:30N, 52:14W). Hence we assume that the track corresponding to the first six detections in Table 7 is an aliased track.

After correcting for the azimuthal bias and probable aliased tracks, the tracks were redrawn in Figure 24. Using the CCGS Grenfell as a reference, the positions of a number of detected targets correlate well visually with those of the ground truth. For example, in Figure 23, three fishing vessels are indicated, one at (46:31N, 51:47W) and the other two at (46:39N, 51:27W). In Figure 24, we observe two moving targets that correspond with the above-mentioned fishing vessels. The track that correlates with the target at (46:31N, 51:47W) has an average velocity of - 9.3 knots, which indicates that the vessel is sailing away from the radar. According to the report supplied by Atlantic Airways, the two fishing vessels at the position of (46:39N, 51:27W) were sailing in tandem in close proximity of one another. The radar detected only one track, and the average speed for this target was about +8 knots.

Figure 25 shows the average energy of the Bragg components as a function of range for Cape Race on 30 April, 1995. The individual plots in Figure 25 are for the various beam pointing directions. The composite Bragg energy versus range profile similar to that of Figure 21 is shown in Figure 26 together with the propagation loss versus range profile for 6 MHz at two sea states. It can be seen that the variation of the Bragg energy at ranges less than 100 km differs significantly from those of the propagation loss. There are two possible reasons for the observed difference.

The first is that the waveform used in the Cape Race radar was a pulse-compression waveform (FMICW). The individual pulses within each FM sweep had a length of 240 µsec. The eclipsing range was therefore about 36 km. Since the receiver was turned off when the pulses were being transmitted, only a fraction of the echo from range cells within the eclipsing range
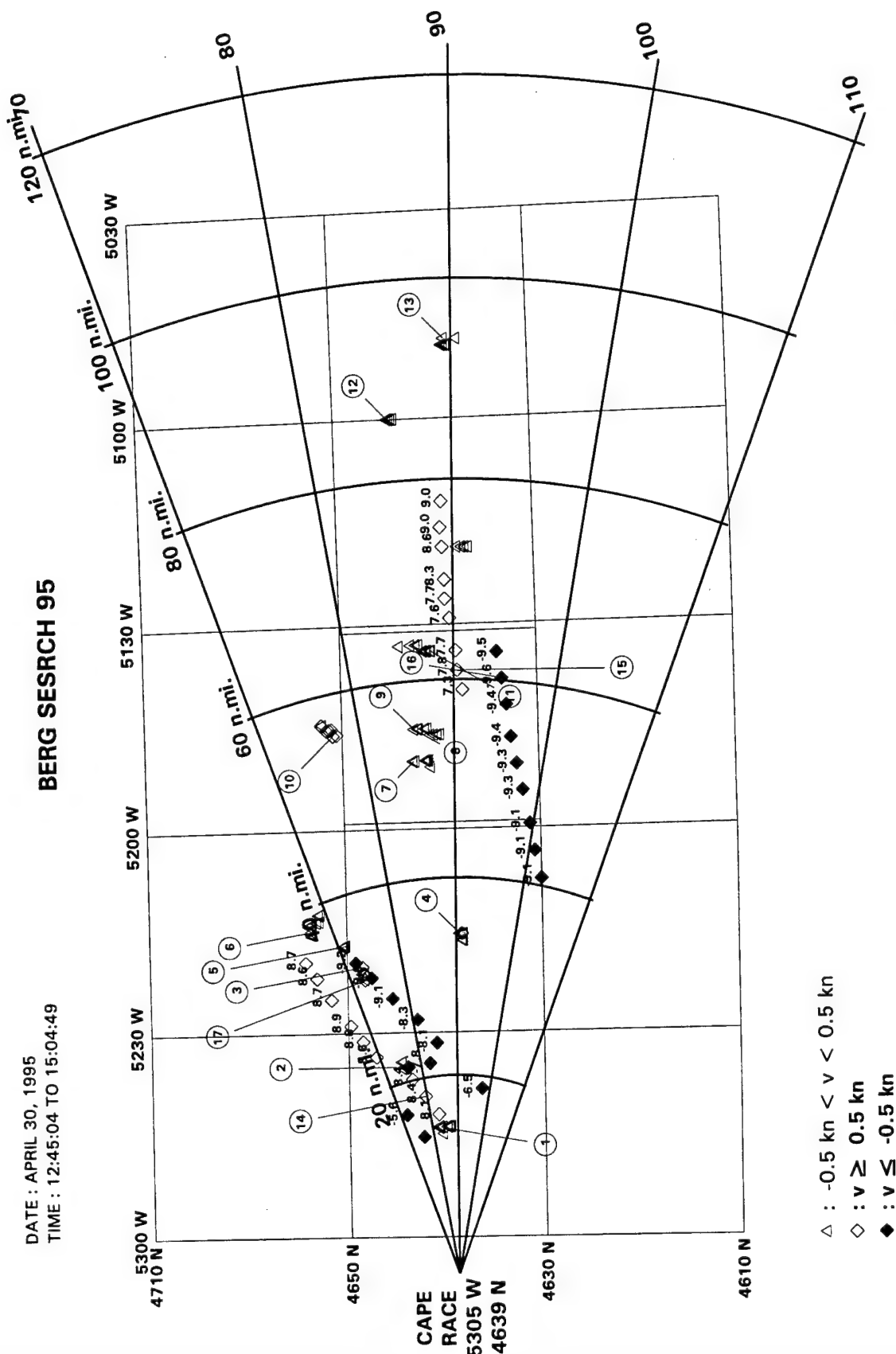
Figure 24. Calibrated track plot for Cape Race on 30 April, 1995.

53
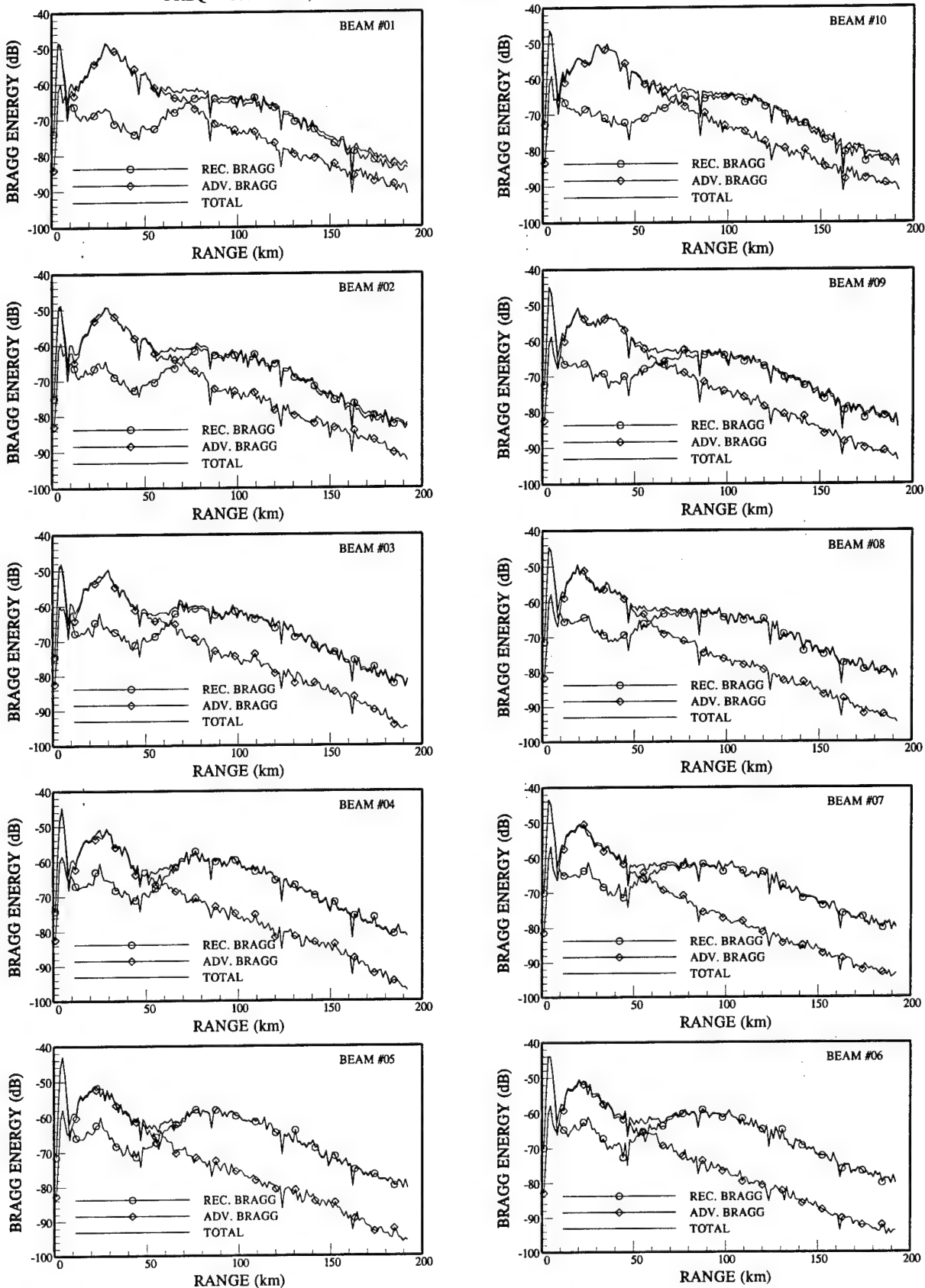
Figure 25. Average Bragg energy as a function of range for Cape Race on 30 April, 1995.
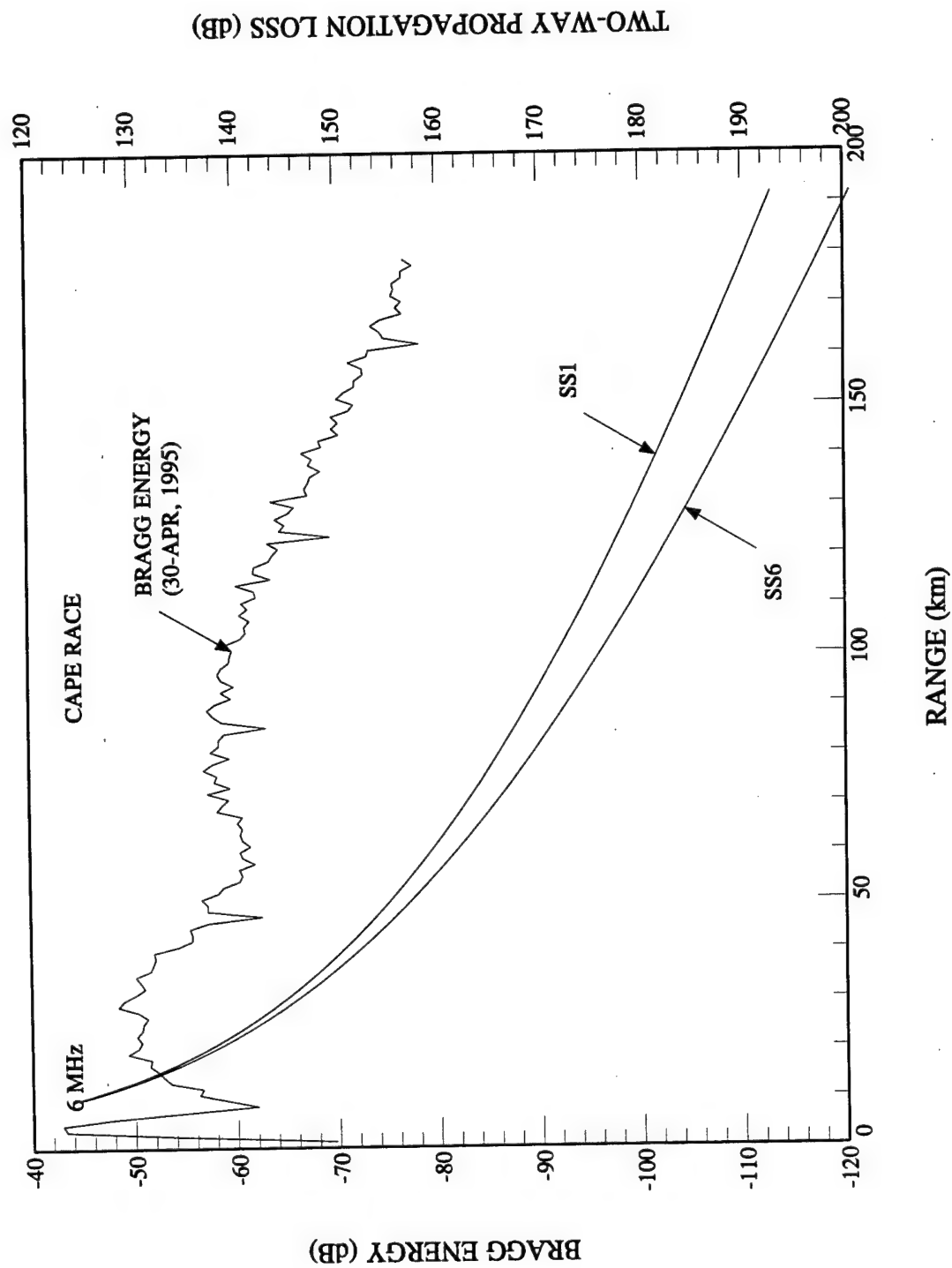
TWO-WAY PROPAGATION LOSS (dB)

Figure 26. Bragg energy at Cape Race on 30 April, 1995 and propagation loss as functions of range at 6 MHz.

55

Table 7:   Aliased track of a slow-moving target due to antenna grating lobes.

Time	Range (km)	Range (n.mi.)	Azimuth (Deg.)	Doppler. (Hz)	Velocity (kn.)	Magnitude (dB)
12:45:04	69.6	37.6	15.53	-0.008	-0.39	-78.85
13:00:12	70.8	38.2	15.39	-0.008	-0.39	-80.19
13:15:21	70.8	38.2	15.80	-0.009	-0.44	-80.71
13:39:47	70.8	38.2	16.07	-0.008	-0.39	-80.67
13:54:55	70.8	38.2	15.93	-0.008	-0.39	-78.33
14:10:04	70.8	38.2	16.75	-0.008	-0.39	-78.57
14:34:31	70.8	38.2	-16.61	-0.008	-0.39	-80.05
14:49:39	72.0	38.9	-16.34	-0.008	-0.39	-81.17
15:04:48	72.0	38.9	-16.07	-0.009	-0.44	-80.00

was available for pulse compression. The resulting reduction in pulse compression gain accounts for the peculiar variation of the Bragg energy for ranges less than 40 km.

The reasons for the observed dip in Bragg energy as a function of range between 40 km and 100 km are difficult to pin point. One plausible explanation is that, unlike Cape Bonavista, the ocean floor around Cape Race remains relatively shallow out to several tens of km, except for a small area where there is a deep channel. This could prevent the sea in these areas from reaching the fully developed state even if the prevailing wind has the required speed.

Regardless of the real reasons for the observed anomalous behaviour of the Bragg energy at close-in ranges, we cannot be certain that the sea within 90 km of Cape Race was fully developed (for an operating frequency of 5.811 MHz) on April 30, 1995. Consequently, the estimate of the RCS for targets at ranges less than 100 km are not very reliable.

We can, however, obtain an estimate of the RCS for the CCGS Grenfell because its range was at slightly greater than 100 km where the Bragg energy behaved normally. The average Doppler energy for the CCGS Grenfell was estimated to be -72 dB. From Figure 26, the energy for the Bragg components at 102 km was estimated to be approximately -60 dB. Thus the energy of the echo from the Grenfell was about 12 dB below the Bragg lines. Assuming $\sigma_B^0 = -20$ dB, a range cell size of 1.2 km and an azimuthal beamwidth of 2.54°, the equivalent RCS of the Bragg lines at 102 km is estimated to be 47.4 dBm². To account for the contribution to the Bragg components from the grating lobes of the antenna, we add 3 dB to the estimate (there is one grating lobe besides the main lobe that intersect the elemental pattern, as can be seen from Figure 6). Hence the RCS of the Bragg lines is $\sigma_B = 50.5$ dBm², and the RCS for CCGS Grenfell is 38.5 dBm² (50.5 -12, and the free space RCS is 26.3 dBm².

The details of all the probable iceberg targets detected and tracked by the Cape Race HFSWR on 30 April, 1995 are tabulated in the Table 8. These are targets with radial speed less than one knot. For these targets, the parameters were averaged over the entire observation period.

Table 8: Detected surface targets by the Cape Race HFSWR on 30 April, 1995.

Target No.	Range (km)	Range (n.mi.)	Az.(Deg w.r.t. T.N.)	Vel. (kn)	Mang. (dB)	LAT.	LONG.
1	27.6	14.8	121.35	0.36	-64.8	46:40:08N	52:43:51W
2	40.8	21.6	111.45	-0.43	-83.3	46:44:17N	52:34:52W
3	57.6	31.8	108.45	0.58	-78.3	46:48:21N	52:21:01W
4	62.4	34.1	115.13	0.44	-80.6	46:38:11N	52:15:49W
5	64.8	35.0	106.74	0.00	-78.5	46:50:15N	52:17:03W
6	72.0	38.3	103.65	-0.40	-79.8	46:53:15N	52:13:29W
7	94.8	51.8	122.29	0.14	-88.8	46:41:45N	51:50:04W
8	100.8	54.8	121.91	0.20	-75.1	46:41:17N	51:45:38W
9	102.0	55.1	121.82	0.24	-74.6	46:42:20N	51:45:16W
10	103.2	56.5	112.53	0.58	-88.0	46:51:28N	51:45:02W
11	116.4	63.1	122.69	0.37	-89.5	46:41:47N	51:33:28W
12	135.6	73.2	126.62	0.22	-93.4	46:37:06N	51:18:48W
13	159.6	86.2	121.60	0.23	-97.9	46:44:08N	50:59:58W
14	174.0	93.5	125.47	-0.24	-97.8	46:38:09N	50:49:11W

4.2   Results for 2 May, 1995.

Data were collected on 2 May, 1995 at Cape Race only. There were only three files collected on 2 May, 1995. Each file was divided into three segments. Hence there were nine detection intervals for the Cape Race data on 2 May, 1995. The starting times of the segmented data files are listed in Table A.3 of Appendix A. The data were processed as described in Section 4.1b.

The preliminary track plot between the times of 12:44:42 and 15:07:47 is presented in Figure 27. The beam pointing correction of -5.68° described in Section 4.1b was applied to the bearing estimates. The ground-truth data for Cape Race on the day of 2 May, 1995 is shown in Figure 28. The region for which ground-truth data were collected is the square area bound by the
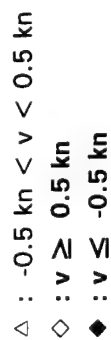
57

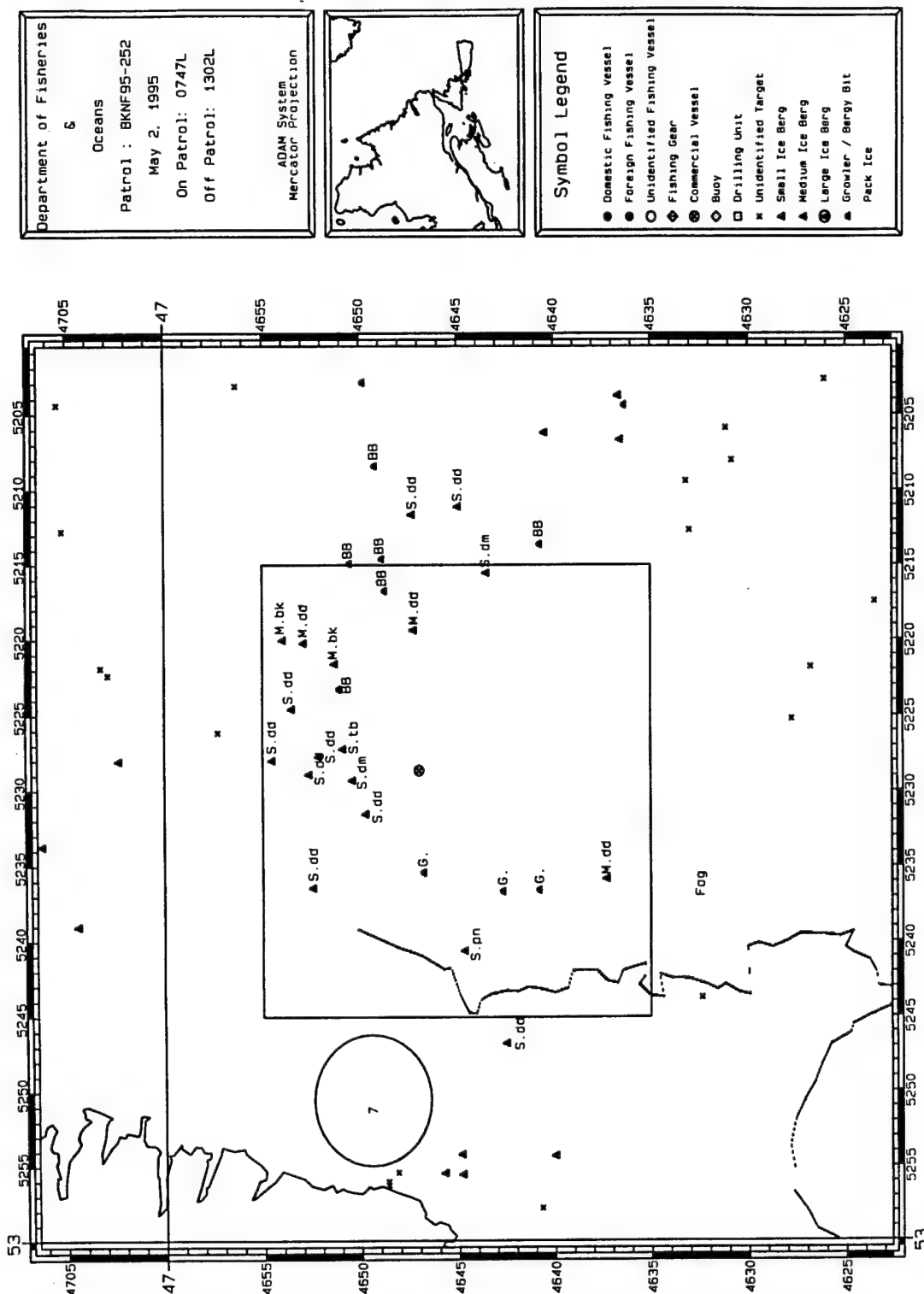Figure 27. Preliminary track plot for Cape Race on 2 May, 1995.

58

Figure 28. Ground truth at Cape Race on 2 May, 1995.

59

longitude-line pair of (52:25W, 52:45W) and latitude-line pair of (46:55N and 46:35N). This area is within 35 n.mi. of Cape Race, and the 35° surveillance sector at 35 n.mi. only covers about half of the total area inside the box.

Many more targets were detected in the Cape Race data of 2 May than in the data of 30 April, 1995. There were four visible ship tracks as shown in Figure 27. One of these was detected at a range exceeding 120 nautical miles.

Several alias tracks were corrected with the aid of the ground truth provided in Figure 28. Target No.8 in Figure 27 lies on the boundary of the square box. Its position was approximately (46:35N, 52:20W). From Figure 28, there were no icebergs sighted around this location. If we assume that this track was an alias track, a possible location for the true track would be approximately at (46:52N, 52:20W). There were a number of medium icebergs in this area as can be seen from Figure 28. Similarly targets No.11 and 12 are probable alias tracks and were corrected.

After correcting for probable aliased tracks, the accumulated track plot was redrawn in Figure 29. There is good visual agreement among many targets inside the box and those of the ground truth. No ground truth is available for areas beyond 40 n.mi. from Cape Race. Hence it could not be ascertained that there were no alias tracks among the remaining detections.

The large number of targets detected on this day are tabulated in Table B1. Only targets with radial speeds less than one knot are listed. The parameters were averaged over the entire observation period.

Figure 30 shows the average energy of the Bragg components as a function of range for Cape Race on 2 May, 1995. The individual plots in Figure 30 are for the various beam pointing directions. The composite Bragg energy versus range profile is shown in Figure 31 together with the propagation loss versus range profile for 6 MHz at several sea states. It can be seen that the attenuation of the Bragg energy is at a slightly lower rate than that of the propagation loss. This could be interpreted as an indication that the sea conditions at various ranges up to 200 km from Cape Race were similar on 2 May. However compared with the data in Figure 27, the Bragg energy is substantially lower on 2 May than on 30 April for ranges beyond 70 km. This suggests that the sea was not fully developed (for 5.81 MHz) around Cape Race on 2 May, 1995. Hence estimates of target RCS were not made using the 2 May data.

4.3   Results for 25 July 1995.

Raytheon returned to Cape Bonavista on July 25, 1995. Since some icebergs were still in the surveillance area, additional data were collected which can be used for iceberg detection. However, there are no ground-truth data for the July trial. The data were processed in the same manner as described in Section 4.1a. The starting times of the data files are listed in Table A.4 in Appendix A.

Strong ionospheric reflection of the radar signal was observed over a number of range cells, from about 95 km to about 125 km. The ionospheric reflection interference persisted from

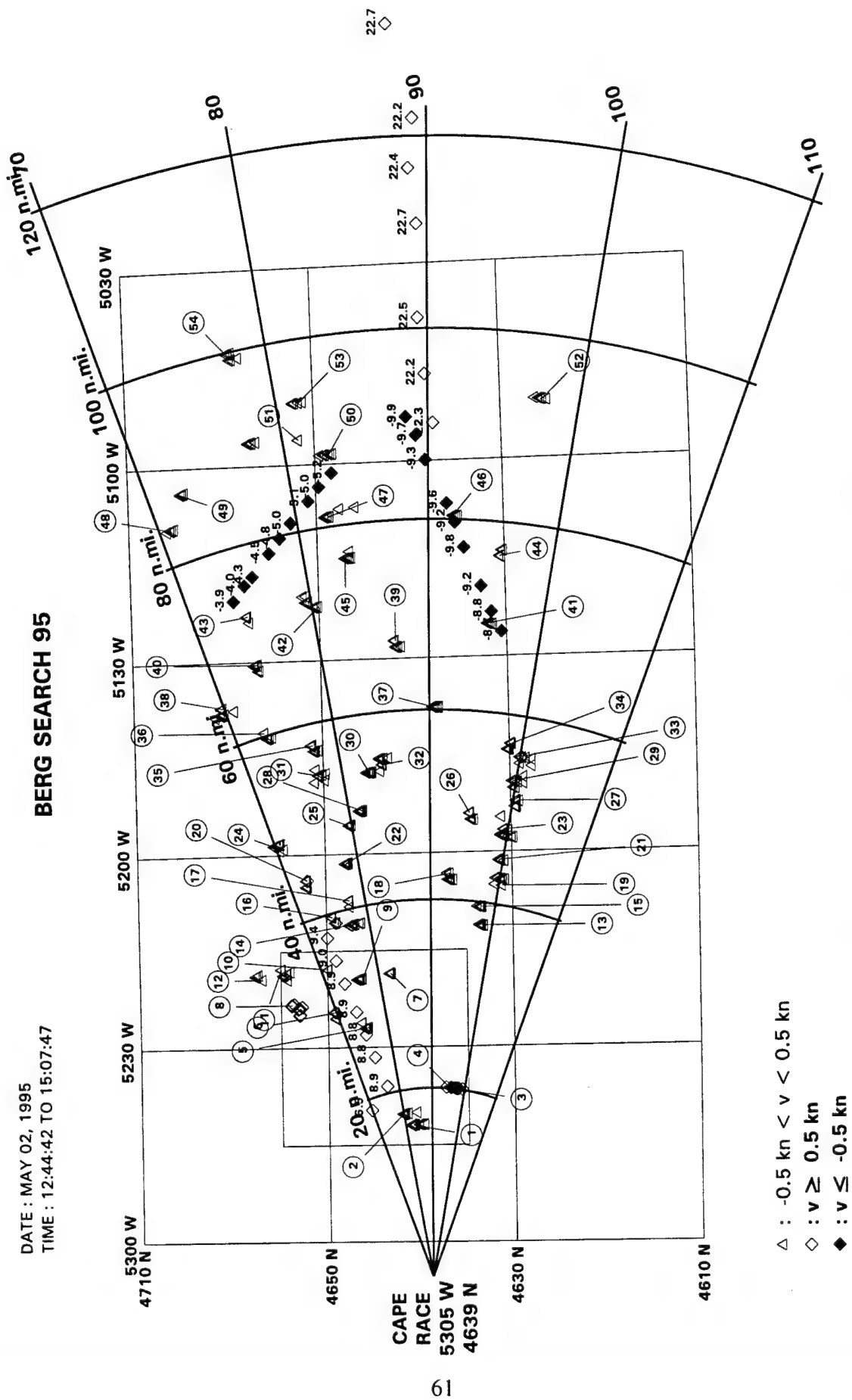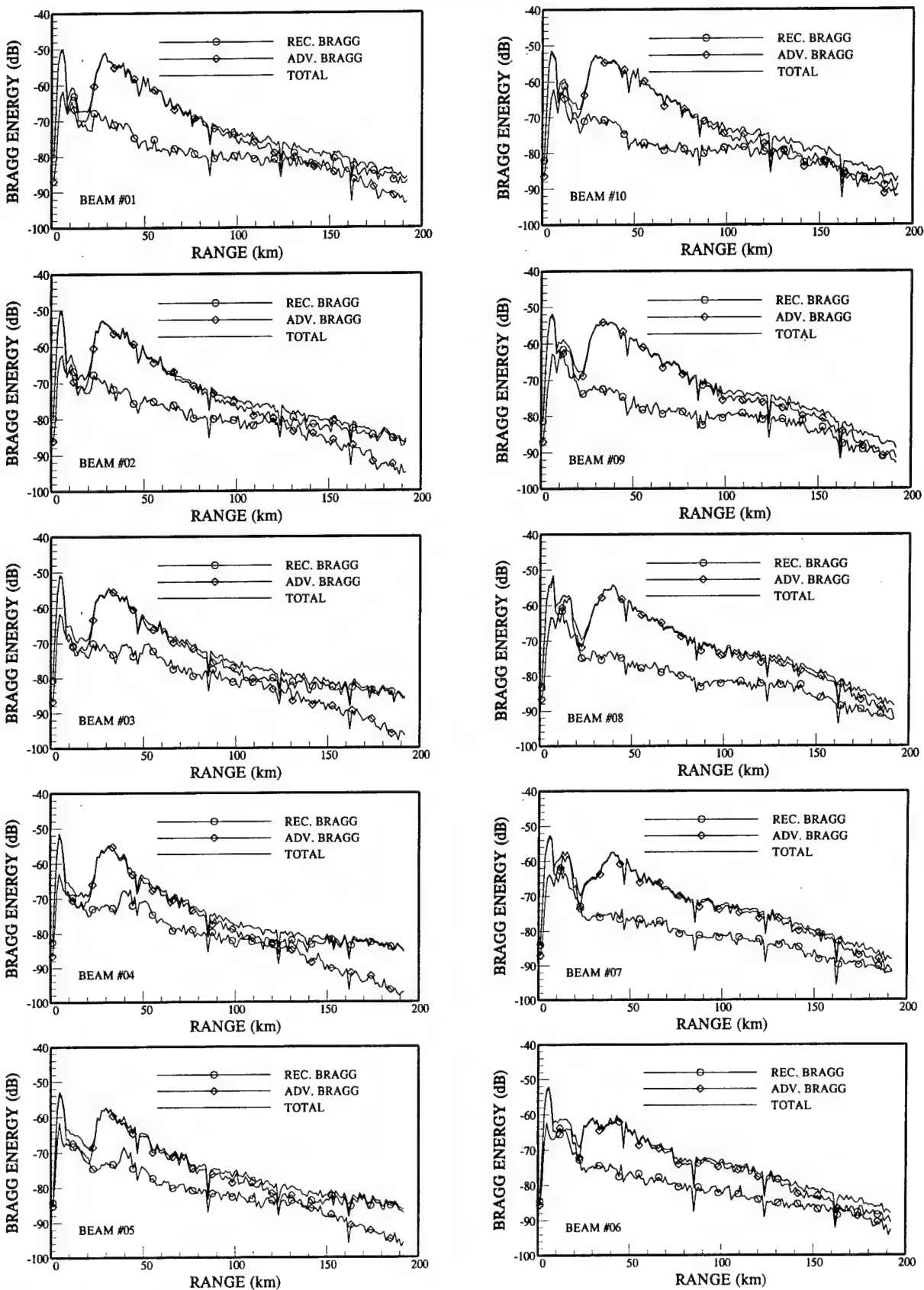Figure 29. Calibrated track plot for Cape Race on 2 May, 1995.

61

Figure 30. Average Bragg energy as a function of range for Cape Race on 2 May, 1995.
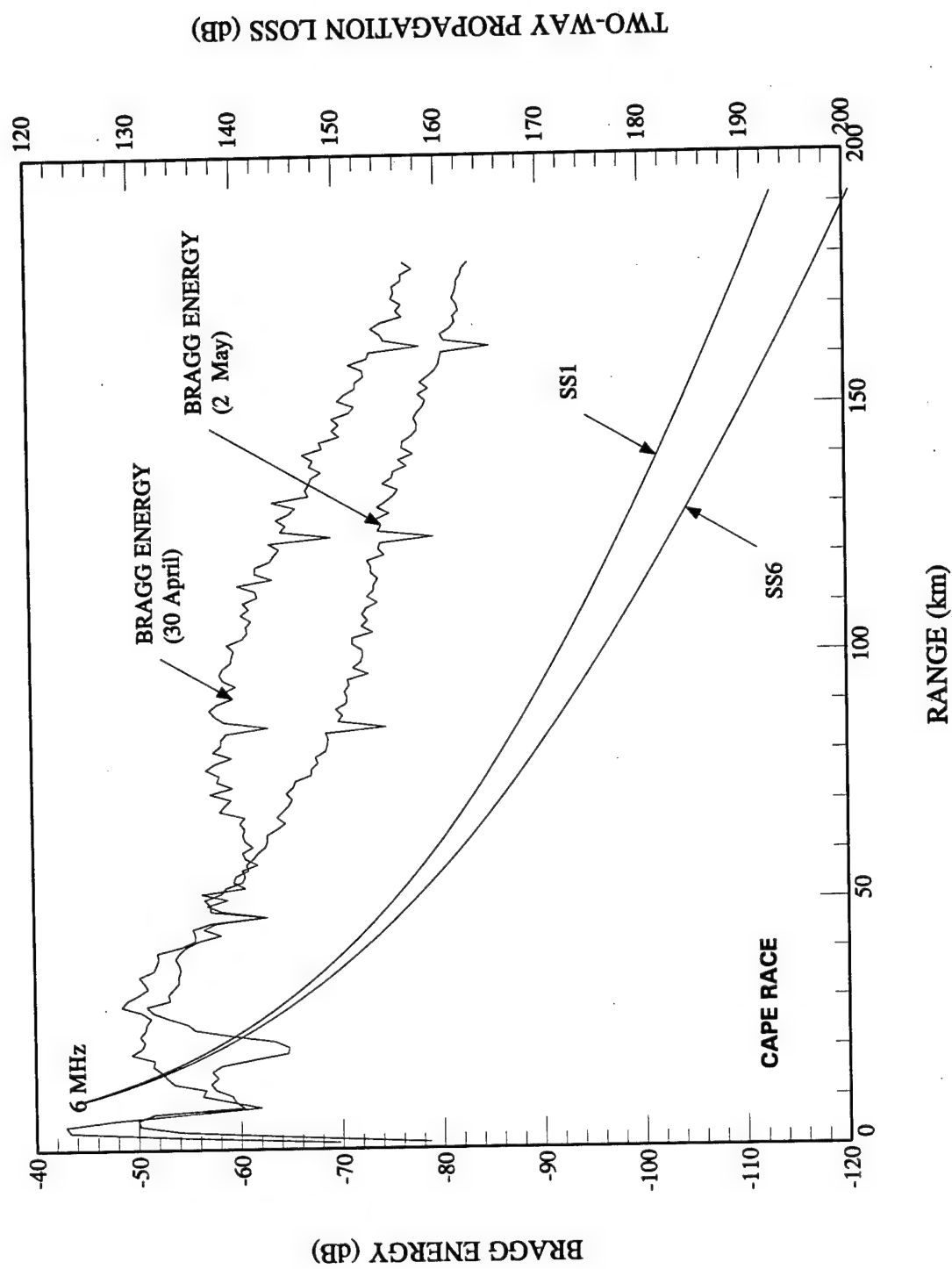
Figure 31. Bragg energy at Cape Race on 2 May, 1995 and propagation loss as functions of range at 6 MHz.

63

the time of 09:30 to about 11:30, at which time data collection was interrupted (between files ICE_T6 and ICE_T7) to down load data from disk to tape. By the time data collection resumed at 15:35, the ionospheric interference had largely disappeared. Because of their low velocity, there was no track loss for icebergs. However, there were discontinuities in ship tracks because of this gap in the data. Three possible icebergs were detected.

The accumulated HFSWR track plot for Cape Bonavista on 25 July, 1995 between the times of 12:04:50 and 18:25:13 is presented in Figure 32. There were three low-velocity targets. It These are listed in Table 9.

Table 9:   Probable icebergs detected at Cape Bonavista on 25 July, 1995.

Target No.	Range (km)	Range (n.mi.)	Az.(Deg. w.r.t. True North)	Vel. (kn)	Magn. (dB)	LAT.	LONG.
1	48.0	26.1	167.53	0.01	12.3	48:15:43N	52:56:55W
2	78.0	42.2	121.06	-0.08	12.1	48:19:16N	52:11:04W
3	112.8	60.9	62.23	0.21	7.9	49:09:08N	51:42:59W

Figure 33 shows the average power of the Bragg components as a function of range for Cape Bonavista on 25 May, 1995. The individual plots in Figure 33 are for the various beam pointing directions. The composite Bragg energy versus range profile similar to that of Figure 21 is shown in Figure 34, together with the propagation loss curves for 4 MHz at several sea states. It can be seen that the attenuation of the Bragg energy with range is at a much lower rate compared to that for the propagation loss. Also the average Bragg energy is substantially lower on the day of 25 July. Further examination of the data reveals that the Bragg energy calculated from data taken in the morning of 25 July, 1995 (files ICE_T1 to ICE_T6 in Table A.4 of Appendix A) has a level comparable to those obtained on 30 April, 1995 at Cape Bonavista.

Figure 32. Accumulated track plot for Cape Bonavista on 25 July, 1995.

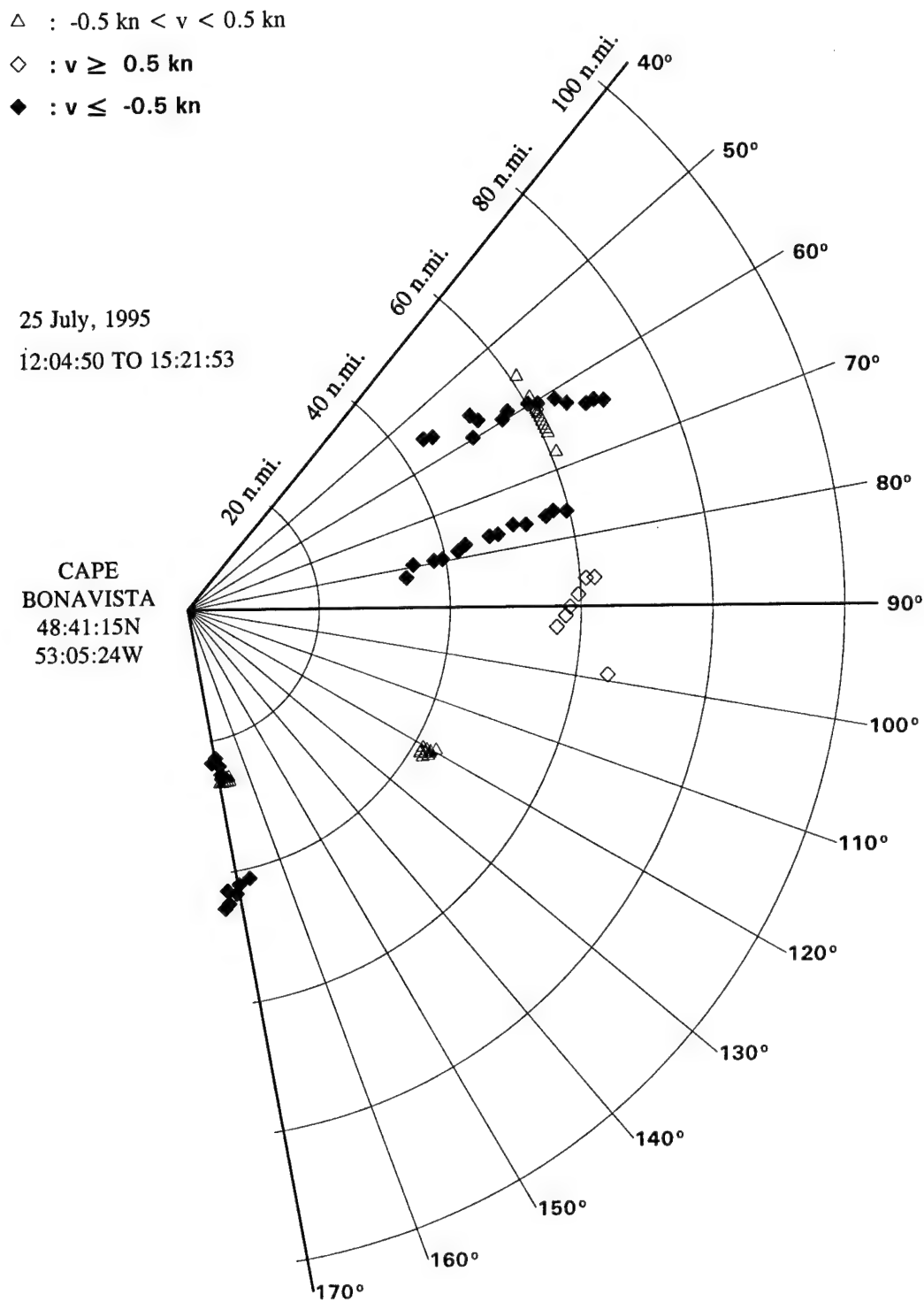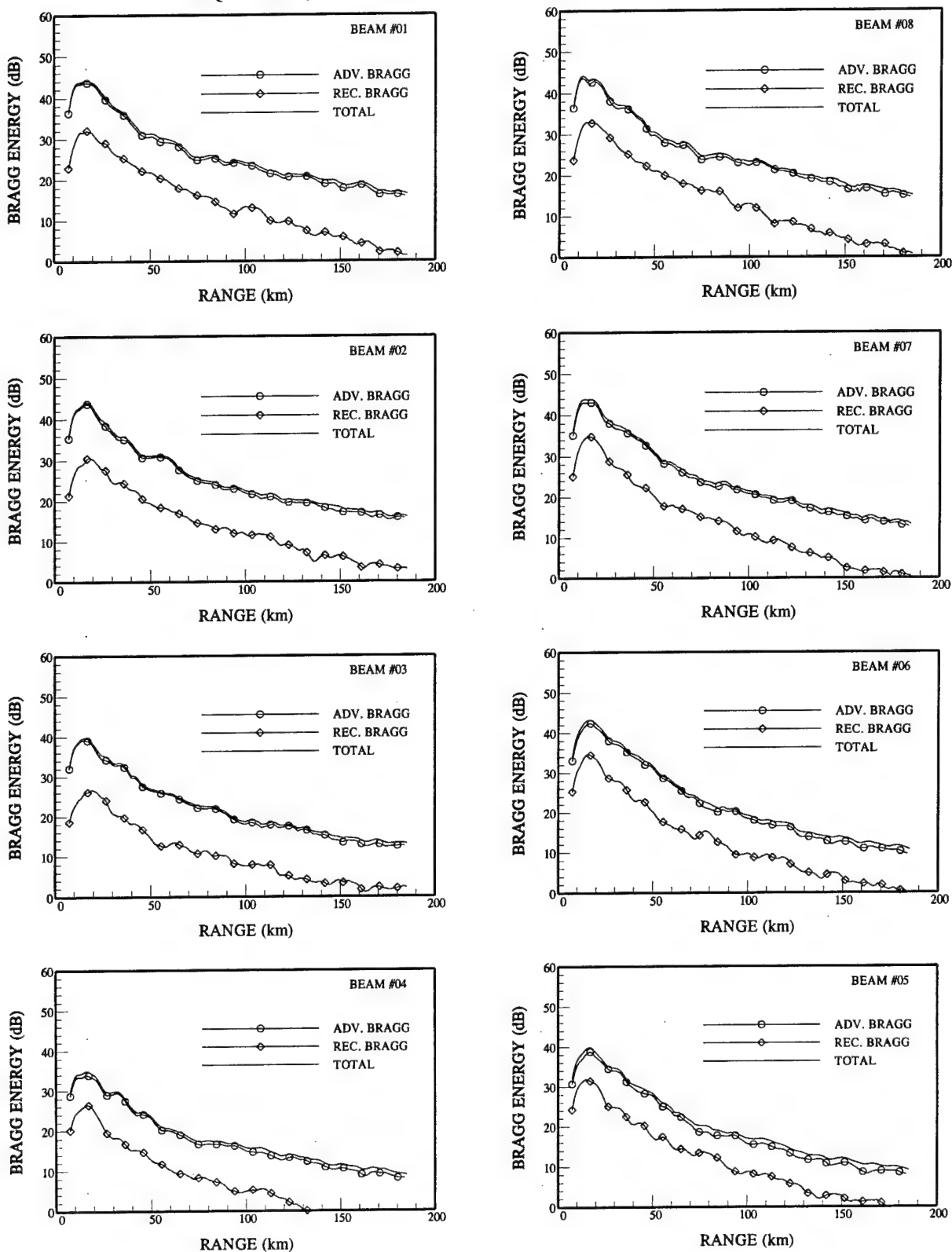Figure 33. Average Bragg energy as a function of range for Cape Bonavista on 25 July, 1995.
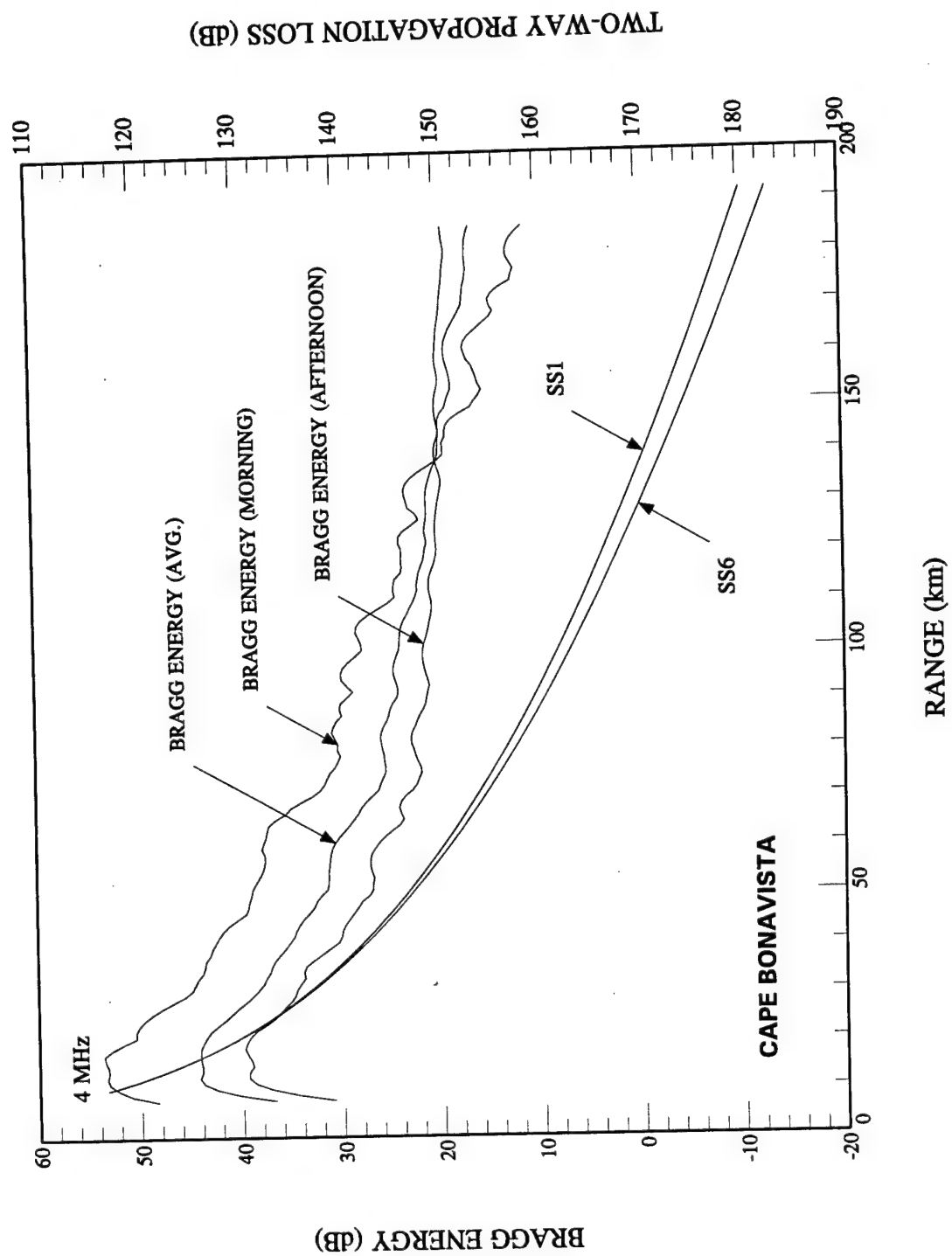
Figure 34. Bragg energy at Cape Bonavista on 25 July, 1995 and propagation loss as functions of range at 4 MHz.

67

5.   CONCLUSIONS.

Using two experimental HFSWR facilities in Newfoundland, we have demonstrated the potential of employing HFSWR technology for the detection and tracking of icebergs and surface vessels. Even though the nominal resolutions of the HFSWR in bearing and range are rather coarse, using advanced digital signal processing techniques, quite respectable accuracies can be obtained in both range and azimuth. For the Cape Bonavista facility, with an average power of only five Watts, icebergs can be detected out to 80 nautical miles.

Results obtained from Cape Bonavista on 30 April and 25 July, 1995 were similar. To the extent that ground-truth data were available, good visual correlation was obtained between the radar detected targets and the ground truth. Only icebergs of medium size or larger were detected at Cape Bonavista. This is attributed to the low average power of the Cape Bonavista HFSWR. In addition, the relatively coarse range and azimuthal resolution of this radar also played a part in the small number of detections, in that closely spaced targets could not be resolved.

For the Cape Race facility, which has a substantially higher average power and much finer range and azimuthal resolutions, surface targets (most likely icebergs) could be detected out to beyond 100 n.mi. The CCGS Sir Wilfred Grenfell was detected and tracked throughout the observation period. Its estimated position and those of several icebergs correlated very well with the ground-truth data.

The data analyzed in this report were collected during day-light hours. It is well known that the noise level increases significantly after dusk in the lower end of the HF band. In addition, there is also a substantial increase in co-channel radio-interference level. Consequently, the detection and tracking performance of the HFSWR at night time would be degraded. The problem of increased noise level can be overcome by increased transmit power, higher antenna gain and longer coherent integration time. The problem of increased co-channel interference can be alleviated by cancellation techniques [28] employing cross-polarized auxiliary antennas and by locating and operating in a channel that is free of interference. A good frequency management system is essential.

There are some definite advantages in employing the HFSWR over other sensors in iceberg detection and tracking. Firstly, it has the capability to provide a real-time continuous surveillance picture of a wide area of the coastal regions at relatively low cost. Secondly, it detects the relatively large icebergs among much smaller ones or packed sea ice. This cannot easily be done by examining satellite images. Finally, it provides some target identification capability based on relative radar-cross-section and velocity estimates.

It should be emphasized that these trial results were obtained with experimental HFSWRs, and they by no means represent the full potential of an operational HFSWR. DND, in collaboration with Canadian Industry, is in the process of developing two full-scale HFSWRs. These radars are scheduled to become operational in June 1997. At that time a comprehensive evaluation of the capabilities of the HFSWR will be carried out.

6. REFERENCES.

[1] Desjardins, L and H. McRuer, Ed., "Berg Search '95 - Evaluation of ERS-1 and ground wave over-the-horizon radar target detection and identification," Canadian Ice Service Report, 18 April, 1996.

[2] Chan, H.C., "Evaluation of the FMICW waveform in HF surface wave radar applications," DREO Report No.1219, Defence Research Establishment Ottawa, January 1994.

[3] Skolnik, M.L., Ed.,"Radar Handbook - Array Antennas," McGraw-Hill Book Company, New York, 1970, p.11-10.

[4] Harris, H.J., "On the use of windows for harmonic analysis with the discrete Fourier transform", Proceedings of the IEEE, Vol.66, No.1, January 1978. pp.51-83.

[5] Lipa, B.J. and D.E. Barrick, "Analysis Methods for Narrow-beam High Frequency Radar Sea Ehco," NOAA Tech. Report ERL 420-WPL 56, 1982.

[6] Barton, D.K., "Radar system analysis," Artech House Inc., Dedham, MA., 1976, pp.57-58.

[7] Burg, J.P., "Maximum entropy analysis," Ph.D. Desertation, Standford University, 1975.

[8] Schmidt, R.O., "Multiple emitter location and signal parameter estimation," Proc. RADC Spectrum Estimation Workshop, Rome, New York, 1979, pp.243-258.

[9] Hanson, R.C., "Microwave scanning antennas, Vol. 1: Apertures," Academic Press, New York and London, 1964.

[10] Nitzberg, R., "Clutter map CFAR Analysis," IEEE Trans., Vol. AES-22, July 1986, pp.419-421.

[11] Weiss, M., "Analysis of some modified cell-averaging CFAR processors in multiple-target situation," IEEE Trans. Vol. AES-18, January 1982, pp.102-114.

[12] Dillard, G.M. and C.E. Antoniak, "A practical distribution-free detection procedure for multiple range bin radars," IEEE Trans., vol. AES-6, September 1970, pp. 629-635.

[13] Hansen, V.G., "Detection performance of some nonparametric rank tests and an application to radar," IEEE Trans., vol. IT-16, No.3, May, 1970, pp. 309-318.

[14] Antoniak, C.E. et al., "Distribution-free detection in radar with multiple resolution elements," SWIEEECO Record, IEEE Cat. No. F-72, 1967, pp. 17-2-1 to 17-2-8.

[15]   Barrick, D.E., "The statistics of HF sea-echo Doppler spectra", IEEE Trans. on antenna and propagation, vol.AP-25, No.1, January 1977, pp. 19-28.

[16]   Shearman, E.D.R., "Radio science and oceanography," Radio Science, Vol.18, No.3, May-June, 1983, pp.299-230.

[17]   Cantrell, B.H., "Adaptive tracking algorithm for tracking air targets with search radars," NRL report 7805, Naval Research Laboratory, Washington, D.C., September 1974.

[18]   Singer, R.A., R.G. Sea and K.B. Housewright, "Derivation and evaluation of improved tracking filters for use in dense multitarget environments," IEEE Trans. on IT, Vol. IT-20, No.4, July 1974, pp.423-432.

[19]   Headrick, J., "HF over-the-horizon radar" (Ch. 24, *Radar Handbook*, M.L. Skolnik, Ed.)," McGraw-Hill Book Company, New York, 1990, p. 24.3.

[20]   Shearman, E.D.R., "Propagation and scattering in MF/HF ground wave radar," IEE Proceedings, Vol. 130, Part F, No.7, December 1983, pp.579-590.

[21]   Barrick D.E., "Theory of HF and VHF propagation across a rough sea," Radio Science Vol. 6, No.5, May 1971, pp.517-533.

[22]   Teague, C.C. and G.L. Tyler, "The radar cross section of the sea at 1.95 MHz: Comparison of in-situ and radar determinations," Radio Science, Vol. 10, No.10, October, 1975, pp.847-852.

[23]   Barrick, D.E., "Remote sensing of sea state by radar" (Ch. 12 in *Remote sensing of the troposphere*, V.E. Derr, Ed.), NOAA/ Environmental Research Laboratories, Boulder, Colo., 1972, pp.12-1 to 12-46.(12-12)

[24]   Kinsman, B., "Wind Waves," Prentice-Hall Inc., Englewood Cliffs, N.J., 1965.

[25]   Barrick, D.E., "Electromagnetics of the sea,", AGARD Conference Proceedings, No. 77, 1970, PP.18-1 to 18-25.

[26]   Teague, C.C., G.L. Tyler and R.H. Stewart, "Studies of the sea using HF Radio scatter," IEEE Trans. on Antenna and Prop., Vol. AP-25, No.1, January, 1977, pp. 12-19.

[27]   Barrick, D.E., "Theory of ground-wave propagation across a rough sea at decameter wavelengths, Contract No. DAA H01-70-C-0312, Battell Memorial Institute, Columbus Laboratories, January, 1970.

[28]   Madden, J., "The adaptive suppression of interference in HF ground wave radar," RADAR 87, IEE International Radar Conference, London, U.K, October 1987, pp.98-102.

7. ACKNOWLEDGEMENT.

8.   APPENDICES.

8.1   Appendix A: Experimental data log.

Table A.1:   Starting time of segmented data files collected at Cape Bonavista on April 30, 1995.

File No.	Seg	Time	File	Seg	Time	File	Seg	Time
ICE-16	A	12:04:50	ICE-20	A	13:57:46	ICE-24	A	16:23:10
ICE-16	B	12:14:23	ICE-20	B	13:48:13	ICE-24	B	16:32:43
ICE-17	A	12:25:18	ICE-21	A	14:29:44	ICE-25	A	17:02:03
ICE-17	B	12:34:51	ICE-21	B	14:39:17	ICE-25	B	17:11:36
ICE-18	A	12:45:34	ICE-22	A	15:21:53	ICE-26	A	17:33:02
ICE-18	B	12:55:07	ICE-22	B	15:31:26	ICE-26	B	17:42:35
ICE-19	A	13:06:18	ICE-23	A	15:44:13	ICE-27	A	18:15:40
ICE-19	B	13:15:51	ICE-23	B	15:53:46	ICE-27	B	18:25:13

Table A.2:   Starting time of Cape Race data collected on April 30, 1995.

File No.	Segment	Time	Segment	Time	Segment	Time
One	1	12:45:04	2	13:00:12	3	13:16:21
Two	1	13:39:47	2	13:54:55	3	14:10:04
Three	1	14:34:31	2	14:49:39	3	15:04:48

Table A.3:   Starting times of the segmented data files for Cape Race on 2 May, 1995.

File No.	Seg. No.	Time	File No.	Seg. No.	Time	File No.	Seg. No.	Time
ONE	1	12:44:42	TWO	1	14:11:10	THREE	1	15:07:47
ONE	2	12:59:50	TWO	2	14:26:18	THREE	2	15:22:55
ONE	3	13:14:59	TWO	3	14:41:27	THREE	3	15:38:04

Table A.4:   Starting time of data files collected at Cape Bonavista on 25 July, 1995.

File No.	Seg	Time	File No.	Seg.	Time	File No.	Seg	Time
ICE_T1	A	09:36:02	ICE_T6	B	11:18:05	ICE_T11	A	17:26:36
ICE_T2	A	09:45:11	ICE_T7	A	15:35:45	ICE_T11	B	17:36:09
ICE_T3	A	09:59:39	ICE_T8	A	15:51:49	ICE_T12	A	17:53:07
ICE_T4	A	10:14:03	ICE_T8	B	16:01:22	ICE_T12	B	18:02:40
ICE_T4	B	10:23:36	ICE_T9	A	16:21:30	ICE_T13	A	18:22:40
ICE_T5	A	10:40:34	ICE_T9	B	16:31:03	ICE_T13	B	18:32:13
ICE_T5	B	10:50:07	ICE_T10	A	16:51:48			
ICE_T6	A	11:08:32	ICE_T10	B	17:01:21			

Appendix B: Table of detections for Cape Race on 2 May, 1995.

Table B.1: Table of detections for Cape Race on 2 May, 1995.

Target No.	Range (km)	Range (n.mi.)	Az.* (Deg.)	Vel. (kn)	Magn. (dB)	LAT.	LONG.
1	30.0	16.2	85.48	-0.10	-55.7	46:40:17N	52:41:52W
2	32.4	17.5	81.24	-0.17	-67.6	46:41:40N	52:40:12W
3	37.2	20.1	97.37	0.52	-80.0	46:36:25N	52:36:24W
4	37.2	20.1	96.37	0.01	-53.5	46:36:46N	52:36:20W
5	51.6	27.4	75.30	-0.33	-53.0	46:45:53N	52:26:47W
6	54.0	29.5	69.75	0.40	-77.5	46:49:10N	52:24:57W
7	60.0	32.4	82.40	-0.03	-73.7	46:43:11N	52:18:34W
8	57.6	31.8	63.18	0.53	-84.4	46:53:16N	52:23:59W
9	60.0	32.4	76.56	0.19	-63.8	46:46:26N	52:19:25W
10	63.6	34.3	71.31	0.00	-67.2	46:49:54N	52:17:53W
11	64.8	35.7	64.06	0.35	-88.5	46:54:32N	52:18:26W
12	68.4	36.8	59.91	-0.27	-88.7	46:57:21N	52:18:48W
13	69.6	37.6	98.35	0.06	-82.0	46:33:24N	52:11:19W
14	70.8	38.2	77.79	0.16	-86.2	46:46:57N	52:10:51W
15	73.2	39.5	97.83	-0.14	-86.3	46:33:27N	52:08:27W
16	72.0	39.1	74.77	0.34	-77.6	46:49:07N	52:10:18W
17	74.4	40.7	77.66	0.17	-70.3	46:47:32N	52:07:23W
18	78.0	42.3	92.91	0.13	-82.2	46:36:40N	52:03:57W
19	79.2	42.6	100.18	-0.16	-87.3	46:31:17N	52:04:25W
20	80.4	43.6	72.44	0.36	-86.9	46:51:58N	52:04:35W
21	82.8	44.7	99.83	0.22	-77.2	46:31:09N	52:01:22W
22	82.8	44.7	78.48	-0.04	-84.1	46:47:43N	52:01:26W

* Azimuth measured closewise from true north.

Table B.1 (Continue): Table of detections for Cape Race on 2 May, 1995.

Target No.	Range (km)	Range (n.mi.)	Az.* (Deg.)	Vel. (kn)	Magn. (dB)	LAT.	LONG.
23	87.6	47.4	99.95	0.30	-88.3	46:30:33N	51:57:29W
24	88.8	48.4	73.81	0.30	-87.5	46:52:14N	51:57:28W
25	90.0	48.6	79.94	0.14	-83.3	46:47:13N	51:55:32W
26	90.0	48.8	95.78	0.24	-83.4	46:33:48N	51:54:45W
27	93.6	50.8	100.57	0.29	-87.6	46:29:23N	51:52:48W
28	92.4	49.9	81.55	-0.01	-95.7	46:46:03N	51:53:22W
29	97.2	53.0	100.21	0.37	-85.5	46:29:17N	51:49:38W
30	99.6	53.8	83.28	0.21	-80.2	46:44:57N	51:47:28W
31	99.6	54.4	77.74	0.31	-86.1	46:50:12N	51:47:46W
32	102.0	54.8	84.77	-0.11	-97.1	46:43:38N	51:45:49W
33	102.0	55.5	100.58	0.32	-92.3	46:28:27N	51:46:09W
34	104.4	56.5	98.75	0.30	-93.0	46:30:01N	51:44:14W
35	105.6	57.3	77.60	0.19	-90.3	46:50:55N	51:43:35W
36	110.4	59.8	73.23	0.29	-86.6	46:55:51N	51:41:33W
37	111.6	60.3	90.67	0.04	-84.6	46:37:50N	51:37:39W
38	117.6	63.6	69.82	0.23	-85.5	47:00:30N	51:37:50W
39	123.6	66.9	87.15	0.09	-90.5	46:41:45N	51:28:00W
40	123.6	67.2	74.17	0.34	-100.1	46:56:48N	51:30:40W
41	128.4	69.3	95.50	-0.05	-90.3	46:31:44N	51:25:04W
42	134.4	72.4	80.01	-0.02	-92.1	46:50:54N	51:21:07W
43	133.2	72.4	74.59	0.21	-84.1	46:57:36N	51:23:14W
44	142.8	76.9	95.91	-0.23	-85.3	46:30:19N	51:14:15W
45	141.6	76.5	83.60	0.18	-95.4	46:46:46N	51:14:21W

* Azimuth measured clockwise from true north.

Table B.1 (Continue): Table of detections for Cape Race on 2 May, 1995.

Target No.	Range (km)	Range (n.mi.)	Az.* (Deg.)	Vel. (kn)	Magn. (dB)	LAT.	LONG.
46	148.8	80.3	92.17	-0.19	-92.2	46:35:06N	51:08:34W
47	151.2	81.2	82.86	0.06	-88.7	46:48:13N	51:07:41W
48	154.8	83.6	70.93	0.21	-90.3	47:05:28N	51:09:25W
49	160.8	86.8	72.38	0.21	-94.6	47:04:21N	51:03:56W
50	162.0	87.5	83.01	0.03	-100.1	46:48:37N	50:58:33W
51	166.8	90.0	78.38	0.13	-93.0	46:56:04N	50:56:19W
52	172.8	93.3	97.47	-0.20	-105.3	46:25:42N	50:51:08W
53	172.8	93.3	81.59	0.07	-94.7	46:51:28N	50:50:25W
54	183.6	99.5	77.85	0.24	-97.5	46:58:38N	50:42:51W

* Azimuth measured clockwise from true north.

DOCUMENT CONTROL DATA
(Security classification of title, body of abstract and indexing annotation must be entered when the overall document is classified)

1. ORIGINATOR (the name and address of the organization preparing the document. Organizations for whom the document was prepared, e.g. Establishment sponsoring a contractor's report, or tasking agency, are entered in section 8.) DEFENCE RESEARCH ESTABLISHMENT OTTAWA	2. SECURITY CLASSIFICATION (overall security classification of the document including special warning terms if applicable) UNCLASSIFIED

3. TITLE (the complete document title as indicated on the title page. Its classification should be indicated by the appropriate abbreviation (S,C or U) in parentheses after the title.)

ICEBERG DETECTION AND TRACKING USING HIGH FREQUENCY SURFACE WAVE RADAR (U)

4. AUTHORS (Last name, first name, middle initial)

CHAN, HING C.

5. DATE OF PUBLICATION (month and year of publication of document) JANUARY 1997	6a. NO. OF PAGES (total containing information. Include Annexes, Appendices, etc.) 76	6b. NO. OF REFS (total cited in document) 28

7. DESCRIPTIVE NOTES (the category of the document, e.g. technical report, technical note or memorandum. If appropriate, enter the type of report, e.g. interim, progress, summary, annual, or final. Give the inclusive dates when a specific reporting period is covered.)

DREO TECHNICAL REPORT

8. SPONSORING ACTIVITY (the name of the department project office or laboratory sponsoring the research and development. Include the address.)
Defence Research Establishment Ottawa
3701 Carling Avenue
Ottawa, Ontario, K1A 0Z4

9a. PROJECT OR GRANT NO. (if appropriate, the applicable research and development project or grant number under which the document was written. Please specify whether project or grant) 05AB11	9b. CONTRACT NO. (if appropriate, the applicable number under which the document was written)
10a. ORIGINATOR'S DOCUMENT NUMBER (the official document number by which the document is identified by the originating activity. This number must be unique to this document.) DREO REPORT 1310	10b. OTHER DOCUMENT NOS. (Any other numbers which may be assigned this document either by the originator or by the sponsor.)

11. DOCUMENT AVAILABILITY (any limitations on further dissemination of the document, other than those imposed by security classification)

(X) Unlimited distribution
( ) Distribution limited to defence departments and defence contractors; further distribution only as approved
( ) Distribution limited to defence departments and Canadian defence contractors; further distribution only as approved
( ) Distribution limited to government departments and agencies; further distribution only as approved
( ) Distribution limited to defence departments; further distribution only as approved
( ) Other (please specify):

12. DOCUMENT ANNOUNCEMENT (any limitation to the bibliographic announcement of this document. This will normally correspond to the Document Availability (11). However, where further distribution (beyond the audience specified in 11) is possible, a wider announcement audience may be selected.)

UNLIMITED

UNCLASSIFIED

SECURITY CLASSIFICATION OF FORM
(highest classification of Title, Abstract, Keywords)

13. ABSTRACT (a brief and factual summary of the document. It may also appear elsewhere in the body of the document itself. It is highly desirable that the abstract of classified documents be unclassified. Each paragraph of the abstract shall begin with an indication of the security classification of the information in the paragraph (unless the document itself is unclassified) represented as (S), (C), or (U). It is not necessary to include here abstracts in both official languages unless the text is bilingual.)

An iceberg surveillance experiment involving multiple sensors was carried out in a one-week period between April and May 1995. Several Canadian and U.S. Government agencies and members of industry participated. The Canadian Department of National Defence (DND), in collaboration with industry, provided high-frequency surface-wave radar (HFSWR) sensors, while the Canadian and U.S. Coast Guards provided surface and aerial ground-truth data. The experiment coincided with the over-flight of the surveillance area by the ERS-1 satellite. The ERS-1 data permit the evaluation of techniques for detecting icebergs from satellite imagery. The trial results demonstrated the potential of HFSWR technology in the detection and tracking of icebergs and surface vessels. Surface targets can be detected out to beyond 100 nautical miles. The estimated positions of the targets correlate very well with the available ground-truth data.

14. KEYWORDS, DESCRIPTORS or IDENTIFIERS (technically meaningful terms or short phrases that characterize a document and could be helpful in cataloguing the document. They should be selected so that no security classification is required. Identifiers, such as equipment model designation, trade name, military project code name, geographic location may also be included. If possible keywords should be selected from a published thesaurs, e.g. Thesaurus of Engineering and Scientific Terms (TEST) and that thesaurus-identified. If it is not possible to select indexing terms which are unclassified, the classification of each should be indicated as with the title.)

RADAR
HIGH FREQUENCY
HF
ICEBERGS
TRACKING
DETECTION
SURFACE WAVE
OVER-THE-HORIZON
OTH RADARS
SURVEILLANCE
SATELLITE
AERIAL
IMAGERY

UNCLASSIFIED

SECURITY CLASSIFICATION OF FORM